

Calibration of an Ultrasound Tomography System
for Medical Imaging with 2D Contrast-Source
Inversion

by

Gabriel Paul Faucher

A Thesis submitted to the Faculty of Graduate Studies of

The University of Manitoba

in partial fulfilment of the requirements of the degree of

MASTER OF SCIENCE

Department of Electrical and Computer Engineering

University of Manitoba

Winnipeg

Copyright © 2013 by Gabriel Paul Faucher

Abstract

This dissertation describes two possible methods for the calibration of an ultrasound tomography system developed at University of Manitoba's Electromagnetic Imaging Laboratory for imaging with the contrast-source inversion algorithm. The calibration techniques are adapted from existing procedures employed for microwave tomography. A theoretical model of these calibration principles is developed in order to provide a rationale for the effectiveness of the proposed procedures. The applicability of such an imaging algorithm and calibration methods in the context of ultrasound are discussed.

Also presented are 2D and 3D finite-difference time-domain update equations for the simulation of acoustic wave propagation in inhomogeneous media. Details regarding the application of an absorbing boundary-condition, point-source modelling and the treatment of penetrable objects are included in this document.

Contributions

This dissertation reports on the development of two calibration techniques that can be used to prepare data collected by an ultrasound tomography (UST) system for imaging with the finite-element contrast-source inversion (FEM-CSI) algorithm (written by Dr. Amer Zakaria). More specifically, elements contributed by the author include:

- The adaptation of the theoretical FEM-CSI imaging problem to the context of acoustics.
- The identification of noise sources and measurement error present in the UST system developed at University of Manitoba's Electromagnetic Imaging Laboratory.
- The development and implementation of signal-processing techniques which can be used to improve and calibrate data collected by the UST system.
- The implementation of two and three dimensional finite-difference time-domain acoustical simulation software with support for scattering from penetrable objects.

Acknowledgments

First and foremost, I would like to thank my advisor, Dr. Joe LoVetri, for giving me the opportunity to broaden my knowledge and understanding. Your guidance, wisdom and support has been invaluable to me throughout my graduate work.

I would also like to thank my colleagues Dr. Amer Zakaria, Dr. Ian Jeffrey, Dr. Majid Ostadrahimi, Pedram Mojabi, Mohammad Asefi, Dr. Puyan Mojabi, Cameron Kaye and Dr. Colin Gilmore. Your insight and encouragement has been very much appreciated over the years. Special thanks to Chathura Kumaragamage and Paul Oramasionwu for your efforts in developing and maintaining the ultrasound system.

I would like to express my appreciation for the time taken by my examining committee members: Dr. Neil Popplewell and Dr. Sherif Sherif.

Finally, to my family and friends, thank you for your continued support and encouragement during my post-secondary career.

Table of Contents

List of Tables	vii
List of Figures	viii
Abbreviations and Symbols	xi
1 Introduction	1
1.1 Motivation and Problem Statement	2
1.2 Literature Review	3
2 The Ultrasound Tomography System	7
2.1 System Overview	7
2.2 The Ultrasound Tomography Chamber	8
2.2.1 Piezoelectric Transducers	11
2.3 Measurement Parameters	12
3 Physics of Acoustics	15
3.1 Introduction	15
3.2 Inhomogeneous Acoustic Wave Equation	16
3.3 Relation to Electromagnetics	23
4 Finite-Difference Time-Domain Model	25
4.1 Introduction	25
4.2 FDTD Update Equations	26
4.3 Scattering from Penetrable Objects	32
4.4 Source Modelling	35
4.4.1 3D Source Model	35
4.4.2 2D Source Model	36
4.5 Simulation Domain Truncation	36
5 Finite-Element Contrast-Source Inversion	39
5.1 Equation Governing the Acoustic Problem	39
5.2 Problem Formulation	42
5.3 Special Considerations for Acoustics	45

6	Calibration	51
6.1	System Model	51
6.2	Calibration Coefficients	54
6.3	Incident Field Calibration Principle	56
6.3.1	Calibrating FDTD Data	57
6.3.2	Calibrating UST-System Data	58
6.4	Scattered Field Calibration Principle	60
6.5	Modelling Acoustic Fields for Calibration	62
6.5.1	Incident Field Model	63
6.5.2	Calibration Object Model	65
6.6	Time-Domain Signal Processing	66
6.6.1	Time-of-Flight Determination	66
6.6.2	Transducer Localization	71
6.6.3	Signal Data Windowing	72
6.7	Known Calibration Issues	80
6.8	Summary of Calibration Steps	83
7	Results	86
7.1	Transducer Localization	86
7.2	Calibration Results	95
7.2.1	The Imaging Phantom	95
7.2.2	Incident Field Calibration	96
7.2.3	Scattered Field Calibration	103
7.2.4	Time-Domain Windowing	111
8	Conclusions and Future Work	113
8.1	Future Work	115
A	Additional Inversion Results	117
B	Frequency-Domain Representation of Signal Data	124
	References	130

List of Tables

7.1	Summary of transducer positioning error for 20 different random model configurations	92
-----	--	----

List of Figures

1.1	Ultrasound tomography principle	5
2.1	High-level diagram of the UST system	8
2.2	Pictures of the ultrasound tomography chamber	10
2.3	Ultrasound chamber dimensions	11
2.4	A piezoelectric transducer used in the UST chamber	12
4.1	3D-FDTD grid element	30
4.2	2D-FDTD grid element	31
4.3	Inhomogeneous 1D-FDTD domain at the interface of two media	33
4.4	Inhomogeneous 1D-FDTD domain with redefined boundary parameters	33
5.1	Geometrical model of the imaging problem	42
5.2	Inversion results of synthetic data for different object sizes	47
5.3	Inversion results of synthetic data for objects with different density discrepancies	49
6.1	A representative block-diagram of the UST system	52
6.2	A simplified block-diagram of the UST system	53
6.3	Comparison of raw and cleaned signal data	68
6.4	Illustration of time-domain data distortion	74
6.5	Example window plot	75
6.6	Geometrical model of the windowing domain	76
6.7	Example of ray paths used for window bound determination	77
6.8	Illustration of windowing applied to scattered field data	79
6.9	Illustration of incident and scattered ray arrival angles	81
7.1	Example of a constructed transducer-ring model	89
7.2	Illustration of rays used to determine pairwise transducer distance	90
7.3	Illustration of sample matrices before and after correction	91
7.4	Comparison of expected and computed transducer positions for an example model	93
7.5	Transducer locations computed from measurement data	94
7.6	Reconstructions of FDTD data after the application of the incident field calibration	98

7.7	Images of human-tissue phantom data	99
7.8	Reconstructions of phantom data calibrated with the incident field calibration when different numbers of receivers are used in the inversion	101
7.9	Reconstructions of calibrated FDTD data when different numbers of observation points are used in the inversion	102
7.10	Reconstructions of FDTD data after the application of the scattered field calibration	104
7.11	Reconstructions of phantom data after the application of the scattered field calibration	106
7.12	Reconstructions of phantom data calibrated with the scattered field calibration when different numbers of receivers are used in the inversion	108
7.13	Images of a noisy FDTD-simulated phantom with the scattered field calibration	110
7.14	Reconstructions of calibrated phantom data for different windowing domain sizes	112
A.1	Reconstructions of the calibration object after applying the incident field calibration	118
A.2	Reconstructions of human-tissue phantom data at 1.1 MHz	119
A.3	Reconstructions of human-tissue phantom data at 1.5 MHz	120
A.4	Inversion results of data for two aluminium wires at 1.2 MHz	121
A.5	Inversion results of data for three aluminium wires at 1.4 MHz	122
A.6	Inversion results of data for a high-density polyethylene rod at 1.2 MHz	123
B.1	Measured time-domain incident field signal before applying the FFT .	126
B.2	Frequency-domain representation of a measured incident field signal .	127
B.3	Measured time-domain scattered field signal before applying the FFT	128
B.4	Frequency-domain representation of a measured scattered field signal	129

List of Algorithms

6.1	Signal-Arrival Sample Determination	67
6.2	Cleaning Noisy Signal Data	68
6.3	Time-of-Flight Matrix Correction	70
6.4	MDS Localization	72
6.5	Incident Field Calibration	84
6.6	Scattered Field Calibration	85

Abbreviations and Symbols

Abbreviation	Description
1D	One Dimensional
2D	Two Dimensional
3D	Three Dimensional
ABC	Absorbing Boundary Condition
CFL	Courant-Friedrichs-Lewy
CURE	Computed Ultrasound Risk Evaluation
CSI	Contrast-Source Inversion
DC	Direct Current
FDTD	Finite-Difference Time-Domain
FEM	Finite Element Method
FEM-CSI	Finite-Element Contrast-Source Inversion Method
FFT	Fast Fourier Transform
GUI	Graphical User Interface
IFFT	Inverse Fast Fourier Transform
LTI	Linear Time-Invariant
MDS	Multidimensional Scaling
MHz	Mega Hertz
MWT	Microwave Tomography
OI	Object of Interest
PC	Personal Computer
PEC	Perfect Electric Conductor
PVC	Polyvinyl Chloride
RTT	Reynolds Transport Theorem

SG/DA	Signal Generation and Data Acquisition
SVD	Singular Value Decomposition
TM	Transverse Magnetic
TOF	Time of Flight
TR	Transmitter-Receiver
UMEIL	University of Manitoba Electromagnetic Imaging Laboratory
UST	Ultrasound Tomography

Symbol	Description
\vec{a}	Denotes a as a vector quantity
\triangleq	Denotes a definition
\Rightarrow	Denotes analogous terms
∇	Gradient operator
$\nabla \cdot$	Divergence operator
C	Calibration coefficient
c	Speed of sound
c_b	Speed of sound in the background medium
\mathcal{D}	FEM-CSI imaging domain
d	Distance variable
f	Frequency
f_s	Sampling frequency
G	System function of UST chamber input devices
H	System function of UST chamber
\mathbb{H}	System function of UST chamber with calibration object
i, j, k	FDTD-grid spatial indices
K	System function of UST chamber output devices
k	Wavenumber
k_b	Wavenumber of background medium
L	System function of UST chamber multipath
n	FDTD temporal index

P	Fluid pressure
P_0	Average fluid pressure
p	Incremental fluid pressure
$p^{inc}, p^{tot}, p^{scat}$	Incident, total and scattered pressure fields
$p_f(\cdot)$	Incident pressure field function
\vec{r}, \vec{r}'	Position vectors in Cartesian coordinates
\vec{r}_0	Position of the point source in Cartesian coordinates
\mathcal{S}	FEM-CSI measurement surface
s	Time-domain signal
\mathring{s}	Windowed time-domain signal
T	Time-of-flight matrix
T	Water temperature
t	Time variable
\vec{U}	Fluid velocity vector
\vec{U}_0	Average fluid velocity vector
\vec{u}	Incremental fluid velocity vector
$\vec{u}^{inc}, \vec{u}^{tot}, \vec{u}^{scat}$	Incident, total and scattered velocity fields
\mathcal{W}	Windowing domain
X	Frequency domain representation of UST system input signal
Y	Frequency domain representation of UST system output signal
\mathbb{Y}	Frequency-domain UST system output signal for calibration object
Γ	FEM-CSI problem domain boundary
$\delta(\cdot)$	Dirac delta function
Δh	FDTD-grid element step size
κ	Average fluid bulk modulus
κ_b	Average bulk modulus of the background medium
Λ	Set of transducer location estimates
ϱ	Fluid density
ρ	Average fluid density
ρ_1	Incremental fluid density

ρ_b	Average density of the background medium
τ, τ_a, τ_b	Transmitter indices
φ_τ	Contrast-source variable for an active transmitter τ
χ	Contrast variable
χ'	Normalized contrast variable ($\chi + 1$)
Ω	FEM-CSI problem domain
ω	Angular frequency ($2\pi f$)

Introduction

Medical imaging has become an indispensable tool for diagnosing various ailments of the human body. A large factor driving its popularity is that it can provide information about a patient without the need for biopsy. Modern imaging modalities capable of producing multidimensional images include: X-ray Computed Tomography (X-ray CT), Magnetic Resonance Imaging (MRI), Positron Emission Tomography (PET) and Ultrasound [1]. These methods utilise high-speed electronics and computers for data collection and image reconstruction. They differ from simpler planar imaging modalities, such as the common X-ray, which usually produce images on a film from exposure to an external radiation source during imaging. These planar imaging methods provide images that are two-dimensional projections, or shadows, of an anatomical region of interest.

The device under consideration in this work is the ultrasound tomography (UST) system developed at the University of Manitoba Electromagnetic Imaging Laboratory (UMEIL). The principle of UST is to insonify a target at many angles about a single axis of rotation and to create an image from the scattered signals produced by acoustic interactions with the object. This approach differs from conventional ultrasound imaging, such as obstetric ultrasonography, which only uses signal echoes to produce images [2]. Furthermore, images produced by conventional ultrasound only provide

spatial information about a target. Image reconstruction techniques employed at the UMEIL provide not only spatial information but are also used to determine physical properties of a target to produce what can be thought of as a “property map”.

1.1 Motivation and Problem Statement

Breast cancer is the most common cancer among women worldwide. This disease alone is responsible for over 450,000 deaths each year [3] and thus requires an effective method of detection. Currently, the most effective detection technique is X-ray mammography, though it has the disadvantage of using potentially harmful ionising radiation [4]. In light of this, members of the Electromagnetic Imaging Laboratory at the University of Manitoba have developed a microwave tomography (MWT) system suitable for biological imaging [5–8]. Both Finite-Element Contrast-Source Inversion (FEM-CSI) [9] and Gauss-Newton Inversion [10] imaging techniques have been successfully applied to reconstruct phantoms and biological targets.

Building on these accomplishments, the question of whether these principles can be extended to ultrasound tomography is being explored at the UMEIL. The group has already built a UST system capable of acquiring scattered ultrasound signals from an insonified target [11]. A 2D image reconstruction software based on FEM-CSI has also been developed for an idealised acoustical model. What is now required is a calibration process which takes raw data from the UST system and adjusts it to better conform to the idealised model expected by the imaging algorithm. The purpose of this work is to bridge the gap between measured data and FEM-CSI by developing such a calibration process.

The calibration process involves a two step procedure. The first step is to characterize and adjust the UST system hardware to optimize the quality of acquired data.

The second step is to prepare the data for the inversion algorithm through the use of software signal processing techniques. The challenges addressed in this work are therefore summarized as follows:

1. Identify and mitigate sources of noise and other signal corrupting effects present in the UST system during normal operation.
2. Determine optimal user-definable measurement parameters to obtain the best quality data.
3. Develop signal processing software capable of removing the effects of the measurement system from signal data and prepare it for the reconstruction algorithm.
4. Determine other information required by the inversion algorithm, such as the relative spatial coordinates of the ultrasound sources.

1.2 Literature Review

The beginnings of ultrasound imaging can be traced back to the invention of the supersonic reflectoscope by F. Firestone in 1940 [12]. Originally, the device was conceived to detect defects in metals by applying principles of acoustic pulse-echo range finding. Almost a decade later, hospitals in Japan, the United States and Sweden applied commercialized versions of the reflectoscope to the human body for medical diagnostic purposes. Since then, clinical ultrasound systems have evolved into portable devices capable of nearly real-time 3D imaging.

Commonly known clinical ultrasound devices involve the use of a transducer wand with an imaging system operated by qualified personnel. In many ways, this type of

apparatus differs from ultrasound tomography systems in development today. Principles of UST require that a target be encircled by at least one ring of transducers. In contrast to the pulse-echo mechanism of a transducer wand, the ring transducers insonify the target at different angles while the remaining transducers receive the resulting scattered acoustic fields (see Figure 1.1). Several such UST systems are being developed in North America. The Computed Ultrasound Risk Evaluation (CURE) prototype [13, 14] developed at the Karmanos Cancer Institute in Detroit Michigan, uses one transducer ring that can be translated along its longitudinal axis. Such an apparatus allows for the reconstruction of 2D images of many slices of the target. It is specifically designed for the detection of breast cancer. Other systems developed for medical applications exist at the University of Rochester in New York [15] and at the University of California in San Diego [16]. They both make use of a single fixed ring-transducer; the former implements 2048 elements whereas the latter, up to 1024.

Many calibration techniques have been created for conventional ultrasound systems as outlined in [17]. Unfortunately, there is little literature providing details on the calibration of UST systems. Of the four referenced papers on the three aforementioned UST systems, only [15] provides details regarding system calibration. The calibration method described uses a pulse-echo technique to determine the distance of each transducer from a metal wire placed at the center of the ring. This method relies on the ability of each individual transducer to transmit as well as receive a signal during the same acquisition period. Unfortunately, the UST system at the UMEIL is not designed to receive echoes on the transmitting transducer; when a particular transducer is set as transmitter, signals may only be received by the other transducers. Due, in part, to this limitation, known calibration techniques employed at the UMEIL for MWT [18] have been adapted for ultrasound tomography. Details

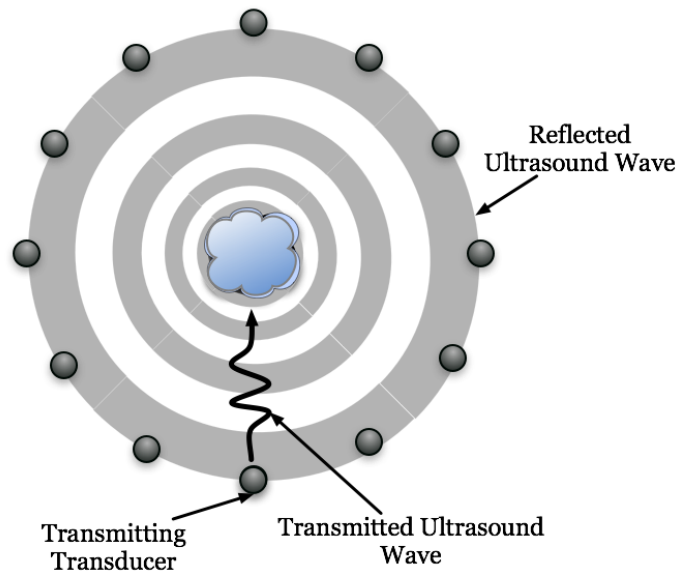


Figure 1.1: Ultrasound tomography principle. A target is insonified at different angles by successively transmitting an ultrasound signal from each transducer while the others receive the scattered wave.

regarding these techniques are described in Chapter 6.

The FEM-CSI imaging algorithm requires, among other things, knowledge of the spatial coordinates of the transducer locations. Due to the operating wavelength of ultrasound and the structure of the transducers, it is not possible to accurately determine relative transducer locations with a “measuring stick”. It is for this reason that an acoustical source localization technique is employed. Such techniques are often based on Multidimensional Scaling (MDS) [19] algorithms with variations on error correction and on the estimation of missing information [20–23]. The method most applicable to this work is a simplification of a procedure suggested in [20]. The simplified procedure requires only signal time-of-flight (TOF) information between pairs of system transducers which can almost entirely be determined using threshold detection techniques. When the TOF between pairs cannot be found due to their

close proximity, the procedure allows for the estimation of missing TOF data. Error correction is also a part of this localization technique and improves the computed coordinates.

2

The Ultrasound Tomography System

This chapter provides a description of the ultrasound tomography (UST) system developed at the University of Manitoba Electromagnetic Imaging Laboratory. Design and construction of the system was conceived as an undergraduate project in 2010 with applications to breast cancer imaging and detection. Only a brief overview of the system is provided in the following sections. The reader is referred to [11] for a detailed system description.

2.1 System Overview

The UST system is composed of many interconnected hardware components that are managed with customized system-control software. A high-level block diagram of the system is shown in Figure 2.1. As can be seen, all control software resides on a desktop computer (PC) fitted with signal generation (SG) and data acquisition (DA) boards. Devices external to the PC are the UST chamber and the transmitter-receiver (TR) module. The SG/DA boards were purchased from the DynamicSignals company. The TR-module was purchased from Sonometrics Corporation.

The software component of the UST system is implemented entirely in MATLAB [24]. This software includes a graphical user interface (GUI) which makes it possible to configure many aspects of the UST system. With this same interface, the user is able

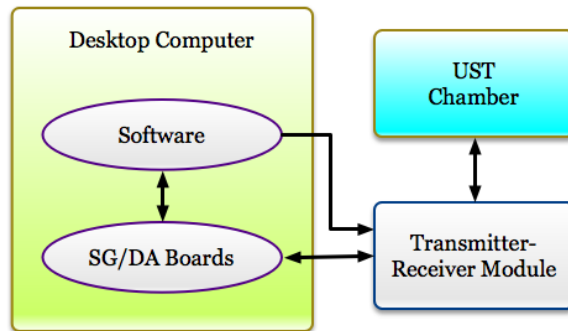


Figure 2.1: High-level diagram of the UST system. The arrows denote communication channels between the system components.

to make data acquisition requests which initiate the insonification of the target object held within the UST chamber. A data acquisition consists of successively transmitting a signal on each transducer, while the others receive the signal scattered by the chamber contents. A sampled time-domain signal is acquired for each transmitter-receiver pair.

The TR-module is responsible for directing signal data between the PC and the UST chamber. When insonification of the target is initiated, the control software first configures the TR-module and initializes the SG/DA boards. The TR-module then drives the transducers of the UST chamber with voltage signals generated by the SG boards and routes the acquired signals to the DA cards for digital encoding. The encoded time-domain data is then stored on the PC. It is this data that is calibrated for imaging using methods described in Chapter 6.

2.2 The Ultrasound Tomography Chamber

Aspects of the UST chamber relevant to calibration of the acquired data is discussed in this section. A good characterization of the effects that the chamber components have on the received signals is important for the development of an effective

calibration procedure. Devices exterior to the chamber are not covered in great detail as their combined effects on measured data can be represented by a single system function (see Chapter 6).

The UST chamber, pictured in Figure 2.2(a), is a polyvinyl chloride (PVC) tube submerged in a larger water-filled container. It has an inner-diameter of approximately 15.2 cm and a height of 27 cm as depicted in Figure 2.3. Originally, the chamber contained only a single ring of 32 evenly-spaced transducers as described in [11]. Currently, 8 levels of 32 evenly-spaced transducers are affixed to the inner wall, providing support for 256 piezoelectric crystals. All transducers are mounted in such a way that their main signal beams point in a direction inwardly normal to the mounting wall. Water-proof cables connected to the transducer backing are led directly out, through the chamber wall to the TR-module.

The transducer mounts offer 1 cm separation between the transducer crystals and the chamber wall. It is in this space and on the chamber floor that an acoustically absorptive foam is placed to reduce signal reflections from the inner walls (see Figure 2.2(b)). The material used is basic foam carpet underlay. An effort is made to mitigate reflections within the chamber in order to simplify the calibration procedure (see section 6.5.1). The water level is kept at least 3 cm above the top of the chamber for a similar reason. The air-water interface created above the UST chamber creates an almost perfectly reflective boundary for acoustic signals. By maintaining the water level sufficiently high above the inner cylinder, reflected signals from this interface will only arrive at receiving transducers after sampling has completed.



(a)



(b)

Figure 2.2: Pictures of the ultrasound tomography chamber. (a) PVC ultrasound chamber in surrounding container. Under normal operation the chamber is entirely submerged. (b) Ultrasound chamber with acoustically absorptive foam along inner wall and floor.

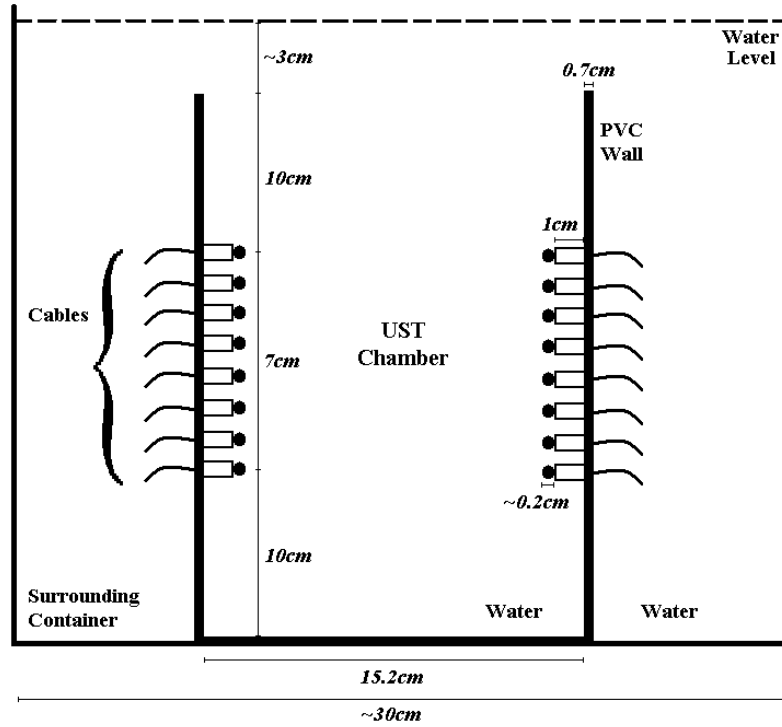


Figure 2.3: Ultrasound chamber dimensions.

2.2.1 Piezoelectric Transducers

The ultrasound transducers of the UST system were supplied by Sonometrics Corporation. They are driven at frequencies in the range of 1.1 MHz to 1.5 MHz and it has been observed that they have a resonant frequency near 1.3 MHz [11]. These cylindrical crystals are made of lead zirconate titanate (PZT-5H), a material exhibiting the piezoelectric effect [25]. Individual crystals were dipped in an epoxy compound by the supplier to provide better coupling to the background medium (water). The resulting ultrasound transducers are roughly spherical with a diameter of approximately 2 mm as shown in Figure 2.4. Every transducer of the UST chamber has the ability to both transmit and receive ultrasound signals.

Insonification of the target object is made possible by generating ultrasonic pressure waves with a transducer in transmit-mode. When the transducer is driven with

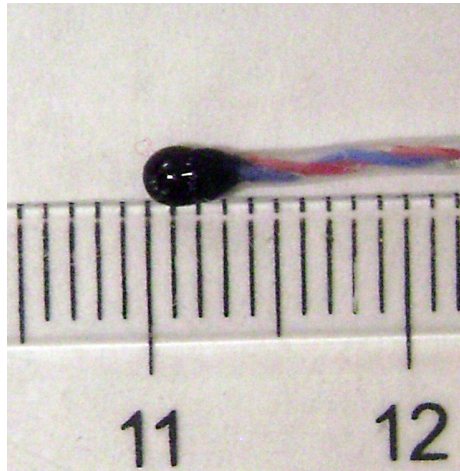


Figure 2.4: A piezoelectric transducer used in the UST chamber.

a voltage signal, its structure deforms and creates local pressure changes in the propagating medium (water). These pressure changes then travel through the medium as ultrasound waves and interact with the target.

Ultrasound signals can be measured when pressure waves reach transducers in receive-mode. The pressure waves cause the crystals to deform and thereby generate voltage signals that can be recorded electronically. In this manner, data acquired by the UST system is effectively a measure of pressure fields at receiving transducers.

2.3 Measurement Parameters

The measurement software GUI holds many configuration options to control various aspects of the UST system. The following is a description of the most commonly used system parameters and their settings for data acquisition.

Transducer Selection The transducers used to insonify the UST chamber contents and those used to receive the scattered signals are set with this parameter. Since this work is concerned with calibration for 2D imaging, only one level of

transducers is selected at a time.

Waveform This parameter allows the user to set the type of signal that is radiated by the transmitting transducer. Two options are available: a short pulse or a sinusoid. The sinusoid option is used for imaging purposes because the generated wave can be set to a frequency of interest. Frequencies commonly used are in the range of 1.1 MHz to 1.5 MHz.

Pattern Length This parameter is only available when the waveform is set to “sinusoid”. As such, the pattern length refers to the duration of the sinusoidal signal. It has been observed that a signal long enough to mimic the effects of a continuous wave provides the most meaningful results. For this reason the pattern length is set to at least 10 microseconds, time enough to generate at least 10 periods of a sinusoid at 1 MHz.

Sampling Rate The sampling rate refers to the number of samples the DA boards are to take of the received signal per second. The possible settings are 10 MHz, 50 MHz and 100 MHz. For acceptable accuracy, the received signal should be sampled at a rate of ten data points per wavelength or more. For this reason, 10 MHz is barely sufficient for a frequency of interest of 1MHz. Therefore, a sampling rate of 50 MHz is commonly used.

Number of Samples This parameter sets the number of samples that are to be acquired by the receiving transducers at every signal transmission. This option is set such that a sufficient number of samples is taken for the scattered signals to be received at the chosen sampling rate. Based on the UST chamber dimensions and the expected speed of sound in water, this parameter is often set to 7000 samples.

Averaging Signal averaging is used to reduce random noise in the measured signals.

This is based on the principle that with sufficient samples, random noise will average to zero and leave only the more definite signal of interest. Experience suggests that an average of 80 signals produces data clean enough for signal processing.

3

Physics of Acoustics

Many of the techniques used to characterize electromagnetic (EM) wave behaviour may be used to understand waves in analogous systems. Acoustic wave behaviour is a good example of this parallelism as it shares many analogous concepts with electromagnetic theory [26,27]. In this chapter, some aspects of acoustical theory are developed and its similarities to EM wave behaviour are shown.

3.1 Introduction

Acoustics can be described as the theory of pressure disturbances propagating in a medium. The medium may be a solid material or a fluid such as air or water. This chapter establishes a characterization of fields at a macroscopic level, where the medium is regarded as a continuous distribution. This differs from the microscopic perspective in which the motion of individual molecules is considered (Brownian motion [28]). As such, it is convenient to visualize a medium as a conglomeration of particles and an individual particle be regarded as a tiny bit of matter, rather than as a molecule. This is akin to the macroscopic behaviour of matter required for Maxwell's equations [29,30].

Even though acoustical systems behave in ways similar to EM systems, there are several differences that must be noted. One principal difference arises when

considering the physics of the media in the problem being solved. The speed of an EM wave depends on the permittivity and permeability of the medium whereas sound speed is dependent on its density and bulk modulus [26]. Later in this chapter, these material properties are shown to be analogous in their relation to the wave equation.

Another difference is that EM fields are typically perceived as transverse waves whereas acoustical systems are dominated by longitudinal waves in gases and most liquids. The fluid particles move in the direction of wave propagation through a series of compressions and rarefactions. The restoring force responsible for propagating the wave is simply opposition of the fluid to being compressed [31]. Shear (transverse) waves do arise in solids and some liquids but are relatively weak compared to longitudinal waves. This is particularly the case for water as it does not support transverse waves due to its negligible shear strength [32–34]. This insight is important because the propagation medium utilized in this work is water. For these reasons, transverse wave propagation is not considered here. Both solid and fluid media are assumed to only support longitudinal waves for the model developed in this chapter.

It should be noted that only linear small-amplitude wave propagation is considered in the derivations of the following section. Any non-linear effects arising from wave-mixing or shock wave formation are assumed to be negligible or non-existent.

3.2 Inhomogeneous Acoustic Wave Equation

Within a medium, local pressure gradients cause local accelerations of the constituent particles which result in local velocity changes. In turn, these lead to local density variations which then bring upon new pressure gradients. These interactions within a medium result in acoustic waves that can be described by a linear model of

fluid flow [26]. Acoustic waves are thus characterized by the following fields

$$\begin{aligned} P(\vec{r}, t) &: \text{fluid pressure (N/m}^2\text{)} \\ \vec{U}(\vec{r}, t) &: \text{fluid velocity (m/s)} \\ \varrho(\vec{r}, t) &: \text{fluid mass density (kg/m}^3\text{)}. \end{aligned}$$

Derivation of the inhomogeneous acoustic wave equation depends on the conservation of the fluid's mass and linear momentum. Once the conservation relations are established, an equation of state for the particular fluid is used to link the two resulting expressions.

We begin by deriving a mass conservation relation. Conservation of mass states that the mass within an isolated volume remains constant as it moves or deforms over time. This can be written mathematically as

$$\frac{d}{dt} \int_{V(t)} \varrho(\vec{r}, t) dv = 0 \quad (3.1)$$

where $\vec{r} = (x, y, z)$ is the position vector, t is the time parameter and $V(t)$ is any volume in the medium that may deform and move with velocity $\vec{U}(\vec{r}, t)$ [26]. In this context, the Reynolds transport theorem (RTT) [35] may be applied to equation (3.1) to relate density and fluid velocity:

$$\int_{V(t)} \frac{\partial \varrho(\vec{r}, t)}{\partial t} + \nabla \cdot (\varrho(\vec{r}, t) \vec{U}(\vec{r}, t)) dv = 0 \quad (3.2)$$

where the surface integral arising from the application of RTT is cast into a volumetric integral by the divergence theorem [26, 36]. Since $V(t)$ is an arbitrary volume it follows that the integrand of (3.2) is identically zero. A governing mass conservation equation

for the acoustic medium is therefore obtained:

$$\frac{\partial \varrho(\vec{r}, t)}{\partial t} + \nabla \cdot \left(\varrho(\vec{r}, t) \vec{U}(\vec{r}, t) \right) = 0. \quad (3.3)$$

We now derive a relation for the conservation of linear momentum in the medium. The continuum generalization of Newton's second law [37] may be written as

$$\frac{d}{dt} \int_{V(t)} \varrho(\vec{r}, t) \vec{U}(\vec{r}, t) dv = \int_{V(t)} \vec{F}(\vec{r}, t) dv \quad (3.4)$$

where $\vec{F}(\vec{r}, t)$ is the total force density acting on the volume of fluid [26, 36]. For the purposes of this work, forces are assumed to arise only from pressure gradients in the fluid; viscosity and external forces such as gravity are ignored. To express total force density, \vec{F} , as a fluid pressure gradient, ∇P , consider a small rectangular volume of fluid with dimensions Δx , Δy , Δz that is subject to a net force, \vec{f} . Since the total force density is just the total force per unit volume, we have the following relation for the first vector component of \vec{F} :

$$F_x = \lim_{\Delta x, \Delta y, \Delta z \rightarrow 0} \frac{f_x}{\Delta x \Delta y \Delta z} \quad (3.5)$$

where f_x is the net force on the volume in the x -direction. Since pressure is defined as the force normal to an area, f_x in (3.5) can be understood as the pressure difference

across the Δx dimension of the volume:

$$\begin{aligned}
 F_x &= \lim_{\Delta x, \Delta y, \Delta z \rightarrow 0} \frac{P(x, y, z)\Delta y\Delta z - P(x + \Delta x, y, z)\Delta y\Delta z}{\Delta x\Delta y\Delta z} \\
 F_x &= \lim_{\Delta x \rightarrow 0} \frac{P(x, y, z) - P(x + \Delta x, y, z)}{\Delta x} \\
 F_x &= -\frac{\partial P}{\partial x}.
 \end{aligned} \tag{3.6}$$

The derivative in (3.6) is negative because the force vector points in the direction of decreasing pressure. A similar procedure can be applied to the remaining component directions to obtain

$$\vec{F} = -\nabla P \tag{3.7}$$

in three dimensions.

Combining equations (3.4) and (3.7), the integral form of Newton's second law may now be written as

$$\frac{d}{dt} \int_{V(t)} \rho(\vec{r}, t) \vec{U}(\vec{r}, t) dv = - \int_{V(t)} \nabla P(\vec{r}, t) dv. \tag{3.8}$$

Applying RTT and then the divergence theorem to obtain an expression in terms of volumetric integrals, equation (3.8) becomes

$$\int_{V(t)} \frac{\partial \rho(\vec{r}, t) \vec{U}(\vec{r}, t)}{\partial t} + \nabla \cdot \left(\rho(\vec{r}, t) \vec{U}(\vec{r}, t) \vec{U}(\vec{r}, t) \right) dv = - \int_{V(t)} \nabla P(\vec{r}, t) dv. \tag{3.9}$$

Note that the term $\rho(\vec{r}, t) \vec{U}(\vec{r}, t) \vec{U}(\vec{r}, t)$ evaluates to a second-rank tensor. Since $V(t)$ is arbitrary, integrands in (3.9) may be equated to give the differential form of the

linear momentum conservation equation

$$\frac{\partial \varrho(\vec{r}, t) \vec{U}(\vec{r}, t)}{\partial t} + \nabla \cdot \left(\varrho(\vec{r}, t) \vec{U}(\vec{r}, t) \vec{U}(\vec{r}, t) \right) = -\nabla P(\vec{r}, t). \quad (3.10)$$

The two conservation equations (3.3) and (3.10) form the basis from which the inhomogeneous acoustic wave equation is derived.

In order to obtain a small-amplitude model for acoustical wave propagation from equations (3.3) and (3.10), the three field quantities P , \vec{U} and ϱ are represented as an average field, plus a small fluctuation:

$$\begin{aligned} P(\vec{r}, t) &= P_0 + p(\vec{r}, t) \\ \vec{U}(\vec{r}, t) &= \vec{U}_0 + \vec{u}(\vec{r}, t) \\ \varrho(\vec{r}, t) &= \rho(\vec{r}) + \rho_1(\vec{r}, t) \end{aligned} \quad (3.11)$$

where the fluctuations in pressure, velocity and density are small: $|p| \ll |P_0|$ and $|\rho_1| \ll |\rho|$. Note that P_0 is a constant and that $\vec{U}_0 = 0$ because the fluid is assumed to be at rest. It is also worth noting that defining the average density as a function of \vec{r} allows for the modelling of inhomogeneous media.

If (3.11) is substituted into (3.3), the conservation of mass equation becomes

$$\frac{\partial \rho_1(\vec{r}, t)}{\partial t} + \nabla \cdot (\rho(\vec{r}) \vec{u}(\vec{r}, t)) = 0 \quad (3.12)$$

where the second-order term $\nabla \cdot (\rho_1(\vec{r}, t) \vec{u}(\vec{r}, t))$ has been removed because it is a negligible product of two small first-order terms. Similarly, if (3.11) is substituted

into (3.10), the conservation of linear momentum equation becomes

$$\rho(\vec{r}) \frac{\partial \vec{u}(\vec{r}, t)}{\partial t} + \nabla p(\vec{r}, t) = 0 \quad (3.13)$$

where the third-order term $\nabla \cdot (\rho_1(\vec{r}, t) \vec{u}(\vec{r}, t) \vec{u}(\vec{r}, t))$ and both second-order terms, $\partial(\rho_1(\vec{r}, t) \vec{u}(\vec{r}, t)) / \partial t$ and $\nabla \cdot (\rho(\vec{r}) \vec{u}(\vec{r}, t) \vec{u}(\vec{r}, t))$, are all negligible and removed.

The conservation equations, (3.12) and (3.13), appear as a system of two equations in the following three variables: $p(\vec{r}, t)$, $\vec{u}(\vec{r}, t)$ and $\rho_1(\vec{r}, t)$. As such, there is a need for a third equation linking at least two of these variables. If it is assumed that adjacent volumes of fluid in the system do not exchange significant heat then the entropy of the fluid remains constant with time. Such processes are known as isentropic and lead to an equation of state involving the three variables and the bulk modulus (incompressibility) of the medium in question [26, 38–40]. This equation may be written in the form given in [39]:

$$\frac{DP(\vec{r}, t)}{Dt} = \frac{\kappa(\vec{r})}{\rho(\vec{r})} \frac{D\rho(\vec{r}, t)}{Dt}, \quad (3.14)$$

where the known quantity $\kappa(\vec{r})$ is the average adiabatic bulk modulus of the fluid in units of pressure (N/m^2) and the differential operator, D/Dt , is defined as

$$\frac{D}{Dt} \triangleq \frac{\partial}{\partial t} + \vec{U}(\vec{r}, t) \cdot \nabla \quad (3.15)$$

where “ \cdot ” denotes the dot-product. The equation of state can be written in terms of small-amplitude field quantities by substituting (3.11) into (3.14) and making obvious

simplifications. It can then be reduced to

$$\frac{\partial p(\vec{r}, t)}{\partial t} = \frac{\kappa(\vec{r})}{\rho(\vec{r})} \left(\frac{\partial \rho_1(\vec{r}, t)}{\partial t} + \vec{u}(\vec{r}, t) \cdot \nabla \rho(\vec{r}) + \vec{u}(\vec{r}, t) \cdot \nabla \rho_1(\vec{r}, t) \right) \quad (3.16)$$

by removing the term $\vec{u}(\vec{r}, t) \cdot \nabla p(\vec{r}, t)$ based on the assumption that the pressure-wave speed is much greater than local particle velocities and thus $\partial p / \partial t \gg \vec{u} \cdot \nabla p$ [40]. The two conservation equations together with (3.16) now form a system of three equations in three variables.

The system of equations can be simplified by first substituting (3.12) into (3.16) to obtain

$$\frac{\partial p(\vec{r}, t)}{\partial t} = \frac{\kappa(\vec{r})}{\rho(\vec{r})} (\nabla \cdot (\rho_1(\vec{r}, t) \vec{u}(\vec{r}, t)) - \varrho(\vec{r}, t) \nabla \cdot \vec{u}(\vec{r}, t)). \quad (3.17)$$

The variable $\rho_1(\vec{r}, t)$ can then be eliminated from (3.17) by noting that $\nabla \cdot (\rho_1(\vec{r}, t) \vec{u}(\vec{r}, t))$ is a negligible second order term and that $\varrho \approx \rho$. By applying these approximations to (3.17) and writing the resulting equation with (3.13), we arrive at a pair of coupled equations in $p(\vec{r}, t)$ and $\vec{u}(\vec{r}, t)$:

$$\nabla \cdot \vec{u}(\vec{r}, t) = -\frac{1}{\kappa(\vec{r})} \frac{\partial p(\vec{r}, t)}{\partial t} \quad (3.18)$$

$$\nabla p(\vec{r}, t) = -\rho(\vec{r}) \frac{\partial \vec{u}(\vec{r}, t)}{\partial t}. \quad (3.19)$$

It is interesting to note from (3.19) that $\partial \vec{u} / \partial t$ points in the direction of the pressure gradient $-\nabla p$ (higher pressure toward lower pressure). This implies that the derived acoustic equations indeed model the propagation of longitudinal waves.

The inhomogeneous acoustic wave equation for incremental fluid pressure, $p(\vec{r}, t)$, can now be obtained by taking the time derivative of (3.18), the divergence of (3.19)

and performing appropriate substitutions:

$$\nabla^2 p(\vec{r}, t) - \frac{\rho(\vec{r})}{\kappa(\vec{r})} \frac{\partial^2 p(\vec{r}, t)}{\partial t^2} = \frac{\nabla \rho(\vec{r})}{\rho(\vec{r})} \cdot \nabla p(\vec{r}, t) \quad (3.20)$$

where ∇^2 is the Laplace operator. The terms on the left-hand side of (3.20) consist of the wave equation for a homogeneous medium whereas the right-hand side is often referred to as the source term [39, 40].

3.3 Relation to Electromagnetics

Most of this work involves the transitioning of principles used for EM to the field of acoustics. In order to make this transition more intuitive, analogies between the two disciplines are made.

The first analogy is made for the physical properties of media. We begin by observing the homogeneous form of (3.20), which is obtained by setting its right-hand side to zero. The speed of acoustic wave propagation, c , is implicitly defined in this new equation as $c = \sqrt{\kappa/\rho}$ [38]. Next, we note that the homogeneous wave equation for the scalar electric field is identical to the homogeneous form of (3.20) except that the wave speed is related to the permittivity, ϵ , and permeability, μ , of the medium by $c_{EM} = \sqrt{1/\epsilon\mu}$ [26]. If the homogeneous wave equations for incremental pressure and scalar electric field were written in terms of c and c_{EM} , respectively, then it is conceivable that both equations would have analogous solutions when $\rho/\kappa = \epsilon\mu$. This forms the basis for the relation between EM and acoustic material parameters. Throughout this work, permittivity is selected as the analogue of compressibility, and

permeability that of density:

$$\epsilon \rightleftharpoons 1/\kappa \quad (3.21)$$

$$\mu \rightleftharpoons \rho. \quad (3.22)$$

A second analogy is made for the field quantities. The acoustic model is described in terms of two coupled variables known as the incremental pressure and the incremental velocity. Similarly, the EM model is represented by coupled electric and magnetic fields [41]. Since only pressure fields are considered in UST and it is the electric field which is of interest in MWT, it is most convenient to relate these two quantities. Hence, the field analogies are selected as

$$\text{Electric Field} \rightleftharpoons \text{Incremental Pressure} \quad (3.23)$$

$$\text{Magnetic Field} \rightleftharpoons \text{Incremental Velocity}. \quad (3.24)$$

4

Finite-Difference Time-Domain Model

Finite-Difference Time-Domain (FDTD) is a standard numerical modelling method that belongs to a class of grid-based time-domain techniques [42, 43]. It is often used to model electrodynamical systems based on the differential form of Maxwell's equations. In this chapter, it is shown how FDTD can be used to model acoustical systems.

4.1 Introduction

For this work, acoustic 2D and 3D time-domain simulation tools were developed based on FDTD principles. The purpose of these tools is not to simulate the entire UST system described in Chapter 2, but rather to investigate ultrasound signal propagation in the UST chamber only. These tools provided valuable insight when characterizing sources of measurement error due to the chamber. Simulation results were also used to validate calibration techniques in a controlled setting.

A good model of the UST chamber must satisfy certain criteria. One of these requirements is that the model must handle ultrasound wave propagation from a point-source excitation. It must also be flexible enough to allow for different background media because acoustical properties of water change with temperature. The model must also adequately simulate acoustic scattering from objects with user-definable density and bulk modulus.

An acoustic 3D-FDTD program was originally developed to model the seat-dip effect in concert halls [44]. This program was capable of simulating acoustic scattering from ideally hard and ideally soft objects in air only. As part of this work, the program was extended to simulate scattering from objects of variable density and bulk modulus. The background medium was also made user-definable to allow for the simulation of sound propagation through water at different temperatures. As for the 2D-FDTD program, it was written based on existing transverse magnetic (TM) 2D-FDTD source code. The TM program was a good starting point because the acoustic 2D-FDTD update equations are strikingly similar to those for the electromagnetic 2D-TM case presented in [45]. These EM equations were adapted for acoustics using the analogies presented in section 3.3. The 2D program was extended to allow modelling of point-sources and scattering from objects of varying acoustical properties.

The FDTD update equations derived in this chapter are based on the acoustic conservation equations established in Chapter 3. This implies that the FDTD model developed here only supports linear longitudinal wave propagation in fluids and solids. Transverse waves and non-linear effects are not supported by this model.

4.2 FDTD Update Equations

In order to simulate the UST chamber, we make use of the notions of incident, total and scattered field quantities. The incident field is a field value measured at an observation point when no scattering object is present in the simulation domain; the total field is a field value measured at an observation point when a scattering object is present; and the scattered field is the difference of the two. The field values are measured in response to a point-source insonifying the simulation domain. The acoustic wave pressure and velocity (introduced in Chapter 3) may then be expressed

in terms of these quantities as

$$\begin{aligned} p^{tot} &= p^{inc} + p^{scat} \\ \vec{u}^{tot} &= \vec{u}^{inc} + \vec{u}^{scat} \end{aligned} \quad (4.1)$$

where the superscripts *tot*, *inc* and *scat* denote the total, incident and scattered fields, respectively.

The acoustic conservation equations, (3.19) and (3.18), may be written in terms of the field quantities presented in (4.1). The incident fields satisfy

$$\nabla p^{inc}(\vec{r}, t) = -\rho_b \frac{\partial \vec{u}^{inc}(\vec{r}, t)}{\partial t} \quad (4.2)$$

$$\nabla \cdot \vec{u}^{inc}(\vec{r}, t) = -\frac{1}{\kappa_b} \frac{\partial p^{inc}(\vec{r}, t)}{\partial t} \quad (4.3)$$

where $\vec{r} = (x, y, z)$ is the location vector and t is the time variable. The values ρ_b and κ_b are the known density and the bulk modulus of the homogeneous background medium. Similarly, the total fields satisfy

$$\nabla p^{tot}(\vec{r}, t) = -\rho(\vec{r}) \frac{\partial \vec{u}^{tot}(\vec{r}, t)}{\partial t} \quad (4.4)$$

$$\nabla \cdot \vec{u}^{tot}(\vec{r}, t) = -\frac{1}{\kappa(\vec{r})} \frac{\partial p^{tot}(\vec{r}, t)}{\partial t} \quad (4.5)$$

where $\rho(\vec{r})$ and $\kappa(\vec{r})$ are known values describing inhomogeneities in the simulation domain.

Derivation of the FDTD update equation for the scattered pressure field begins

with substituting (4.1) into (4.5) to obtain

$$\frac{\partial}{\partial t} (p^{inc} + p^{scat}) = -\kappa \nabla \cdot (\vec{u}^{inc} + \vec{u}^{scat}) \quad (4.6)$$

where space and time dependencies have been omitted for notational convenience. Substituting (4.3) into (4.6), the time derivative of scattered pressure is given by

$$\frac{\partial p^{scat}}{\partial t} = -\kappa \left(\frac{\partial u_x^{scat}}{\partial x} + \frac{\partial u_y^{scat}}{\partial y} + \frac{\partial u_z^{scat}}{\partial z} \right) + \left(\frac{\kappa}{\kappa_b} - 1 \right) \frac{\partial p^{inc}}{\partial t}. \quad (4.7)$$

where the scattered velocity vector $\vec{u}^{scat} = (u_x^{scat}, u_y^{scat}, u_z^{scat})$ has been written in component form.

Following a similar procedure gives the time derivative of the scattered velocity:

$$\frac{\partial \vec{u}^{scat}}{\partial t} = -\frac{1}{\rho} \nabla p^{scat} + \left(\frac{1}{\rho_b} - \frac{1}{\rho} \right) \nabla p^{inc} \quad (4.8)$$

which, in component form, becomes

$$\begin{aligned} \frac{\partial u_x^{scat}}{\partial t} &= -\frac{1}{\rho} \frac{\partial p^{scat}}{\partial x} + \left(\frac{1}{\rho_b} - \frac{1}{\rho} \right) \frac{\partial p^{inc}}{\partial x} \\ \frac{\partial u_y^{scat}}{\partial t} &= -\frac{1}{\rho} \frac{\partial p^{scat}}{\partial y} + \left(\frac{1}{\rho_b} - \frac{1}{\rho} \right) \frac{\partial p^{inc}}{\partial y} \\ \frac{\partial u_z^{scat}}{\partial t} &= -\frac{1}{\rho} \frac{\partial p^{scat}}{\partial z} + \left(\frac{1}{\rho_b} - \frac{1}{\rho} \right) \frac{\partial p^{inc}}{\partial z}. \end{aligned} \quad (4.9)$$

The required set of acoustic finite difference equations can be directly determined from (4.7) and (4.9), but first, these continuous equations must be expressed in a discrete form over a finite difference grid. Let the discretized form of a continuous

function $\psi(x, y, z, t)$ be given by the following notation

$$\psi_{[i,j,k]}^{[n]} = \psi(i\Delta x, j\Delta y, k\Delta z, n\Delta t) \quad (4.10)$$

where i, j, k are spatial grid coordinates, n is the time coordinate, $\Delta x, \Delta y, \Delta z$ are spatial-grid step-sizes and Δt is the temporal step-size. If the continuous space and time derivatives in (4.7) and (4.9) are approximated by a second-order centered difference of the form [44]

$$\frac{\partial\phi(\xi)}{\partial\eta} \approx \frac{\phi(\xi + \frac{\Delta\eta}{2}) - \phi(\xi - \frac{\Delta\eta}{2})}{\Delta\eta} \quad (4.11)$$

then the acoustic 3D-FDTD update equations become

$$\begin{aligned} p_{[i,j,k]}^{scat [n+\frac{1}{2}]} &= p_{[i,j,k]}^{scat [n-\frac{1}{2}]} - \frac{\kappa_{[i,j,k]}\Delta t}{\Delta h} \left(u_{x [i+\frac{1}{2},j,k]}^{scat [n]} - u_{x [i-\frac{1}{2},j,k]}^{scat [n]} \right. \\ &\quad \left. + u_{y [i,j+\frac{1}{2},k]}^{scat [n]} - u_{y [i,j-\frac{1}{2},k]}^{scat [n]} + u_{z [i,j,k+\frac{1}{2}]}^{scat [n]} - u_{z [i,j,k-\frac{1}{2}]}^{scat [n]} \right) + \Delta t \left(\frac{\kappa_{[i,j,k]}}{\rho_b} - 1 \right) \frac{\partial p^{inc}}{\partial t} \end{aligned} \quad (4.12)$$

$$\begin{aligned} u_{x [i+\frac{1}{2},j,k]}^{scat [n+1]} &= u_{x [i+\frac{1}{2},j,k]}^{scat [n]} \\ &\quad - \frac{\Delta t}{\rho_{[i+\frac{1}{2},j,k]}\Delta h} \left(p_{[i+1,j,k]}^{scat [n+\frac{1}{2}]} - p_{[i,j,k]}^{scat [n+\frac{1}{2}]} \right) + \Delta t \left(\frac{1}{\rho_b} - \frac{1}{\rho_{[i+\frac{1}{2},j,k]}} \right) \frac{\partial p^{inc}}{\partial x} \end{aligned} \quad (4.13)$$

$$\begin{aligned} u_{y [i,j+\frac{1}{2},k]}^{scat [n+1]} &= u_{y [i,j+\frac{1}{2},k]}^{scat [n]} \\ &\quad - \frac{\Delta t}{\rho_{[i,j+\frac{1}{2},k]}\Delta h} \left(p_{[i,j+1,k]}^{scat [n+\frac{1}{2}]} - p_{[i,j,k]}^{scat [n+\frac{1}{2}]} \right) + \Delta t \left(\frac{1}{\rho_b} - \frac{1}{\rho_{[i,j+\frac{1}{2},k]}} \right) \frac{\partial p^{inc}}{\partial y} \end{aligned} \quad (4.14)$$

$$\begin{aligned} u_{z [i,j,k+\frac{1}{2}]}^{scat [n+1]} &= u_{z [i,j,k+\frac{1}{2}]}^{scat [n]} \\ &\quad - \frac{\Delta t}{\rho_{[i,j,k+\frac{1}{2}]\Delta h} \left(p_{[i,j,k+1]}^{scat [n+\frac{1}{2}]} - p_{[i,j,k]}^{scat [n+\frac{1}{2}]} \right) + \Delta t \left(\frac{1}{\rho_b} - \frac{1}{\rho_{[i,j,k+\frac{1}{2}]} \right) \frac{\partial p^{inc}}{\partial z} \end{aligned} \quad (4.15)$$

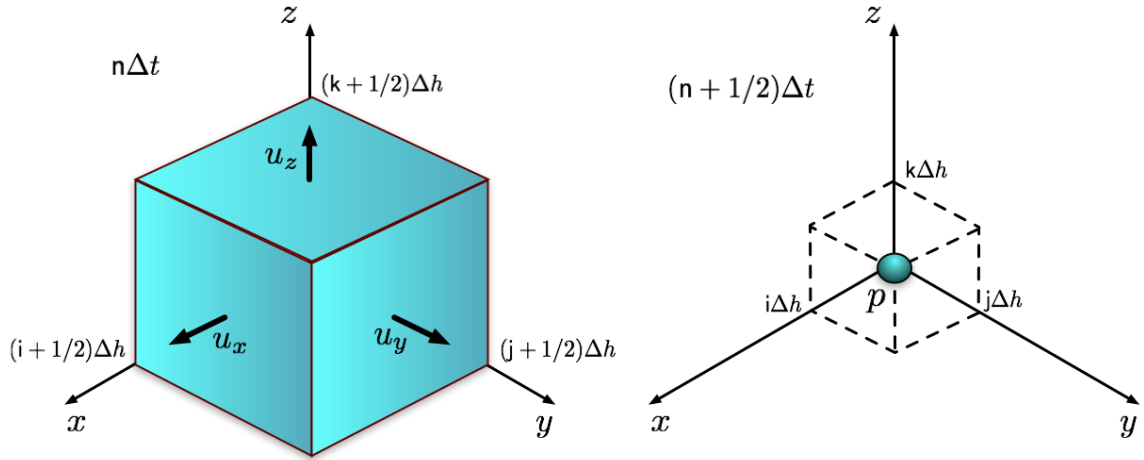


Figure 4.1: 3D-FDTD grid element. The indices shown depict the space-time interlacing of the 3D update equations (4.12)-(4.15).

where $\Delta h = \Delta x = \Delta y = \Delta z$, denote the dimensions of a cubical FDTD-grid element and the derivatives of p^{inc} are not approximated because their analytical forms are assumed to be known. The evaluation indices of update equations (4.12)-(4.15) make for an interlaced leapfrog update scheme as proposed in [44, 45]. A depiction of a 3D grid element is given in Figure 4.1. This update scheme is conditionally stable with Courant-Friedrichs-Lewy (CFL) stability criterion

$$\Delta t < \frac{\Delta h}{c_{max}\sqrt{3}} \quad (4.16)$$

where c_{max} is the maximum speed of longitudinal wave propagation in the simulation domain [44, 45].

The 2D-FDTD update equations are determined directly from (4.12)-(4.15) by

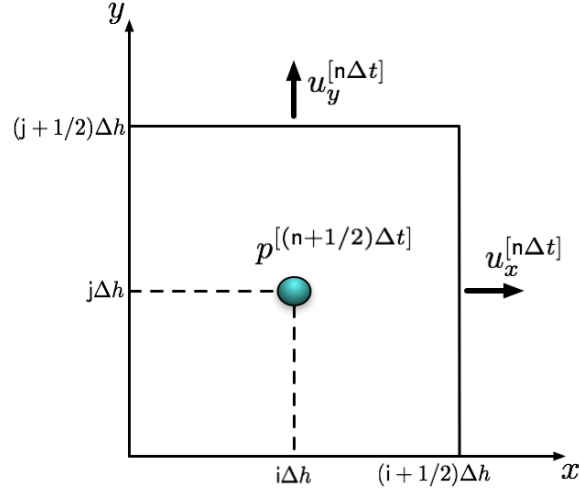


Figure 4.2: 2D-FDTD grid element. The indices shown depict the space-time interlacing of the 2D update equations (4.17)-(4.19).

assuming that the fields do not depend on the z -component:

$$p_{[i,j]}^{scat [n+\frac{1}{2}]} = p_{[i,j]}^{scat [n-\frac{1}{2}]} - \frac{\kappa_{[i,j]}\Delta t}{\Delta h} \left(u_{x [i+\frac{1}{2},j]}^{scat [n]} - u_{x [i-\frac{1}{2},j]}^{scat [n]} + u_{y [i,j+\frac{1}{2}]}^{scat [n]} - u_{y [i,j-\frac{1}{2}]}^{scat [n]} \right) + \Delta t \left(\frac{\kappa_{[i,j]}}{\kappa_b} - 1 \right) \frac{\partial p^{inc}}{\partial t} \quad (4.17)$$

$$u_{x [i+\frac{1}{2},j]}^{scat [n+1]} = u_{x [i+\frac{1}{2},j]}^{scat [n]} - \frac{\Delta t}{\rho_{[i+\frac{1}{2},j]}\Delta h} \left(p_{[i+1,j]}^{scat [n+\frac{1}{2}]} - p_{[i,j]}^{scat [n+\frac{1}{2}]} \right) + \Delta t \left(\frac{1}{\rho_b} - \frac{1}{\rho_{[i+\frac{1}{2},j]}} \right) \frac{\partial p^{inc}}{\partial x} \quad (4.18)$$

$$u_{y [i,j+\frac{1}{2}]}^{scat [n+1]} = u_{y [i,j+\frac{1}{2}]}^{scat [n]} - \frac{\Delta t}{\rho_{[i,j+\frac{1}{2}]} \Delta h} \left(p_{[i,j+1]}^{scat [n+\frac{1}{2}]} - p_{[i,j]}^{scat [n+\frac{1}{2}]} \right) + \Delta t \left(\frac{1}{\rho_b} - \frac{1}{\rho_{[i,j+\frac{1}{2}]}} \right) \frac{\partial p^{inc}}{\partial y} \quad (4.19)$$

The 2D equations also represent an interlaced leapfrog update scheme (see Figure 4.2) which is conditionally stable with CFL stability criterion $\Delta t < \frac{\Delta h}{c_{max}\sqrt{2}}$ [34, 45].

In both the 2D and 3D update equations, the bulk modulus variable, κ , appears

only in pressure field updates and the density variable, ρ , appears only in velocity field updates. The κ values are therefore aligned with the pressure grid and the ρ values are aligned with the velocity grids.

4.3 Scattering from Penetrable Objects

When the FDTD scheme is used to simulate the UST chamber containing nothing but the background medium, the simulation domain is said to be homogeneous. In other words, the bulk modulus, κ , and density, ρ , are kept constant throughout the propagation fluid. If acoustic scattering from an object is considered then the physics of a region of the simulation domain must differ from the background, thereby requiring κ and ρ to vary in space. Such a simulation domain is said to be inhomogeneous.

Inhomogeneous simulation domains in FDTD can cause the maximum longitudinal wave speed, c_{max} , to be undesirably large due to implicit wave speeds forming at the interface between two media. Implicit wave speeds are formed in the FDTD update scheme due to changes in medium parameters at such interfaces. As can be seen in Figure 4.3, the arrangement of grid parameters at the meeting of medium 1 and medium 2 implicitly defines a wave speed of $\sqrt{\kappa_{\alpha'}/\rho_{\alpha}}$ across the boundary. This implicit value can be larger than the user-defined wave speed of either medium. For instance, if the 1D inhomogeneous domain of Figure 4.3 is simulated such that $\kappa_{\alpha} < \kappa_{\alpha'}$ and $\rho_{\alpha} < \rho_{\alpha'}$ then an implicit wave speed is formed at the object boundary ($\sqrt{\kappa_{\alpha'}/\rho_{\alpha}}$) that is greater than either user-defined speed ($\sqrt{\kappa_{\alpha}/\rho_{\alpha}}$ and $\sqrt{\kappa_{\alpha'}/\rho_{\alpha'}}$). This effect can be seen in both 2D and 3D update schemes and can make it difficult to determine the true value of c_{max} for CFL stability.

Another concern arising from implicit wave speeds is the minimum speed, c_{min} , that can be formed. The minimum wavelength of interest is given by $\lambda_{min} = \frac{c_{min}}{f_{max}}$

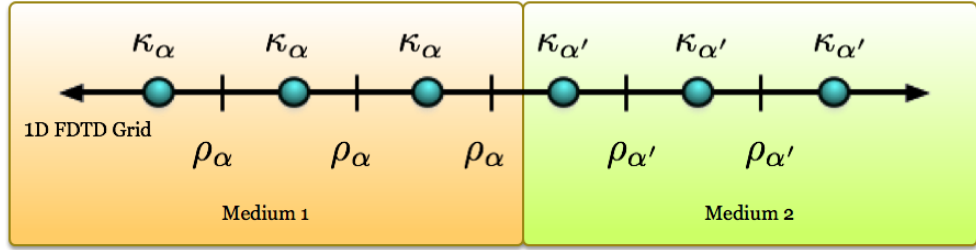


Figure 4.3: Inhomogeneous 1D-FDTD domain at the interface of two media. The parameters κ_α and ρ_α are the properties of medium 1 whereas $\kappa_{\alpha'}$ and $\rho_{\alpha'}$ describe medium 2. Such a grid configuration arises when simulating penetrable objects.

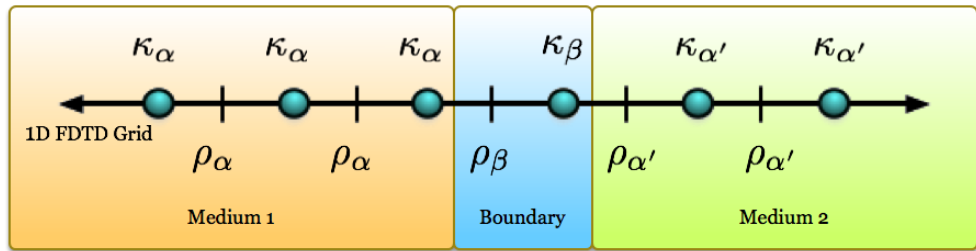


Figure 4.4: Inhomogeneous 1D-FDTD domain with redefined boundary parameters. Adjusting parameter values at the boundary to κ_β and ρ_β is the proposed workaround for the problems caused by implicit wave speeds.

where f_{max} is the maximum frequency of interest. Since it is customary to set $\Delta h \leq \frac{\lambda_{min}}{10}$ for adequate simulation accuracy [34], a lower than expected wave speed at an interface will cause smaller than expected implicit wavelengths to propagate with insufficient accuracy.

Effective treatment of object boundary values is required to remedy the problems caused by implicit wave speeds. A proposed method is to set the boundary values to the average of the respective medium properties $\kappa_\beta = \frac{\kappa_\alpha + \kappa_{\alpha'}}{2}$ and $\rho_\beta = \frac{\rho_\alpha + \rho_{\alpha'}}{2}$ [34] (see Figure 4.4). This works in many cases but implicit speeds larger than c_{max} still arise for certain media combinations and undesirably small implicit speeds are still a problem for high contrast objects.

It is possible to maintain implicit wave speeds below the user-defined c_{max} while

optimizing their lower bound. The solution proposed in this work is to redefine $\kappa_{\alpha'}$ and ρ_{α} at the interface of the media to κ_{β} and ρ_{β} , as shown in Figure 4.4. These boundary values must be determined such that the following conditions are satisfied:

1. $\max(\kappa_{\alpha}, \kappa_{\alpha'}) \geq \kappa_{\beta} \geq \min(\kappa_{\alpha}, \kappa_{\alpha'})$ and $\max(\rho_{\alpha}, \rho_{\alpha'}) \geq \rho_{\beta} \geq \min(\rho_{\alpha}, \rho_{\alpha'})$;
2. implicit wave speeds $c_{\alpha\beta} = \sqrt{\kappa_{\alpha}/\rho_{\beta}}$, $c_{\beta\alpha'} = \sqrt{\kappa_{\beta}/\rho_{\alpha'}}$ and $c_{\beta} = \sqrt{\kappa_{\beta}/\rho_{\beta}}$ are as large as possible but no greater than the user-defined c_{max} .

The first condition is met by splitting the problem into two cases.

Case 1: If $\frac{\kappa_{\alpha}}{\rho_{\alpha'}} \geq \frac{\kappa_{\alpha'}}{\rho_{\alpha}}$ then set $\kappa_{\beta} = \kappa_{\alpha'}$ and $\rho_{\beta} = \rho_{\alpha}$

Case 2: If $\frac{\kappa_{\alpha}}{\rho_{\alpha'}} < \frac{\kappa_{\alpha'}}{\rho_{\alpha}}$ then set $\kappa_{\beta} = \kappa_{\alpha'}$ and $\rho_{\beta} = \rho_{\alpha'}$

As for the second condition, only certain media combinations allow for the flexibility to optimize the object-boundary speeds. Optimization is possible for two special sub-cases that may arise in Case 1.

Case 1a: If $\kappa_{\alpha} > \kappa_{\alpha'}$, $\rho_{\alpha} > \rho_{\alpha'}$ and $\frac{\kappa_{\alpha}}{\rho_{\alpha}} > \frac{\kappa_{\alpha'}}{\rho_{\alpha'}}$ then instead set $\kappa_{\beta} = \frac{\kappa_{\alpha}\rho_{\alpha'}}{\rho_{\alpha}}$

Case 1b: If $\kappa_{\alpha} > \kappa_{\alpha'}$, $\rho_{\alpha} > \rho_{\alpha'}$ and $\frac{\kappa_{\alpha}}{\rho_{\alpha}} < \frac{\kappa_{\alpha'}}{\rho_{\alpha'}}$ then instead set $\rho_{\beta} = \frac{\kappa_{\alpha}\rho_{\alpha'}}{\kappa_{\alpha'}}$

As for Case 2, one possible sub-case can be noted.

Case 2a: If $\kappa_{\alpha} < \kappa_{\alpha'}$, $\rho_{\alpha} < \rho_{\alpha'}$ and $\frac{\kappa_{\alpha}}{\rho_{\alpha}} > \frac{\kappa_{\alpha'}}{\rho_{\alpha'}}$ then instead set $\rho_{\beta} = \frac{\kappa_{\alpha'}\rho_{\alpha}}{\kappa_{\alpha}}$

Case 2 does not support adjustment of κ_{β} because doing so will either violate condition 1 or create overlapping media in the sense $\kappa_{\beta} = \kappa_{\alpha}$ and $\rho_{\beta} = \rho_{\alpha'}$ which is non-physical and disallowed.

By adjusting the parameters at all medium interfaces as described above, the FDTD simulation algorithm can proceed without violating the CFL condition and λ_{min} is optimized. The 1D example presented here can be easily adapted to 2D and 3D grids.

4.4 Source Modelling

The scattered field formulation of the FDTD update equations requires that the incident pressure field, $p^{inc}(\vec{r}, t)$, be imposed onto the simulation domain. This means that the pressure field must be a known function with respect to space and time. Such a function is determined differently for the 2D and 3D cases as described below.

4.4.1 3D Source Model

In 3D-FDTD, a transducer is modelled as a source of acoustic energy originating from a point in space. As such, the incident pressure field function, $p^{inc}(\vec{r}, t)$, must describe an acoustic wave propagating in a homogeneous medium as the result of an applied pressure at a point $\vec{r}_0 = (x_0, y_0, z_0)$. This function must also satisfy the homogeneous acoustic wave equation. The incident pressure field function is therefore written as [27]

$$p_{3D}^{inc}(\vec{r}, t) = \frac{p_f\left(t - \frac{|\vec{r} - \vec{r}_0|}{c_b}\right)}{|\vec{r} - \vec{r}_0|} \quad (4.20)$$

where p_f is a differentiable function of time and $|\cdot|$ is the Euclidean norm.

In order to simulate the enveloped sinusoidal signal generated by the transducers of the UST system, the incident field function is set to the product of a Gaussian function and a sinusoid:

$$p_f(t) = A e^{-\frac{(t-\sigma)^2}{\varsigma}} \sin(\omega t) \quad (4.21)$$

where A is the signal amplitude and ω is the frequency of interest. The constants σ and ς are used to set the signal time-shift and bandwidth, respectively.

4.4.2 2D Source Model

In two dimensions the distribution of pressure in the simulation domain is independent of the z -component. The “2D point-source” for such a situation is effectively a line source parallel to the z -axis [46]. It can be interpreted as a uniform source extending from $z = -\infty$ to $z = \infty$ along a line passing through the source location, $\vec{r}_0 = (x_0, y_0)$. The 2D incident pressure field function has the form

$$p_{2D}^{inc}(\vec{r}, t) = \frac{c_b}{2\pi} \int_{-\infty}^{t - \frac{|\vec{r} - \vec{r}_0|}{c_b}} \frac{p_f(\zeta)}{\sqrt{c_b^2(t - \zeta)^2 - |\vec{r} - \vec{r}_0|^2}} d\zeta \quad (4.22)$$

for a continuous function p_f such that $p_f(t) = 0$ for $t < 0$ [41]. If p_f is set as in (4.21) then the integral in (4.22) becomes difficult to evaluate analytically and it is not feasible to numerically approximate it at every time step of the FDTD algorithm. The incident pressure field for 2D-FDTD is therefore determined by injecting the function (4.21) at the source location in a homogeneous simulation domain and propagated via FDTD. The computed values are differenced as per (4.11) then imposed onto the inhomogeneous simulation domain of interest at every time step.

4.5 Simulation Domain Truncation

The outer boundary of the FDTD grid is terminated with a numerical boundary condition that absorbs acoustic energy reaching the edge of the simulation domain. The boundary condition employed is based on the Mur absorbing boundary condition (ABC) developed for Maxwell’s equations over an interlaced finite-difference grid [47].

The first and second order Mur ABCs at the planar left-hand side boundary of a simulation domain, $x = a$, are given in (4.23) and (4.24), respectively. Both are

written for a scalar field, W , satisfying the homogeneous wave equation [47]:

$$\left(\frac{\partial}{\partial x} - \frac{1}{c_b} \frac{\partial}{\partial t} \right) W|_{x=a} = 0 \quad (4.23)$$

$$\left[\frac{1}{c_b} \frac{\partial^2}{\partial x \partial t} - \frac{1}{c_b^2} \frac{\partial^2}{\partial t^2} - \frac{1}{2} \left(\frac{\partial^2}{\partial y^2} + \frac{\partial^2}{\partial z^2} \right) \right] W|_{x=a} = 0. \quad (4.24)$$

The ABCs given above are for a 3D grid. The corresponding 2D ABCs can be determined from (4.23) and (4.24) by assuming no field variation in the z -direction. Similar boundary conditions can be found for the remaining planar sides of the mesh.

Boundary update equations based on (4.23) and (4.24) are then determined in order to incorporate the ABCs into the FDTD scheme. By setting $W = u_x$, the second-order centered difference approximation, (4.11), gives the first order ABC update equation at boundary $x = a$ as

$$u_{x[a,j,k]}^{scat[n+1]} = u_{x[a+1,j,k]}^{scat[n]} + \frac{c_b \Delta t - \Delta h}{c_b \Delta t + \Delta h} \left(u_{x[a,j,k]}^{scat[n+1]} - u_{x[a,j,k]}^{scat[n]} \right) \quad (4.25)$$

where $\mathbf{a} = a/\Delta h$. Similarly, the second order ABC update equation at boundary $x = a$ is

$$\begin{aligned} u_{x[a,j,k]}^{scat[n+1]} = & -u_{x[a+1,j,k]}^{scat[n-1]} + \frac{c_b \Delta t - \Delta h}{c_b \Delta t + \Delta h} \left(u_{x[a+1,j,k]}^{scat[n+1]} + u_{x[a,j,k]}^{scat[n-1]} \right) \\ & + \frac{2\Delta h}{c_b \Delta t + \Delta h} \left(u_{x[a+1,j,k]}^{scat[n]} + u_{x[a,j,k]}^{scat[n]} \right) \\ & + \frac{(c_b \Delta t)^2}{2\Delta h(c_b \Delta t + \Delta h)} \left(u_{x[a+1,j+1,k]}^{scat[n]} + u_{x[a+1,j-1,k]}^{scat[n]} \right) \\ & + u_{x[a,j+1,k]}^{scat[n]} + u_{x[a,j-1,k]}^{scat[n]} + u_{x[a+1,j,k+1]}^{scat[n]} + u_{x[a+1,j,k-1]}^{scat[n]} \\ & + u_{x[a,j,k+1]}^{scat[n]} + u_{x[a,j,k-1]}^{scat[n]} - 4u_{x[a,j,k]}^{scat[n]} - 4u_{x[a+1,j,k]}^{scat[n]}. \end{aligned} \quad (4.26)$$

Boundary update equations for the remaining planar sides of the simulation domain are determined by terminating u_y and u_z at $y = \text{constant}$ and $z = \text{constant}$ planar boundaries, respectively. Note that first order ABCs are used on the edges (boundary intersections) of the simulation domain because certain second-order terms in (4.26) become unavailable in these regions of the grid.

5

Finite-Element Contrast-Source Inversion

The mathematical formulation of ultrasound imaging using the Finite-Element Contrast-Source Inversion Method (FEM-CSI) is briefly developed in this chapter. It is analogous to work associated with Microwave Tomography (MWT) presented in [9] and adapted to the acoustic case.

There are two parts to FEM-CSI imaging: the forward problem and the inverse problem. The forward problem involves determining the solution to a governing partial differential equation via the finite element method (FEM). The inverse problem is solved using contrast-source inversion (CSI), one of several techniques developed for tomographic imaging.

5.1 Equation Governing the Acoustic Problem

For the MWT case, a governing partial differential equation is derived involving only the electric field in the frequency domain. This equation is found to be the inhomogeneous Helmholtz equation under the assumptions that the problem domain is free of charge and that any materials therein are non-magnetic [9]. It will be shown that, under analogous assumptions, such a governing equation can be derived for the acoustic case.

A governing equation for Ultrasound Tomography (UST) is needed in terms of incremental pressure. In order to more easily transition from MWT, this quantity is made analogous to the electric field (see section 3.3). It is assumed that the problem domain is free of any local pressure gradients and that the density is constant throughout. These are analogous to the MWT assumptions of a charge-free domain and that all contained materials are non-magnetic, respectively. The relation between constant domain-density and non-magnetic materials may not be immediately obvious and thus will be clarified in the following derivation. Note that in this section, the derivation of the governing equation is performed for a two-dimensional configuration of the acoustic problem, nevertheless it can be easily extended to three dimensions.

We begin by removing time dependency from the conservation equations. Pressure and velocity are assumed to be time-harmonic with an $\exp(j\omega t)$ time dependency, where $j^2 = -1$ and $\omega = 2\pi f$ is the angular frequency for a frequency of interest f . Thus, derivatives with respect to time in (3.18) and (3.19) are replaced by $j\omega$, allowing the conservation equations to be considered in their frequency-domain form:

$$\nabla \cdot \vec{u}(\vec{r}) = \frac{-j\omega p(\vec{r})}{\kappa(\vec{r})} \quad (5.1)$$

$$\nabla p(\vec{r}) = -j\omega \rho(\vec{r}) \vec{u}(\vec{r}) \quad (5.2)$$

where $\vec{r} = (x, y)$ is the 2D position vector. Let $\vec{u} = u_x \hat{x} + u_y \hat{y}$, where \hat{x} and \hat{y} are unit vectors along the 2D Cartesian coordinate axes. With some rearrangement and

separation of \vec{u} into its components, (5.1) and (5.2) may then be rewritten as

$$\frac{\partial u_x}{\partial x} + \frac{\partial u_y}{\partial y} = \frac{-j\omega p}{\kappa} \quad (5.3)$$

$$u_x = \frac{j}{\omega\rho} \frac{\partial p}{\partial x} \quad (5.4)$$

$$u_y = \frac{j}{\omega\rho} \frac{\partial p}{\partial y} \quad (5.5)$$

where \vec{r} is removed for notational convenience. Substituting (5.5) and (5.4) into (5.3) and multiplying by $j\omega$, the following is obtained:

$$\frac{\partial}{\partial x} \left(\frac{1}{\rho} \frac{\partial p}{\partial x} \right) + \frac{\partial}{\partial y} \left(\frac{1}{\rho} \frac{\partial p}{\partial y} \right) = \frac{-\omega^2}{\kappa} p. \quad (5.6)$$

Applying the product rule for differentiation to the terms on the left-hand side of (5.6) gives

$$\frac{1}{\rho} \frac{\partial^2 p}{\partial x^2} + \frac{1}{\rho} \frac{\partial^2 p}{\partial y^2} - \frac{1}{\rho^2} \frac{\partial \rho}{\partial x} \frac{\partial p}{\partial x} - \frac{1}{\rho^2} \frac{\partial \rho}{\partial y} \frac{\partial p}{\partial y} = \frac{-\omega^2}{\kappa} p \quad (5.7)$$

and after further simplifying we arrive at a partial differential equation for a pressure wave in space,

$$\nabla^2 p(\vec{r}) + \frac{\omega^2 \rho(\vec{r})}{\kappa(\vec{r})} p(\vec{r}) - \frac{1}{\rho(\vec{r})} \nabla \rho(\vec{r}) \cdot \nabla p(\vec{r}) = 0 \quad (5.8)$$

where ∇^2 is the Laplacian operator and “ \cdot ” denotes the dot-product.

A scalar Helmholtz equation for acoustics can be obtained from equation (5.8) by setting the domain density $\rho(\vec{r}) = \rho_b$, a constant, thereby causing $\nabla \rho(\vec{r}) = \nabla \rho_b = 0$. The governing partial differential equation is thus

$$\nabla^2 p(\vec{r}) + \frac{\omega^2 \rho_b}{\kappa(\vec{r})} p(\vec{r}) = 0. \quad (5.9)$$

Recalling the analogy established between density and permeability, it becomes

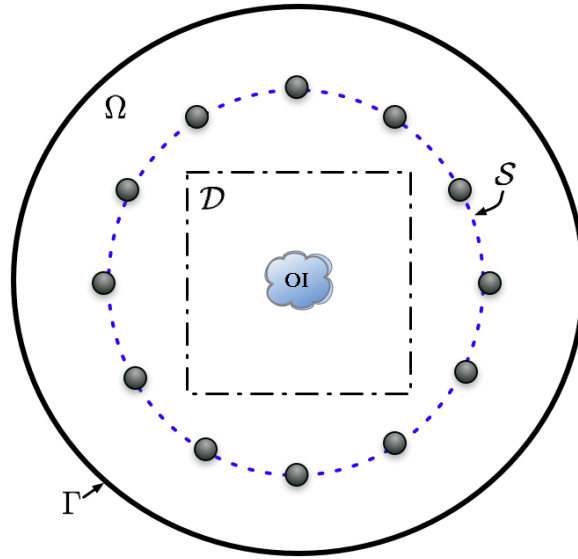


Figure 5.1: Geometrical model of the imaging problem. The problem domain is denoted by Ω and the imaging domain by \mathcal{D} . The enclosing boundary is the surface, Γ , whereas the transmitters and receivers are located on the measurement surface, \mathcal{S} .

clear from the derivation above that constant domain density is related to the MWT assumption that all materials be non-magnetic. This theoretically implies that an object of interest must have the same density as the background medium for proper inversion via FEM-CSI.

5.2 Problem Formulation

The scalar Helmholtz equation for acoustics, (5.9), is analogous to the governing equation of the 2D Transverse-Magnetic (TM) problem for MWT. As such, the inverse problem formulation for the acoustic case will be presented in a manner analogous to the 2D TM problem presented in [48].

We consider an unknown object-of-interest (OI) within a bounded imaging domain, \mathcal{D} , as depicted in Figure 5.1. The surrounding problem boundary, Γ , can be of any shape, size or type (Dirichlet, Neumann, Cauchy, etc.), depending on the imaging

apparatus being modelled. The acoustical properties of the homogeneous background medium are known everywhere in Γ and the density of the OI is assumed to be that of the background medium. The imaging domain \mathcal{D} is successively insonified by its surrounding transmitters. The transmitters are modelled as point sources with incident pressure field, $p_\tau^{inc}(\vec{r})$, produced by transmitter τ at position \vec{r}_τ . This is done by introducing a singularity at $\vec{r}_\tau \in \Gamma$ via the Dirac Delta Function, $\delta(\vec{r} - \vec{r}_\tau)$ [27]. The governing equation, (5.9), is then evaluated over the problem domain, Ω , as follows

$$\nabla^2 p_\tau^{inc}(\vec{r}) + k_b^2 p_\tau^{inc}(\vec{r}) = -\delta(\vec{r} - \vec{r}_\tau), \quad (5.10)$$

where $k_b = \omega \sqrt{\frac{\rho_b}{\kappa_b}}$ is the homogeneous background wavenumber for a constant bulk modulus κ_b .

With the OI present in the imaging domain, \mathcal{D} , the total pressure field, $p_\tau^{tot}(\vec{r})$, satisfies the governing equation, (5.9), as

$$\nabla^2 p_\tau^{tot}(\vec{r}) + k^2(\vec{r}) p_\tau^{tot}(\vec{r}) = -\delta(\vec{r} - \vec{r}_\tau), \quad (5.11)$$

where $k(\vec{r}) = \omega \sqrt{\frac{\rho_b}{\kappa(\vec{r})}}$ is the inhomogeneous wavenumber. It then follows that the scattered field, defined as $p_\tau^{scat} \triangleq p_\tau^{tot} - p_\tau^{inc}$, satisfies the inhomogeneous scalar Helmholtz equation:

$$\nabla^2 p_\tau^{scat}(\vec{r}) + k_b^2(\vec{r}) p_\tau^{scat}(\vec{r}) = -k_b^2 \varphi_\tau(\vec{r}) \quad (5.12)$$

where φ_τ is the contrast-source variable defined as

$$\varphi_\tau(\vec{r}) \triangleq p_\tau^{tot}(\vec{r}) \chi(\vec{r}) \quad (5.13)$$

with contrast, χ , denoted as

$$\chi(\vec{r}) = \frac{c_b^2 - c^2(\vec{r})}{c^2(\vec{r})}. \quad (5.14)$$

Here c_b is the speed of sound in the background medium and $c(\vec{r})$ the speed of sound within the OI.

The objective of CSI is to iteratively update the contrast and the contrast-source variables independently, using scattered field values available on a measurement surface, \mathcal{S} , located within the problem domain (see Figure 5.1). The variables are updated such that the CSI cost functional is minimized [49]. In order to express this functional in the context of FEM-CSI, the inhomogeneous scalar Helmholtz equation, (5.12), is written in operator form:

$$\mathcal{L} \{p_\tau^{scat}(\vec{r})\} = -k_b^2 \varphi_\tau(\vec{r}). \quad (5.15)$$

Its inverse is of particular interest and is defined as

$$\mathcal{L}^{-1} \{-k_b^2 \varphi_\tau(\vec{r})\} = p_\tau^{scat}(\vec{r}), \quad (5.16)$$

which gives the scattered field values in the problem domain, Ω , for a given background wavenumber and contrast source. In addition, two more operators are introduced. The first, $\mathcal{M}_\mathcal{S}$, is responsible for generating field values on the measurement surface, \mathcal{S} , from the scattered field, $p_\tau^{scat}(\vec{r}) \in \Omega$. The second, denoted $\mathcal{M}_\mathcal{D}$, also operates on $p_\tau^{scat}(\vec{r})$ but instead returns pressure field values in \mathcal{D} . At a computational level, the aforementioned operators are represented as matrices which are determined via the FEM.

These operators are then used to define the FEM-CSI cost functional [9]:

$$\begin{aligned} \mathcal{C}(\chi(\vec{r}), \varphi_\tau(\vec{r})) = & \frac{\sum_\tau \|p_{\tau,cal}^{scat}(\vec{r}) - \mathcal{M}_S \mathcal{L}^{-1}\{-k_b^2 \varphi_\tau(\vec{r})\}\|_{\mathcal{S}}^2}{\sum_\tau \|p_{\tau,cal}^{scat}(\vec{r})\|_{\mathcal{S}}^2} \\ & + \frac{\sum_\tau \|\chi(\vec{r}) p_\tau^{inc}(\vec{r}) - \varphi_\tau(\vec{r}) + \chi(\vec{r}) \mathcal{M}_D \mathcal{L}^{-1}\{-k_b^2 \varphi_\tau(\vec{r})\}\|_{\mathcal{D}}^2}{\sum_\tau \|\chi(\vec{r}) p_\tau^{inc}(\vec{r})\|_{\mathcal{D}}^2} \end{aligned} \quad (5.17)$$

where the subscript *cal* indicates calibrated data, $\|\cdot\|_{\mathcal{S}}$ is the L_2 -norm over the surface \mathcal{S} and $\|\cdot\|_{\mathcal{D}}$ is the L_2 -norm over domain \mathcal{D} . The cost functional is minimized by successively updating the contrast and contrast-source by a conjugate gradient method. Information about the acoustical properties of the imaging domain is held in the contrast variable. From (5.14), the contrast gives reconstructed spatial speeds which can be used to build a map, or image, of this quantity as it changes in space. Using the relation for speed, $c(\vec{r}) = \sqrt{\kappa(\vec{r})/\rho_b}$, a bulk modulus map is also available.

5.3 Special Considerations for Acoustics

In the case of MWT, the inversion algorithm achieves best results when reconstructing low-contrast objects [9]. This is also true for UST, but due to the significantly shorter wavelength of ultrasound, object size must also be taken into consideration. Experience indicates that low-contrast objects with a dimension measuring nearly 10 wavelengths cannot be properly reconstructed with FEM-CSI and this number is further reduced when the object contrast is increased [50]. A similar effect can be seen when applying diffraction tomographic imaging techniques to objects several wavelengths in size [51].

In order to estimate the maximum dimensions of an OI used in ultrasound imaging, experimentation with simulated low-contrast objects is performed. Square objects

of different sizes with a contrast of 0.02 are simulated with the FEM in a domain representing an unbounded UST chamber. The simulation frequency is set to 1.5 MHz and the background sound speed is set to 1500 m/s. These parameter values are seen in practice and conveniently give a wavelength of 1 mm. Inversions of several square objects with sizes in the range of 1 mm to 6 mm are shown in Figure 5.2. It can be observed that the simulation data is properly reconstructed for all examples except the 6 mm square. It is instead reconstructed as a somewhat circular object with a radius of approximately 1.5 mm and incorrect contrast, as shown in Figure 5.2(d). A similar effect is observed for larger objects and places a limit on items that can be used for imaging due to their dimensions. Based on these findings, it appears that an item's largest acceptable dimension for imaging with FEM-CSI should be limited to 6 wavelengths, approximately the largest dimension of the 4 mm square.

Another limitation arises due to the assumption of constant domain density as described in section 5.1. It is a requirement imposed by the governing equation of the imaging algorithm and implies that an ideal OI must have density equal to that of the background medium.

In practice, it is difficult to exactly satisfy the constant density constraint when imaging physical objects. For this reason, it becomes important to know the limits of acceptable density disagreement. In order to estimate the extent of these limits, low-contrast square objects with different densities are simulated using FDTD in an environment representing the UST chamber. The metric utilized for this evaluation is the percentage density discrepancy defined as $100 \times |\rho_b - \rho|/\rho_b$, where ρ_b and ρ are the average density of the background medium and of the OI, respectively. The object size is kept constant for all simulations and the background density is fixed to 1 g/cm^3 , the approximate density of water.

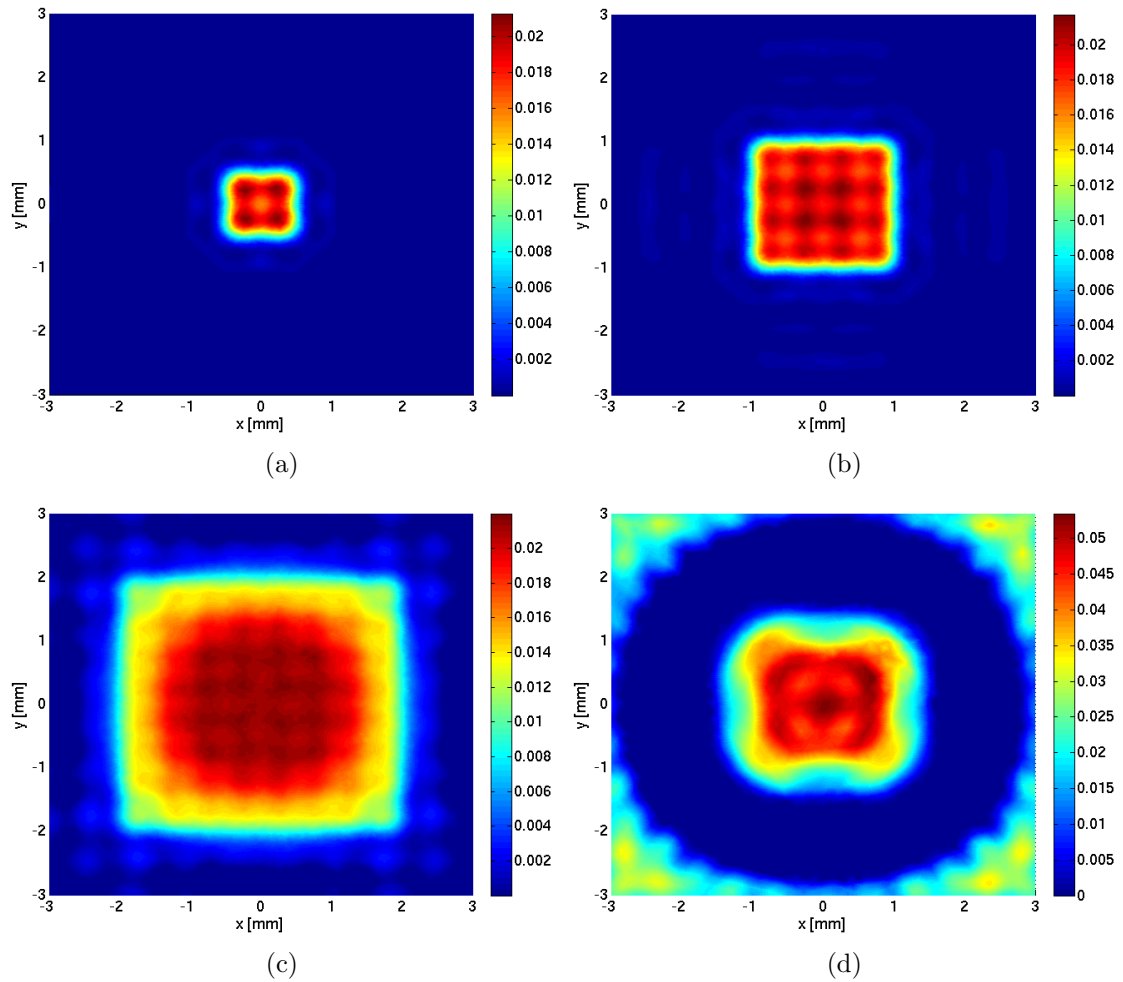


Figure 5.2: Inversion results of synthetic data for different object sizes. The frequency of interest is 1.5 MHz and the background wave speed is 1500 m/s. The resulting wavelength measures 1 mm. The colour scale denotes the reconstructed contrast values. It is shown that an object's largest dimension should be no greater than 6 wavelengths for proper reconstruction. (a) Inversion result for a 1 mm square. (b) Inversion result for a 2 mm square. (c) Inversion result for a 4 mm square. (d) Inversion result for a 6 mm square.

Reconstructions of 2.5 mm squares for different density discrepancies are shown in Figure 5.3. The reference inversion, where the density discrepancy is 0%, is given in Figure 5.3(a). It can be seen in this figure that the reconstructed dimensions are correct. The expected contrast of 0.02 is also correctly determined as illustrated by the colour scale. The other sub-figures show a degradation in inversion results as the density discrepancy is increased. Figure 5.3(d) gives the inversion result for a density discrepancy of 5%. It is clear that the magnitude of such a density disagreement is unacceptable because the resultant contrast significantly diverges from the expected value of 0.02 within the reconstructed object. The inversion result for a density discrepancy of 3% is shown in Figure 5.3(c). It can be observed that the resultant contrast is near the expected value and that it is reasonably uniform throughout the reconstructed object. In light of these observations, the density discrepancy should be kept below 3% for meaningful shape and contrast reconstruction with FEM-CSI.

It is interesting to note that for all reconstructions shown in Figure 5.3, the outer boundaries of the simulated object are distinguishable from the background and the object dimensions are correctly determined. This result suggests that the shape reconstruction of objects with high density discrepancy is still possible though resultant contrast information would not be meaningful.

The findings of this section indicate that any physical test object used to validate a calibration procedure should conform to the limitations discussed above. An object suitable for imaging with FEM-CSI must have low contrast, its largest dimension should be no greater than 6 wavelengths and it should have a density discrepancy of less than 3%. It has been shown through simulation that the use of an object which does not conform to these limitations is likely to produce poor inversion results. A similar outcome can be expected from the use of such objects in an experimental

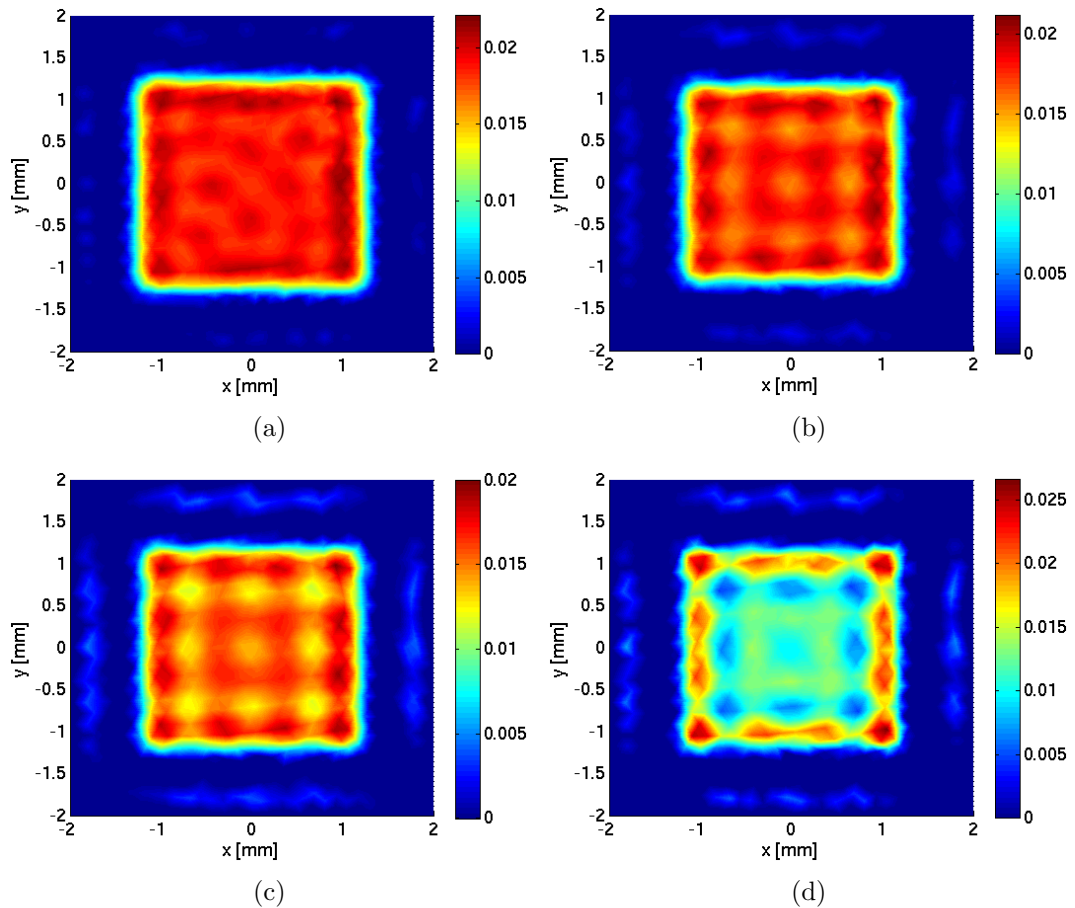


Figure 5.3: Inversion results of synthetic data for objects with different density discrepancies. The OI is a 2.5 mm square with a contrast of 0.02. The colour scale denotes the reconstructed contrast values. It is shown that objects used for imaging should have a density discrepancy no greater than 3% in order to obtain meaningful inversion results. (a) Inversion result for a 0% density discrepancy. (b) Inversion result for a 1% density discrepancy. (c) Inversion result for a 3% density discrepancy. (d) Inversion result for a 5% density discrepancy.

scenario, regardless of the employed calibration technique, and can therefore provide misleading information about the effectiveness of an applied calibration method. Thus, the observations made in this section provide guidelines for the selection of suitable objects when validating the calibration procedures presented in the next chapter.

6

Calibration

Calibration is applied to measured data before it is passed to the inversion algorithm. The acquired data is thus conditioned to meet certain requirements necessary for proper image reconstruction. In the context of this work, calibration is also known as the signal-processing step.

Data collected by the UST system are in the time domain. They are cast to the frequency domain via Fast Fourier Transform (FFT) [52] and calibrated for imaging with the FEM-CSI algorithm. It is for this reason that the concepts presented in this chapter are chiefly developed using frequency-domain principles. Nonetheless, time-domain techniques are used to determine other information required by the inversion algorithm and are detailed in section 6.6. This chapter concludes with summaries of the two presented calibration procedures.

Details regarding the transformation of time-domain data to the frequency-domain are given in Appendix B.

6.1 System Model

A model of the UST system described in Chapter 2 is developed in this section. This model is used as a tool to identify sources of measurement error as well as to determine the type of conditioning that is required to correctly prepare the data

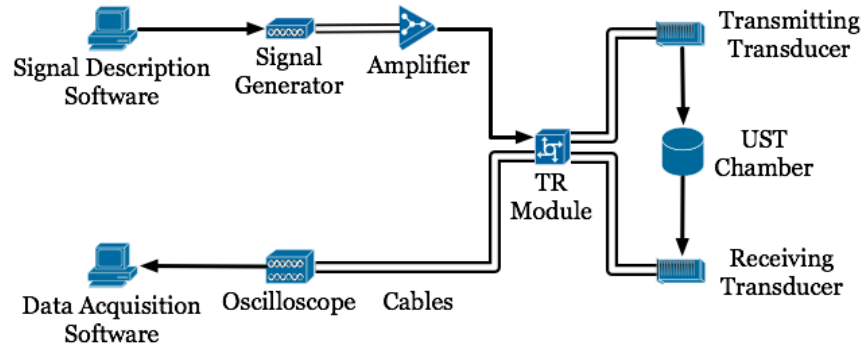


Figure 6.1: A representative block-diagram of the UST system.

for inversion. Though the following model is developed for a particular apparatus, the principles and derived methodology may be applied to a variety of tomography systems.

A representative block-diagram of the UST system for a particular transmitter-receiver pair is shown in Figure 6.1. If all depicted devices are assumed to operate in a linear fashion then the diagram of Figure 6.1 may be regarded as a linear time-invariant (LTI) system. Linearity of the system components may be assumed so long as their linear operating ranges are respected. Time-invariance is achieved by allowing system components to “warm-up” until they reach a steady operating state before taking measurements.

Based on LTI system principles developed in [53], each system component shown in Figure 6.1 can be represented as a *system function* (also known as *transfer function*) with its own *frequency response*. These functions describe how the phase and magnitude of a signal are transformed when passing through a device, as a function of frequency. For the purposes of this work, a simplified system model is created by grouping together the components on either side of the UST chamber into two system functions. Input devices, appearing before the chamber, are grouped into system function $G(\omega)$ and output devices, placed after the chamber, are grouped into $K(\omega)$.

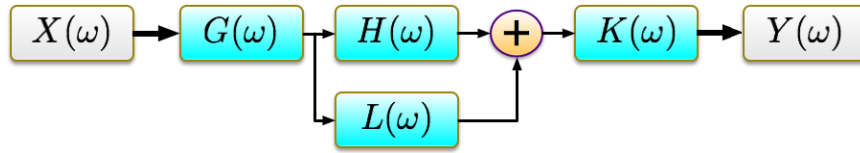


Figure 6.2: A simplified block-diagram of the UST system. Chamber input devices are grouped in system function $G(\omega)$ and output devices are grouped in $K(\omega)$. The chamber system function is represented as the sum of $H(\omega)$ and $L(\omega)$. The term $X(\omega)$ represents the frequency-domain input to the system and $Y(\omega)$ denotes the output. See (6.1) for the resulting system equation.

Note that the system function of the transmitting transducer is absorbed into $G(\omega)$ and that of the receiving transducer into $K(\omega)$. As for the chamber, it is represented as a sum of system functions. Signal propagation between the transmitter-receiver pair in an unbounded medium is represented by the system function $H(\omega)$. Whereas reflections from chamber walls and other fixed mounting implements that create multiple signal paths (multipath) between the transducer pair are subsumed in $L(\omega)$. A block-diagram of the simplified system model is shown in Figure 6.2. In this figure, the frequency-domain input to the system is represented by $X(\omega)$ and the resulting output is denoted by $Y(\omega)$.

The system equation for the simplified UST-system model shown in Figure 6.2, may be written as

$$Y(\omega) = X(\omega)G(\omega) (H(\omega) + L(\omega)) K(\omega) \quad (6.1)$$

where $X(\omega)$ is a known input signal. Due to the LTI nature of the system model, the terms in equation (6.1) are commutative, distributive and associative [53]. Using these properties the following system equation is obtained:

$$Y = XGK(H + L) \quad (6.2)$$

where ω is set to a particular frequency of interest and is removed for notational convenience. In this form the system functions have a phasor representation and so phasor-arithmetic may be employed [54].

6.2 Calibration Coefficients

Data that is to be inverted by FEM-CSI must conform to certain criteria based on the idealized system model being assumed in the algorithm. When creating synthetic data, the forward solver parameters may be adjusted so as to very nearly, if not exactly, comply with these criteria. This is not so easily the case with experimental data. A significant effort is made to conform to inversion algorithm parameters during data collection but further improvements can be made. These improvements are applied to the measured data through calibration by means of a multiplicative constant: the calibration coefficient.

The FEM-CSI algorithm is designed to invert scattered field data for which a reasonable model of the measurement system is assumed. This idealized system model is used in the forward problem and in the inverse problem. It is used to compute $p_{\tau}^{inc}(\vec{r})$ in the FEM-CSI cost functional and is implicitly included in the operators. If convergence of the algorithm is to be expected, the calibrated data must conform to the assumed system model and vice versa. Thus, an appropriate model is chosen to represent the measurement system and calibration is applied to adapt the data to this ideal model. The calibration principles presented in this chapter are, in effect, techniques that use calibration coefficients to reduce the extent to which the numerical model used in FEM-CSI deviates from the actual measurement system. Such a deviation is termed modelling error.

In this work, an ideal system model adheres to the following assumptions:

- Modelled fields satisfy (5.9), the scalar Helmholtz equation.
- Measurements are made in an unbounded medium.
- The problem domain density is constant.
- Pressure fields have known amplitude and zero phase at their points of origin.
- Pressure fields are measured at idealized observation points.

A system model derived from these assumptions does not support the presence of UST-chamber walls, and the use of transducers, cables and other measurement equipment. It is therefore the role of calibration coefficients to remove these effects and reconcile collected data with the idealized system model.

The ideal system model can be represented with phasor notation by applying the assumptions mentioned above to (6.2) as follows. We first denote a steady-state transmitted signal with known amplitude and zero phase at a frequency of interest as X_0 . Next we note that multipath noise is non-existent when measurements are made in an unbounded medium, therefore $L = 0$. In addition, there are no magnitude and phase changes due to transducers and measurement equipment and so $G = K = 1 \angle 0$. By applying these constraints to (6.2) the ideal system model can be represented by the following equation:

$$Y_{mod} = X_0 H_{mod} \tag{6.3}$$

where H_{mod} is a model system function describing signal propagation between two points in an unbounded medium. As such, the ideal system equation may be written

for incident, scattered and total fields as:

$$Y_{mod}^{inc} = X_0 H_{mod}^{inc} \quad (6.4)$$

$$Y_{mod}^{scat} = X_0 H_{mod}^{scat} \quad (6.5)$$

$$Y_{mod}^{tot} = X_0 H_{mod}^{tot} \quad (6.6)$$

where H_{mod}^{inc} represents signal propagation in a homogeneous medium, H_{mod}^{scat} models scattering in an inhomogeneous domain and $H_{mod}^{tot} = H_{mod}^{inc} + H_{mod}^{scat}$.

Noting that input to the FEM-CSI algorithm is measured scattered field data, the ideal system model indicates that data ready for inversion should be adapted to the form of Y_{mod}^{scat} as shown in (6.5). It then becomes evident that the required calibrated data is effectively $X_0 H_{mod}^{scat}$ and it must be extracted from the scattered field form of (6.2). The following sections explain how calibration coefficients are applied to multiplicatively isolate $X_0 H_{mod}^{scat}$ from measured scattered data.

6.3 Incident Field Calibration Principle

An incident field calibration refers to the determination of calibration coefficients using measured incident field data. Recall that incident field data is measured with the object of interest removed from the chamber, leaving only the propagation medium and apparatus. This section describes the calibration procedure on data measured for a single transmitter-receiver pair at a frequency of interest. A full system calibration is obtained when this procedure is applied to each transducer pair.

The incident field calibration of FDTD simulation data is first presented to illustrate the application of this procedure. The following subsection covers the case of calibrating data measured by the UST system.

6.3.1 Calibrating FDTD Data

It is difficult to set the source function to the phasor equivalent of X_0 in FDTD because it is generated in the time-domain. As a consequence, FDTD-generated simulation data needs to be calibrated if inversion results are to be successful.

We begin by defining system equations for the FDTD incident and total field data based on (6.2). The simulation is carried out assuming an absorbing boundary condition terminating a space containing the object of interest. The space is otherwise filled with the homogeneous background medium (i.e. non-existent measurement equipment). This implies that multipath is ignored and that $G = K = 1 \angle 0$. The incident and total field system-equations for the FDTD simulation are therefore written as

$$Y^{inc} = XH^{inc} \quad (6.7)$$

$$Y^{tot} = XH^{tot} \quad (6.8)$$

where X is the phasor representation of the source signal. Scattered field information can be directly obtained from the above equations as

$$\begin{aligned} Y^{scat} &= Y^{tot} - Y^{inc} \\ &= X(H^{tot} - H^{inc}) \\ &= XH^{scat}. \end{aligned} \quad (6.9)$$

It is the value X_0H^{scat} that is to be passed as input to the inversion algorithm. We therefore require a calibration coefficient, C , such that $CY^{scat} \rightarrow X_0H^{scat}$.

When applying the incident field calibration, the calibration coefficient is set to

the ratio of the ideal incident field and the measured incident field [18]:

$$C = \frac{Y_{mod}^{inc}}{Y^{inc}} = \frac{X_0 H_{mod}^{inc}}{X H^{inc}}. \quad (6.10)$$

The scattered field, Y^{scat} , can then be calibrated by applying C to give the following:

$$\begin{aligned} Y^{cal} &= C Y^{scat} \\ &= \frac{X_0 H_{mod}^{inc}}{X H^{inc}} X H^{scat} \\ &= \frac{H_{mod}^{inc}}{H^{inc}} X_0 H^{scat}. \end{aligned} \quad (6.11)$$

This result shows that the effectiveness of the incident field calibration, when applied to FDTD data, is directly affected by modelling error due to the ratio H_{mod}^{inc}/H^{inc} . The value of $X_0 H^{scat}$ is better isolated from the data as this ratio approaches unity. This implies that H_{mod}^{inc} must adequately model the incident field system-function inherent in the FDTD simulation for effective calibration. It is interesting to note that this analysis shows we need only characterize H^{inc} , indicating that this calibration technique is independent of the time-domain source function used in the simulation.

6.3.2 Calibrating UST-System Data

The incident field calibration procedure for measured data is similar to that of FDTD-simulated data. The major difference is that many terms in equation (6.2) cannot be ignored. Consequently, the measured incident and total field system-equations

appear as follows

$$Y^{inc} = X'(H^{inc} + L) \quad (6.12)$$

$$Y^{tot} = X'(H^{tot} + L) \quad (6.13)$$

where $X' = XGK$ for notational convenience. The term Y^{inc} represents the field measured by the UST-system when the object of interest is not present in the UST chamber and H^{inc} is the transfer function of the physical background medium between the transmitter-receiver pair under consideration. The term Y^{tot} represents the measured field when the object of interest is placed in the UST chamber and H^{tot} is the associated transfer function between the same transducer pair.

Scattered field information can be directly obtained from the above equations:

$$\begin{aligned} Y^{scat} &= Y^{tot} - Y^{inc} \\ &= X'(H^{tot} + L - H^{inc} - L) \\ &= X'H^{scat}. \end{aligned} \quad (6.14)$$

It is interesting to note that multipath effects are removed from scattered field data due to the definition of Y^{scat} in terms of the incident and total fields.

We now require a calibration coefficient, C , such that $CY^{scat} \rightarrow X_0H^{scat}$. As before, the calibration coefficient is set to the ratio of the ideal incident field and the measured incident field:

$$C = \frac{Y_{mod}^{inc}}{Y^{inc}} = \frac{X_0H_{mod}^{inc}}{X'(H^{inc} + L)}. \quad (6.15)$$

The scattered field, Y^{scat} , can then be calibrated by applying C as follows:

$$\begin{aligned}
 Y^{cal} &= CY^{scat} \\
 &= \frac{X_0 H_{mod}^{inc}}{X'(H^{inc} + L)} X' H^{scat} \\
 &= \frac{H_{mod}^{inc}}{H^{inc} + L} X_0 H^{scat}.
 \end{aligned} \tag{6.16}$$

This result shows that the incident field calibration is independent of the chosen source function, X . It also shows that the effects of transducers and other measurement equipment can be removed from measured data with an appropriate model for $H^{inc} + L$. Effective incident field calibration of measured data thus requires H_{mod}^{inc} to characterize physical ultrasound waves and their reflections from the UST chamber wall.

The presence of multipath, L , in the measured incident field is problematic for calibration because it is not supported by the ideal model assumed in the FEM-CSI algorithm. Recall from section 6.2 that H_{mod}^{inc} adheres to the assumption that measurements are made in an unbounded medium. This means that multipath is not accounted for when applying the incident field calibration. If multipath is not in some way reduced, its presence may cause significant modelling error and result in poor image reconstruction. It is therefore removed from measured data by other methods as explained in section 6.5.1.

6.4 Scattered Field Calibration Principle

A scattered field calibration refers to the determination of calibration coefficients using measured scattered field data from a known calibration object. The acoustical response of the calibration object must also be modelled as part of this scheme. This

section describes the scattered field calibration procedure on data measured for a single transmitter-receiver pair at a frequency of interest. A full system calibration is obtained when this procedure is applied to each transducer pair.

The scattered field calibration can be regarded as an extension of the principles used for the incident field calibration. For this reason, the scattered field calibration of FDTD simulation data will be omitted and only the more general procedure for measured data is presented. We begin in a manner similar to the procedure of section 6.3.2, by defining the required system equations based on (6.2) as follows

$$Y^{inc} = X'(H^{inc} + L) \quad (6.17)$$

$$Y^{tot} = X'(H^{tot} + L) \quad (6.18)$$

$$\mathbb{Y}^{tot} = X'(\mathbb{H}^{tot} + L). \quad (6.19)$$

Here, (6.19) is the system equation for the calibration object. The term \mathbb{Y}^{tot} represents the field measured by the UST-system when the calibration object is present in the UST chamber and \mathbb{H}^{tot} is the associated transfer function between the transmitter-receiver pair under consideration.

Scattered field information can be directly obtained from the above equations:

$$Y^{scat} = Y^{tot} - Y^{inc} = X'H^{scat} \quad (6.20)$$

$$\mathbb{Y}^{scat} = \mathbb{Y}^{tot} - Y^{inc} = X'\mathbb{H}^{scat}. \quad (6.21)$$

Note that the same incident field measurement is used for the determination of both scattered fields.

A calibration coefficient, C , is required to multiplicatively isolate $X_0 H^{scat}$ from Y^{scat} . The value of C used for the scattered field calibration is the ratio of the

calibration object model and the measured calibration object data [18]:

$$C = \frac{Y_{mod}^{scat}}{Y^{scat}} = \frac{X_0 \mathbb{H}_{mod}^{scat}}{X' \mathbb{H}^{scat}} \quad (6.22)$$

The calibration coefficient is then applied to the scattered field measurement of the unknown object in order to obtain calibrated data:

$$\begin{aligned} Y^{cal} &= CY^{scat} \\ &= \frac{X_0 \mathbb{H}_{mod}^{scat}}{X' \mathbb{H}^{scat}} X' H^{scat} \\ &= \frac{\mathbb{H}_{mod}^{scat}}{\mathbb{H}^{scat}} X_0 H^{scat}. \end{aligned} \quad (6.23)$$

This result shows that the effectiveness of the scattered field calibration is directly affected by modelling error due to the ratio $\mathbb{H}_{mod}^{scat}/\mathbb{H}^{scat}$. The value of $X_0 H^{scat}$ is better isolated from the measured data as this ratio approaches unity. This implies that the effects of transducers and other measurement equipment can be removed from measured data with an appropriate model for \mathbb{H}^{scat} . This analysis also shows that we need only characterize ultrasound scattering from the calibration object and that the time-domain source function used to insonify the target is of little concern.

6.5 Modelling Acoustic Fields for Calibration

As seen in previous sections, the calibration techniques presented in this work require acoustic fields to be described by idealized frequency-domain models. This section discusses the models used in both incident and scattered field calibrations.

6.5.1 Incident Field Model

The incident field calibration scheme makes use of an idealized model, H_{mod}^{inc} , to approximate $H^{inc} + L$ of the measurement system equation, (6.2). The term H^{inc} represents physical ultrasound wave propagation and L accounts for signal reflections within the UST chamber. For the purposes of the UST system under consideration, the multipath term, L , may be set to zero because its effects have been greatly reduced by introducing an acoustically absorptive material on the inner chamber wall and by windowing the time-domain signal (described in section 6.6.3). Assuming negligible multipath implies that H_{mod}^{inc} need not model reflections from the UST chamber wall. The idealized model then reduces to characterizing acoustic fields in a homogeneous and unbounded medium.

The value of Y_{mod}^{inc} used for incident field calibration is determined by taking the product of H_{mod}^{inc} and the source term, X_0 . The value of Y_{mod}^{inc} is thus the expected amplitude and phase of a pressure wave at an observation point, $\vec{r} = (x, y, z)$, which originated from a point source at $\vec{r}_0 = (x_0, y_0, z_0)$, such that the medium is homogeneous and unbounded.

Two incident field models have been utilised in this work. The first, commonly known as the 3D point-source, is given as

$$p_{3D}^{inc}(\vec{r}) = A \frac{e^{-jk_b|\vec{r}-\vec{r}_0|}}{|\vec{r}-\vec{r}_0|} \quad (6.24)$$

where A is the signal amplitude implicitly defined by X_0 , k_b is the homogeneous background wavenumber, $|\cdot|$ is the Euclidean norm and $j^2 = -1$. The second, known

as the line source or 2D point-source, is given as

$$p_{2D}^{inc}(\vec{r}) = \frac{A}{j4} \mathcal{H}_0^{(2)}(k_b |\vec{r} - \vec{r}_0|) \quad (6.25)$$

where $\mathcal{H}_0^{(2)}$ is the zeroth-order Hankel function of the second kind. Note that both source definitions are such that the pressure wave has zero phase at its point of origin.

In order to make use of the above models with the incident field calibration, we note that $|\vec{r} - \vec{r}_0|$ represents the distance between the transmitting transducer and a receiving transducer in the UST chamber. This means (6.24) and (6.25) can be reparameterized as

$$p_{3D}^{inc}(d) = A \frac{e^{-jk_b d}}{d} \quad (6.26)$$

$$p_{2D}^{inc}(d) = \frac{A}{j4} \mathcal{H}_0^{(2)}(k_b d) \quad (6.27)$$

where $d = |\vec{r} - \vec{r}_0|$. When calibrating data for a particular transducer pair, Y_{mod}^{inc} is set to the result of $p_{3D}^{inc}(d)$ or $p_{2D}^{inc}(d)$, where d is distance between the transducers. Determination of pairwise transducer distance is described in section 6.6.1.

For systems where multipath effects cannot be ignored, the model is likely not expressible in a closed-form as shown in (6.24) and (6.25). For such situations, a computational approach involving appropriate boundary conditions to model the chamber wall is recommended. Such a simulation will undoubtedly require knowledge of relative transducer locations in space. These can be determined using methods discussed in section 6.6.2.

6.5.2 Calibration Object Model

The scattered field calibration scheme requires a model, \mathbb{Y}_{mod}^{scat} , to characterize the scattering of ultrasound from a calibration object in an unbounded medium. It is defined as the product of the source term, X_0 , and the scattered field model, \mathbb{H}_{mod}^{scat} . The value of \mathbb{Y}_{mod}^{scat} is thus the expected amplitude and phase of scattered pressure waves at an observation point, $\vec{r} = (x, y, z)$, for an incident field originating at $\vec{r}_0 = (x_0, y_0, z_0)$. The implicit incident field models utilized here are p_{3D}^{inc} and p_{2D}^{inc} , defined in section 6.5.1.

A calibration object whose acoustical properties are well known and easy to model should be employed. For this reason, a thin-walled straw containing only air is used. Such a calibration object may be modelled as a soft cylindrical scatterer because air is considered a soft object relative to water (the background medium). The motivation for this approach is due, in part, to the success in calibrating MWT systems at the UMEIL with a perfect electric conductor (PEC). The PEC is the electromagnetic analogue of the soft scatterer in the sense that they are modelled with equivalent boundary conditions [27].

A closed-form solution of acoustical scattering from a soft cylinder can be determined analytically [31]. But, in an effort to allow for more general calibration objects and to maintain consistency with FEM-CSI, the field at \vec{r} is determined by simulation via the finite element method (FEM). The same scattered field model used internally by FEM-CSI is employed to simulate the insonification of the calibration object in an unbounded medium. When applying the scattered field calibration, \mathbb{Y}_{mod}^{scat} is set to the value of FEM-computed scattered pressure waves at an observation point representing the position of a particular receiving transducer. Transducer locations used in the FEM simulation are determined with methods described in section 6.6.2.

6.6 Time-Domain Signal Processing

This section covers the use of time-domain techniques to determine the signal time-of-flight (TOF) between pairs of transducers and, in turn, their relative coordinates in space. Details about data windowing as a means of reducing signal distortion before applying the FFT are also given. Together, calibrated frequency-domain data and transducer locations form the necessary input to FEM-CSI.

The signal processing methods described in this section are all written in MATLAB [24] and make use of its many built-in functions.

6.6.1 Time-of-Flight Determination

The time-of-flight, t_{ab} , between a pair of transducers, τ_a and τ_b , is defined as the time taken for an ultrasound signal to reach τ_b when sent from τ_a . TOF information is determined from incident field measurements by using a simple threshold detection algorithm (see Algorithm 6.1). This algorithm operates under the following assumptions:

1. Transmission and sampling of the signal are triggered to begin at the same time.
2. Recorded data will be near the measured noise floor until the signal transmitted by τ_a arrives at τ_b .

In other words, TOF is calculated from the sample index at which the signal first arrives at τ_b and a recorded signal, s , defined by a sequence of I samples, $[s_1, \dots, s_I]$, is assumed to contain a subsequence, $s' = [s_1, \dots, s_i]$, that is composed of consecutive elements of s , such that the magnitude of each element of s' is less than a threshold value ϑ . Based on these assumptions, the algorithm first finds a subsequence, s' , in

a recorded signal, for a given threshold. It then finds in s' , the shortest subsequence $[s_l, \dots, s_i]$ for which the product $s_{l-1} \cdot s_l < 0$. Element s_l is known as the signal-arrival sample and its index is returned by the algorithm. The TOF between τ_a and τ_b is therefore

$$t_{ab} = \frac{l-1}{f_s} \quad (6.28)$$

where t_{ab} is measured in seconds and f_s is the sampling frequency.

Algorithm 6.1 Signal-Arrival Sample Determination

Input: A sampled signal $s = [s_1, \dots, s_I]$ and threshold value ϑ

Output: Signal-arrival sample index l

```

1:  $i = 1$ 
2: while  $|s_i| < \vartheta$  do
3:    $i = i + 1$ 
4: end while
5:  $l = i$ 
6: while  $s_{l-1} \cdot s_l > 0$  do
7:    $l = l - 1$ 
8: end while
9: return  $l$ 

```

There is some difficulty in reliably determining the signal-arrival sample when Algorithm 6.1 is applied to raw signal data. This difficulty is due to high-frequency noise and DC bias superimposed onto the signal by the measurement system. The high-frequency noise appears in the data as a small ripple, as can be seen in Figure 6.3(a), whereas the presence of DC bias is characterized by non-zero average random-noise. In order to improve the accuracy of Algorithm 6.1, the input signal, s , is a “cleaned” version of noisy measured data. For the purposes of TOF determination, cleaned signal data is defined as measured signal data with DC bias and high-frequency noise components removed. These types of noise are eliminated by taking the noisy data to the frequency domain via FFT and setting the troublesome frequency components

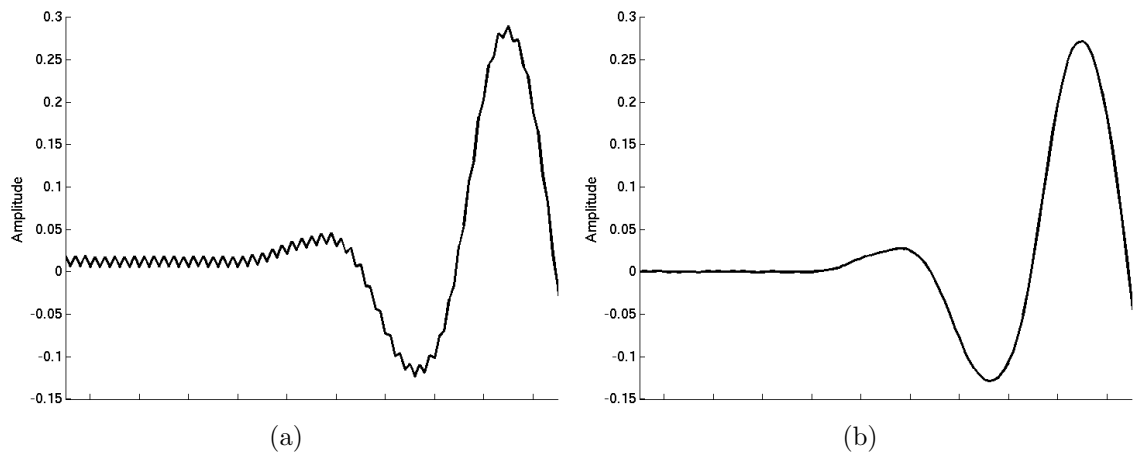


Figure 6.3: Comparison of raw and cleaned signal data. (a) Sample of raw measurement data. (b) Same data after applying Algorithm 6.2. It can be seen that high-frequency ripple effects and DC bias are removed.

to zero. In order to remove DC bias, all frequencies below 140 kHz are set to zero. High-frequency noise is observed at one half the sampling rate and so frequencies greater than 24 MHz are set to zero in order to eliminate the ripple effect. Clean data is then obtained by taking the modified frequency-domain signal back to the time domain by applying the inverse FFT (IFFT). The data cleaning procedure is outlined in Algorithm 6.2 where the FFT and IFFT algorithms used are built-in MATLAB functions. A comparison of measured and cleaned signal data is depicted in Figure 6.3.

Algorithm 6.2 Cleaning Noisy Signal Data

Input: Noisy measured signal data \tilde{s}

Output: Cleaned signal data s

- 1: $\tilde{S} = \text{FFT}(\tilde{s})$
 - 2: $S = \tilde{S}$ with troublesome high and low frequency components set to zero
 - 3: $s = \text{IFFT}(S)$
 - 4: **return** s
-

The application of Algorithm 6.1 to cleaned signal data is effective in finding the signal-arrival sample for most pairs of transducers. However, the presence of inherent random noise in such data may cause the threshold detection algorithm to determine inconsistent signal-arrival samples. This causes the non-physical result $t_{ab} \neq t_{ba}$ for certain pairs of transducers and creates ambiguity in signal TOF. Furthermore, threshold detection cannot be used to determine TOF values for pairs of nearby transducers. This is because crosstalk between channels in the TR-module (see Chapter 2) causes high-amplitude noise in measured signal data and overlaps with an early received signal. In order to resolve these ambiguities and to interpolate missing data, a correction procedure is applied to available TOF information. This procedure is based on methods described in [20] and is outlined in Algorithm 6.3.

In order to correct and interpolate TOF data, a matrix, T , known as the TOF matrix, is introduced. This matrix is defined such that $(T)_{a,b} = t_{ab}$ and any unknown TOFs are set to zero. Under ideal circumstances, the TOF matrix possesses a particular structure that is due to the nature of the transducer locations. More specifically, consider a matrix, Q , obtained by squaring every element of T . Such a matrix has the following properties [20]:

1. It is symmetric.
2. Its diagonal elements are zero.
3. Its elements are non-negative.
4. It is of rank at most 4.

Note that the last property is dependent on the dimensionality of the problem. For transducers located in 3D space, the rank of Q is at most 5 [21].

Algorithm 6.3 Time-of-Flight Matrix Correction*Input:* Measured TOF matrix \tilde{T} *Output:* Corrected TOF matrix T

- 1: $\tilde{Q}^{(i+1)} = \psi_1(\tilde{Q})$ where \tilde{Q} is obtained by squaring every element of \tilde{T}
- 2: **repeat**
- 3: $\tilde{Q}^{(i)} = \tilde{Q}^{(i+1)}$
- 4: $\tilde{Q}^{(i+1)} = \psi_2(\tilde{Q}^{(i+1)})$
- 5: $\tilde{Q}^{(i+1)} = \psi_3(\tilde{Q}^{(i+1)})$
- 6: $\tilde{Q}^{(i+1)} = \psi_4(\tilde{Q}^{(i+1)})$
- 7: **until** $\|\tilde{Q}^{(i+1)} - \tilde{Q}^{(i)}\|_F < \text{error tolerance}$
- 8: Obtain T by taking the square root of every element of $\tilde{Q}^{(i+1)}$
- 9: **return** T

A TOF matrix constructed using measurement data, \tilde{T} , will generally not have an associated matrix \tilde{Q} satisfying the above properties. A correction algorithm is therefore applied to \tilde{T} to reduce arrival-sample inconsistencies and interpolate missing data. The principle behind the correction algorithm is to enforce the above properties by means of matrix transformations which are defined below for a square matrix A :

1. $\psi_1(A) = \frac{A+A^T}{2}$, to enforce symmetry.
2. $(\psi_2(A))_{a,b} = \begin{cases} (A)_{a,b} & \text{if } a \neq b \\ 0 & \text{otherwise} \end{cases}$, to set diagonal entries to zero.
3. $(\psi_3(A))_{a,b} = \begin{cases} (A)_{a,b} & \text{if } (A)_{a,b} \geq 0 \\ 0 & \text{otherwise} \end{cases}$, to enforce non-negativity of all entries.
4. $\psi_4(A) = U_4 \Sigma_4 V_4^T$, the best rank 4 approximation of A via singular value decomposition (SVD) [55].

These transformations are successively applied to \tilde{Q} in an iterative process as outlined in Algorithm 6.3. The correction procedure has converged to a solution when the Frobenius norm of the difference between successive iterations is less than a specified

error tolerance. A proof of the convergence of this algorithm is given in [20]. The corrected TOF matrix is then used to determine relative transducer locations. This procedure is described in the next section.

6.6.2 Transducer Localization

Transducer location determination is an important aspect of the calibration process. Spatial transducer coordinates are required by the imaging algorithm and are also used in the modelling of the incident field and the calibration object. A localization algorithm is utilized because it would be less practical to obtain the required sub-millimetre accuracy with physical measuring equipment.

Transducer localization is achieved by using an implementation of classical multidimensional scaling (MDS) [23, 56] and a transducer distance matrix, D . MDS is a numerical procedure used to determine the relative spatial coordinates of a set of nodes given their pairwise Euclidean distance. For the purposes of transducer localization, if the transducers are perceived as such nodes in space, it then follows that the distance matrix should be defined as

$$D = c_b T \tag{6.29}$$

where c_b is the speed of sound in the background medium and T is a corrected TOF matrix obtained from incident field measurements as described in section 6.6.1. The value of c_b is determined from a water temperature measurement and the following formula, taken from [57]:

$$c_b = 1405.610 + 4.59754 \mathbb{T} - 0.0381796 \mathbb{T}^2. \tag{6.30}$$

Formula (6.30) is valid for a water temperature, \mathbb{T} , in the range of 15°C to 35°C.

The MDS implementation utilised in this work is outlined in Algorithm 6.4 and is based on localization techniques presented in [20]. It returns the transducer location estimates, Λ , as a list of 2D Cartesian coordinates. It is important to note that the estimated coordinates are relative and are therefore invariant up to translation, rotation and reflection of the spatial transducer locations. The absolute locations are therefore determined using the position of a reference transducer and the geometric center of the returned coordinates.

Algorithm 6.4 MDS Localization

Input: Distance matrix D and number of transducers α

Output: Location estimates Λ

- 1: Obtain Q by squaring every element of D
 - 2: $L = I - \frac{1}{\alpha}J_\alpha$ where I is the identity matrix and J_α is a $\alpha \times \alpha$ matrix of ones
 - 3: $Q' = -\frac{1}{2}LQL$
 - 4: Compute $U_2\Sigma_2^2U_2^T$, the best rank 2 approximation of Q' via SVD
 - 5: $\Lambda = U_2\Sigma_2$
 - 6: **return** Λ
-

6.6.3 Signal Data Windowing

Data windowing is used to reduce signal distortions present in time-domain data. Distortions corrupt recorded signals and can lead to significant errors in frequency-domain data when their FFT is determined. The purpose of windowing is to minimize the amplitude of these flaws while preserving meaningful signal information.

Several sources of distortion have been identified. One of them is the inconsistency between the measured incident and total fields. This type of distortion affects the resulting scattered field because the incident field does not subtract exactly from the total field. It appears as an early sinusoidal distortion and is superimposed onto the

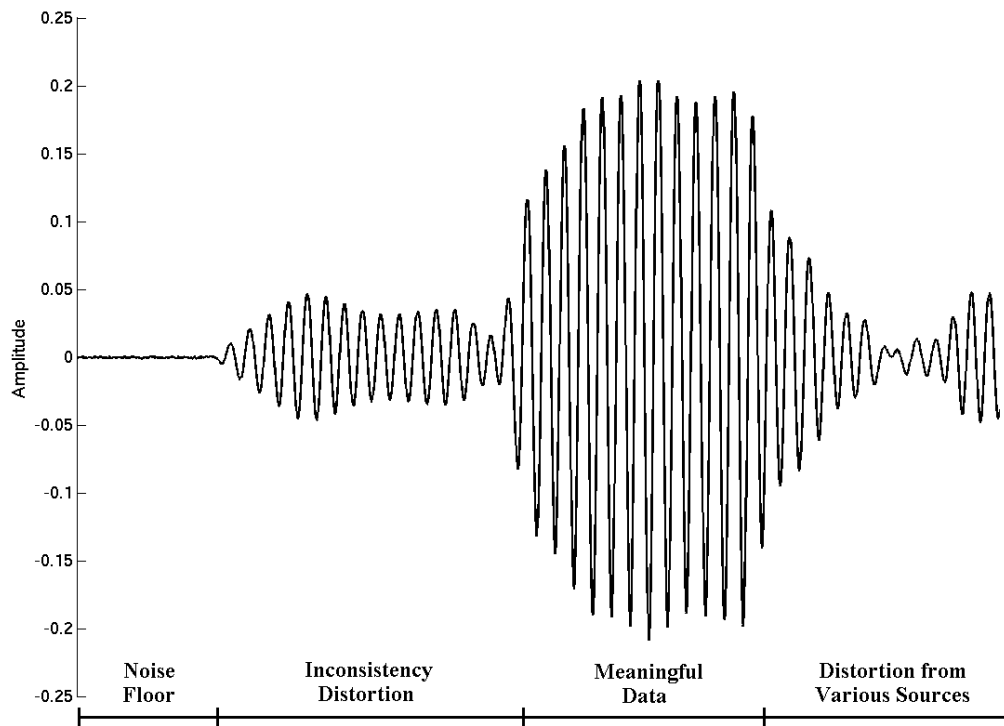
remaining time-domain data. An example of this effect is shown in Figure 6.4(a). It has been observed that this distortion manifests near the frequency of interest and can be a significant source of noise for low-contrast objects. Another source of distortion occurring early in measured data is caused by crosstalk in the TR-module. It is characterized by a high-amplitude signal appearing at the start of recorded data and has duration equal to the specified pattern length. An example of this effect is illustrated in Figure 6.4(b).

Other sources of distortion are caused by transducer ringing [58] and reflections from fixed objects in the chamber. An example of this effect on incident time-domain data is shown in Figure 6.4(b). Ringing is the result of mechanical vibrations of the transmitting transducer which persist after the electrical signal pulse has stopped. These vibrations are recorded by the receiving transducer which also incorporates its own ringing effects after receiving the main pressure signal.

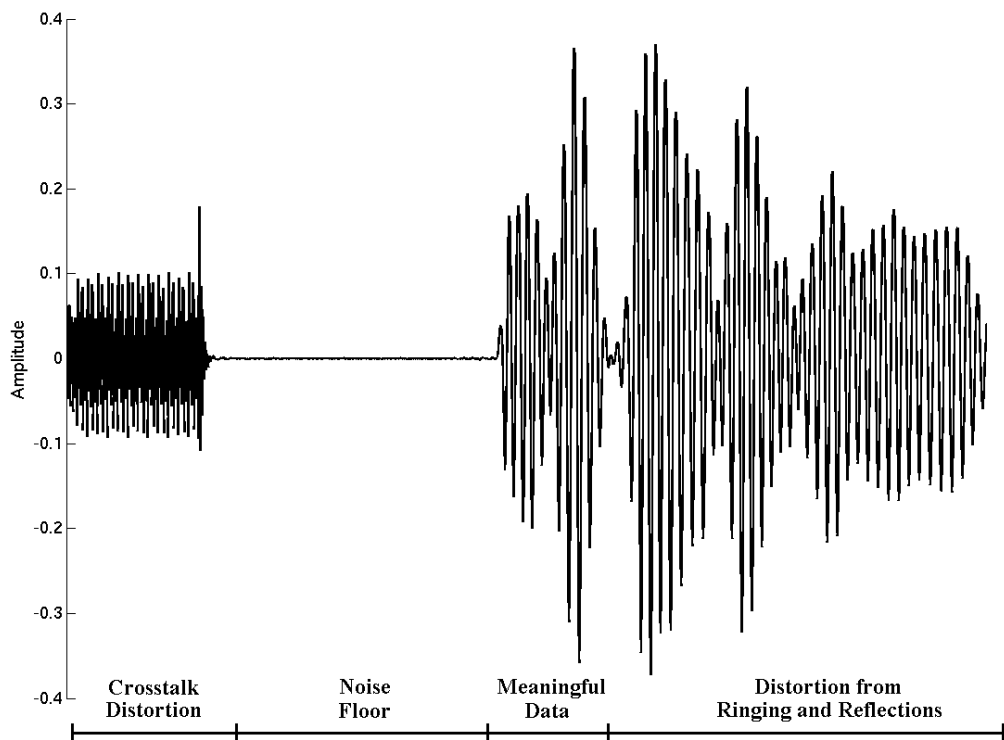
In a model UST system, a measured time-domain signal, $s^{ideal} = [s_1^{ideal}, \dots, s_I^{ideal}]$, has a particular structure. It is zero everywhere except for a subsequence $\dot{s}^{ideal} = [s_{m'}^{ideal}, \dots, s_{n'}^{ideal}]$, where $1 < m' < n' < I$. The data contained in \dot{s}^{ideal} is the received finite duration signal that originated at the transmitter. The form of s^{ideal} is due to the time delay between transmission and reception of the waveform. With a practical system, the measured time-domain signal, $s = [s_1, \dots, s_I]$, can be regarded as an idealized signal superimposed with a distortion, $s^d = [s_1^d, \dots, s_I^d]$. This relation can be written as

$$s = s^{ideal} + s^d. \quad (6.31)$$

In order to extract s^{ideal} from measured data, all values of s^d must be known. Unfortunately, not all the sources of distortion previously mentioned can be accurately characterized. This implies that idealized data cannot be exactly recovered from s .



(a)



(b)

Figure 6.4: Illustration of time-domain data distortion. (a) Scattered field data with inconsistency distortion. (b) Incident field data distorted by crosstalk, ringing and reflections

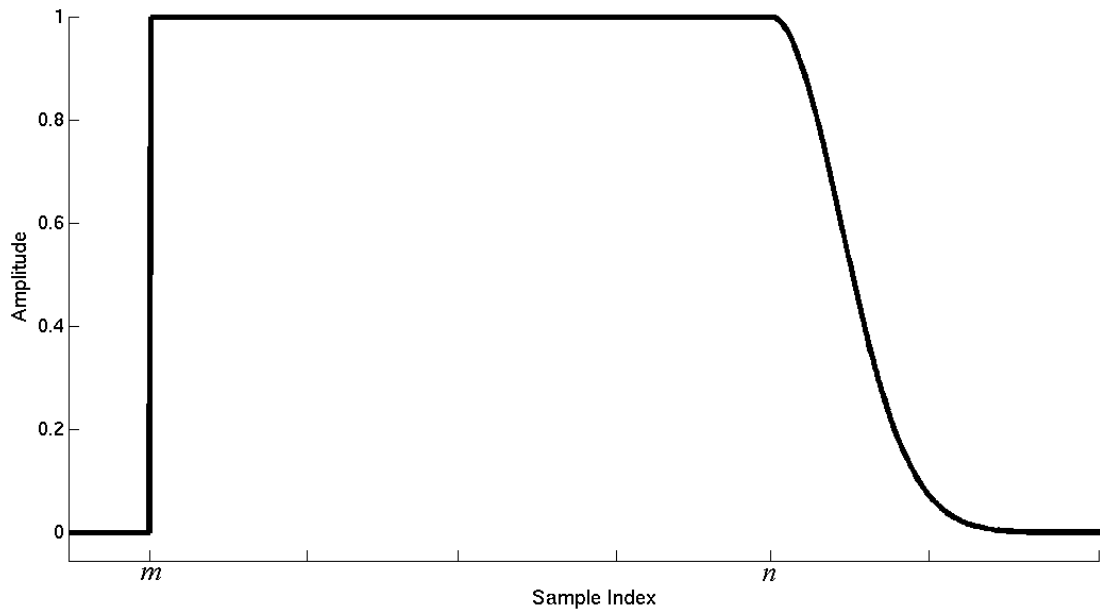


Figure 6.5: Example window plot. When such a window is applied to signal data, distortions before sample index m are removed and those after sample index n are quickly dampened.

It is still possible to improve measured signal data despite s^d being unknown. The structure of s can be brought closer to that of s^{ideal} by zeroing its data, except for a subsequence $\dot{s} = [s_m, \dots, s_n]$, where $1 < m \leq m' < n' \leq n < I$. This type of adjustment is achieved by applying a window function [59] to s . The function employed is a modified rectangular window whose shape allows it to serve two purposes. It removes any inconsistency and crosstalk distortion before s_m by setting these samples to zero. It also quickly dampens any ringing and unwanted reflections after s_n , causing the data to appear closer to the expected ideal. An example window is plotted in Figure 6.5. It should be noted that windowing does not remove distortion superimposed onto \dot{s} . Noise in this portion of the measured signal remains throughout the calibration process.

In order to describe the windowing process, suppose that the recorded signal, s , is measured at receiver τ_b due to a source transducer τ_a . A window is applied to s by

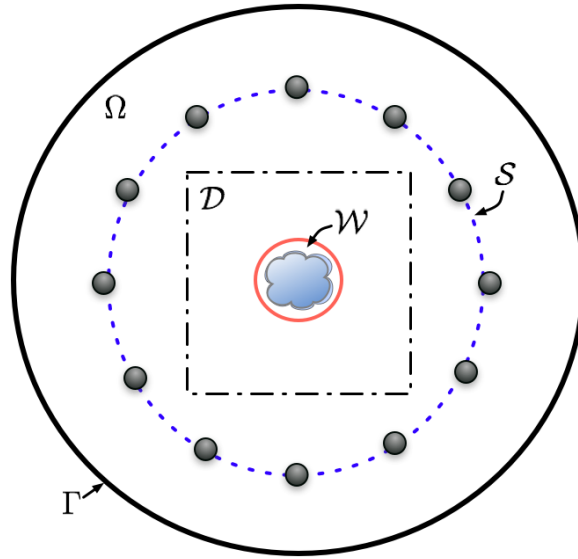


Figure 6.6: Geometrical model of the windowing domain. The windowing domain, \mathcal{W} , is a subdomain of \mathcal{D} and entirely contains the object of interest.

taking its element-wise product with a discrete windowing function:

$$\mathring{s}_i = s_i \varphi_{ab}(i) \quad (6.32)$$

where \mathring{s} is the resulting windowed signal and

$$\varphi_{ab}(i) = \begin{cases} 0 & i < m_{ab} \\ 1 & m_{ab} \leq i < n_{ab} \\ \exp\left(\frac{-(i-n_{ab})^2}{\sigma}\right) & i \geq n_{ab} \end{cases} \quad (6.33)$$

for a user-defined constant, σ , setting the rate at which the tail of the window function approaches zero ($\sigma = 3600$ for $f_s = 50$ MHz). The window parameters m_{ab} and n_{ab} are dependent on the size and location of a user-defined windowing domain, \mathcal{W} , relative to τ_a and τ_b . The windowing domain is a circular subdomain of \mathcal{D} as depicted in Figure 6.6.

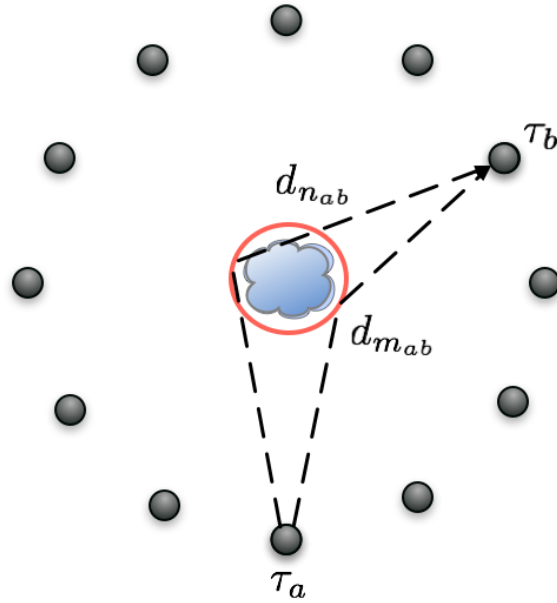


Figure 6.7: Example of ray paths used for window bound determination. These paths are used when defining the particular window function, φ_{ab} , for a signal transmitted from τ_a and measured by τ_b . The path lengths, $d_{m_{ab}}$ and $d_{n_{ab}}$, specify the window parameters, m_{ab} and n_{ab} , respectively.

When applying φ_{ab} to scattered field data, the value of m_{ab} is determined from the shortest distance, $d_{m_{ab}}$, a signal ray must travel from τ_a to τ_b after one reflection from the surface of \mathcal{W} . A depiction of such a ray path is provided in Figure 6.7. The number of samples before the scattered signal is expected to reach the receiver is therefore

$$m_{ab} = \left\lfloor \frac{d_{m_{ab}} f_s}{c_b} \right\rfloor \quad (6.34)$$

where “ $\lfloor \cdot \rfloor$ ” denotes the floor function.

The value of n_{ab} is determined from the length of the longest ray path, $d_{n_{ab}}$, passing through \mathcal{W} , from τ_a to τ_b (also shown in Figure 6.7). The value of this parameter must also take into account the duration (pattern length) of the transmitted waveform, ϖ . The number of samples after which the measured scattered field is expected to be

zero is therefore

$$n_{ab} = \left\lceil \frac{d_{n_{ab}} f_s}{c_b} + \varpi f_s \right\rceil \quad (6.35)$$

where “ $\lceil \cdot \rceil$ ” denotes the ceiling function.

When applying the window function to incident field data, the value of m_{ab} is set to $\lceil \varpi f_s \rceil$ where ϖ is the pattern length measured in seconds and f_s is the sampling frequency. This value of m_{ab} is used to remove crosstalk early in the incident field signal data. The same value of n_{ab} is used for windowing incident and scattered signal data.

Certain constraints on the windowing domain must be considered before defining its location and size. In order to avoid corrupting meaningful data in the idealized range between m' and n' , \mathcal{W} must entirely contain the area occupied by the imaging target. In response to this constraint, it may be tempting to set \mathcal{W} to the size of \mathcal{D} . This would ensure adequate bounds on m' and n' but such a large windowing domain is not very effective in removing distortion. The optimal windowing domain is just large enough to closely encircle the object of interest. Figure 6.8 shows an example scattered signal that has been windowed for different sized \mathcal{W} . The plots are a depiction of a reflected signal from a high-contrast scatterer with a radius of 3 mm. This example is chosen because the index of m' can be easily identified ($m' \approx 4100$). In Figure 6.8(b) it can be seen that meaningful data is preserved with a relatively large window (20 mm radius) but much of the distortion remains. When compared to Figure 6.8(c), it is observed that a close-fitting \mathcal{W} (5 mm radius) better isolates meaningful data from nearby distortion.

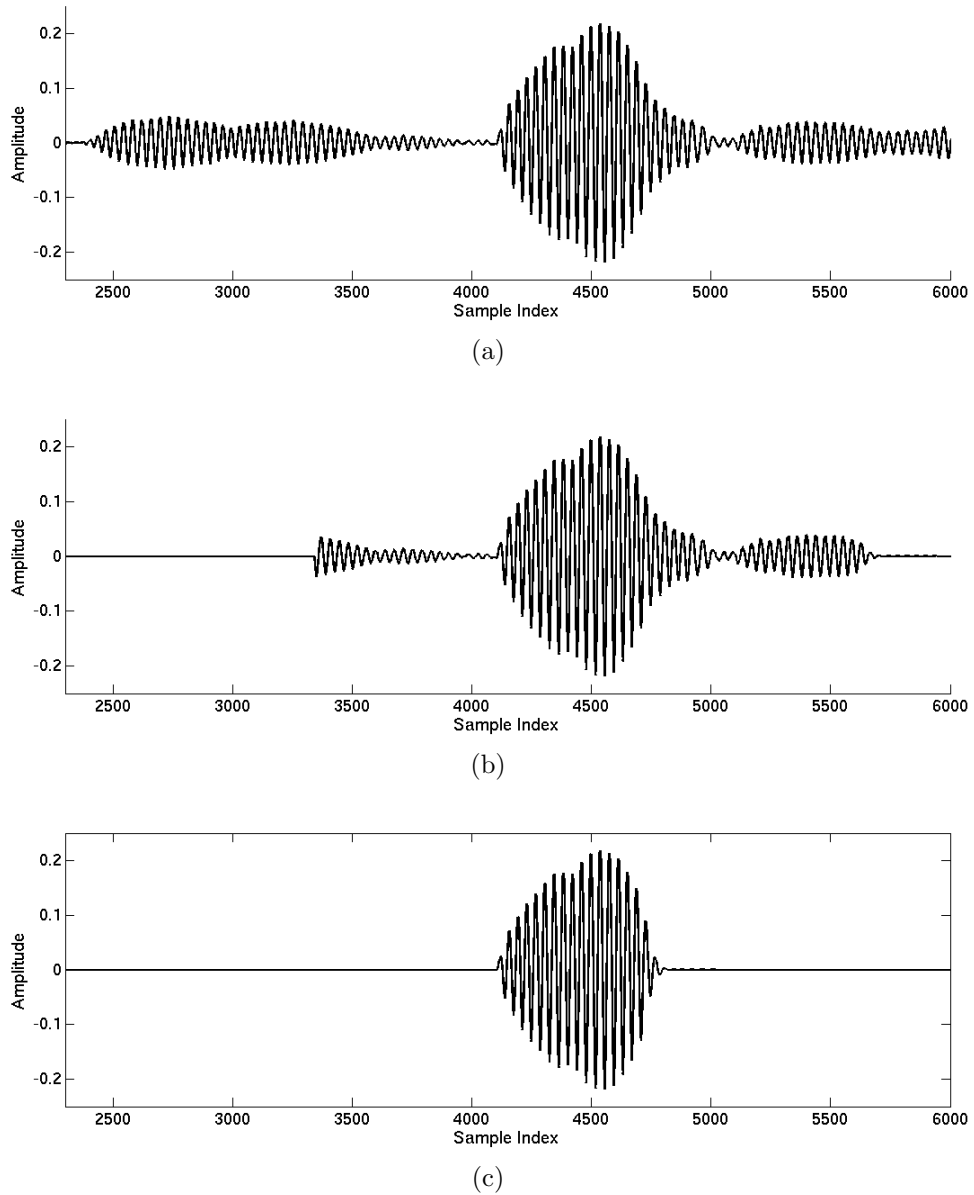


Figure 6.8: Illustration of windowing applied to scattered field data for different window radii. The target is a high-contrast object with a radius of 3 mm. Windowing is employed to remove distortion and isolate meaningful data. (a) Scattered field signal data before windowing. (b) Same data after applying a 20 mm radius window. (c) The data after applying a 5 mm radius window.

6.7 Known Calibration Issues

An implicit assumption about transducer system functions is made for the calibration principles explained in sections 6.3 and 6.4. It is presupposed that both incident and scattered signals are subject to the same transducer system function for a particular transmitter-receiver pair. In practice, this is not necessarily the case. This assumption is not valid when the system function of the transducers vary with respect to the signal's angle of departure and incidence. Figure 6.9 illustrates how signals travelling directly from the source to certain receivers do not depart and arrive at the same angles as those scattered by the object of interest. It can also be inferred from the diagram that incident and scattered signals are only subject to the same system function for transducer pairs that are positioned diametrically across the transducer ring from each other.

The consequences of this effect are most apparent for the incident field calibration. If this calibration principle were applied to a transducer pair that does not adhere to the above assumption then the system equation for the measured incident field in an unbounded medium would be written as

$$Y^{inc} = X G^{inc} H^{inc} K^{inc} \quad (6.36)$$

where G^{inc} and K^{inc} have the superscript, *inc*, to differentiate them from the system functions of the scattered signal: G^{scat} and K^{scat} . The measured scattered and total fields would therefore be given as

$$Y^{scat} = X G^{scat} H^{scat} K^{scat} \quad (6.37)$$

$$Y^{tot} = X (G^{inc} H^{inc} K^{inc} + G^{scat} H^{scat} K^{scat}). \quad (6.38)$$

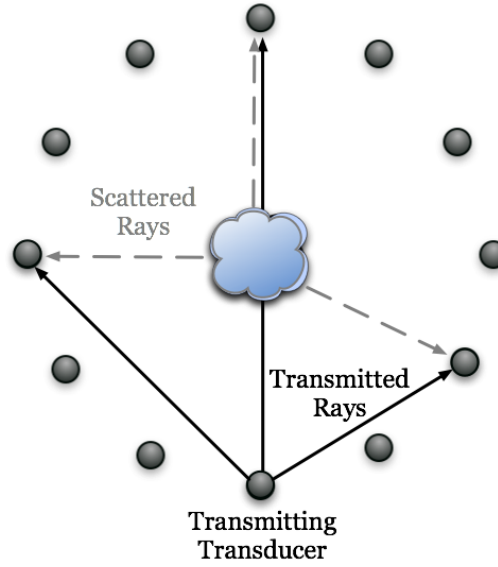


Figure 6.9: Illustration of incident and scattered ray arrival angles. Signal rays travelling directly from the source to certain receivers depart and arrive at different angles as compared to those scattered by the target. It can be seen that incident and scattered signals only arrive at the same angle for transducer pairs that are positioned diametrically across the transducer ring from each other.

The calibration coefficient would be determined from the incident field in a manner similar to what is described in section 6.3.2 and would be written as

$$C = \frac{Y_{mod}^{inc}}{Y^{inc}} = \frac{X_0 H_{mod}^{inc}}{X G^{inc} H^{inc} K^{inc}}. \quad (6.39)$$

When applied to the scattered field, the supposedly calibrated data results in

$$\begin{aligned} Y^{cal} &= CY^{scat} \\ &= \frac{X_0 H_{mod}^{inc}}{X G^{inc} H^{inc} K^{inc}} X G^{scat} H^{scat} K^{scat} \\ &= \frac{G^{scat} K^{scat}}{G^{inc} K^{inc}} \frac{H_{mod}^{inc}}{H^{inc}} X_0 H^{scat}. \end{aligned} \quad (6.40)$$

This indicates that the incident field calibration procedure does not adequately re-

move system effects from measured data when $G^{inc} K^{inc} \neq G^{scat} K^{scat}$, which can be the case when the transducer pair is not positioned diametrically.

The issue of inconsistent transducer system functions can theoretically be avoided with the scattered field calibration when the OI and calibration object have similar dimensions and position relative to the transducers. This is because the calibration coefficients are determined from scattered fields created by the calibration object, thereby eliminating the need to consider system functions with respect to the incident field. Calibration error due to inconsistent transducer system functions is thus reduced in data prepared with the scattered field calibration and better image reconstruction can be expected.

The practical difficulty in applying the scattered field calibration is in finding a good estimate for the calibration object's location with respect to the determined transducer positions. In order to keep modelling error to a minimum, the calibration object's location must ideally be estimated to sub-wavelength accuracy. At 1.5MHz the ultrasound signal wavelength is approximately 1mm, meaning that its location would ideally have to be estimated to a fraction of a millimetre. Such accuracy clearly cannot be obtained without sophisticated measuring implements. To obtain a viable location estimate, we turn to images of the calibration object produced from measured data calibrated with the incident field principle. With such images it is possible to determine a reasonable estimate of the calibration object location relative to the computed transducer positions. Note that such an estimate is only considered "reasonable" because an improvement is observed in image reconstruction when compared to uncalibrated data. The accuracy of determining the calibration object location in this manner is still questionable. Images reconstructed from data calibrated using this approach are shown in Chapter 7.

6.8 Summary of Calibration Steps

The principles and methods presented in this chapter are all aspects of the calibration process. These aspects are organized into two different algorithms known as the incident field calibration and the scattered field calibration. These calibration processes are summarized in this section. Inputs to the incident field calibration procedure (Algorithm 6.5) are the measured incident and total fields for all transmitter-receiver pairs, \tilde{s}^{inc} and \tilde{s}^{tot} , respectively. Inputs to the scattered field calibration procedure (Algorithm 6.6) are \tilde{s}^{inc} , \tilde{s}^{tot} and the measured total field for the calibration object, \tilde{s}_{co}^{tot} . All operations are understood to be applied to the data for transducer pairs of interest. Both algorithms assume that the background-medium sound speed, c_b , has been established by a water temperature measurement and formula (6.30). It is also assumed that the sampling frequency, f_s , and the measurement frequency of interest are given as input to the algorithms.

Algorithm 6.5 Incident Field Calibration

Input: Incident field data \tilde{s}^{inc} , Total field data \tilde{s}^{tot}

Output: Calibrated scattered field Y^{cal}

Transducer localization

- 1: Clean incident data and store in s^{inc} (Algorithm 6.2)
- 2: Determine \tilde{T} from s^{inc} (Algorithm 6.1)
- 3: Obtain T from \tilde{T} (Algorithm 6.3)
- 4: Determine Λ from T (Algorithm 6.4)

Convert to frequency domain

- 5: Obtain scattered data $\tilde{s}^{scat} = \tilde{s}^{tot} - \tilde{s}^{inc}$
- 6: Window incident data $\mathring{s}^{inc} \leftarrow \tilde{s}^{inc}$
- 7: Window scattered data $\mathring{s}^{scat} \leftarrow \tilde{s}^{scat}$
- 8: Determine frequency-domain incident data $Y^{inc} = \text{FFT}(\mathring{s}^{inc})$
- 9: Determine frequency-domain scattered data $Y^{scat} = \text{FFT}(\mathring{s}^{scat})$

Apply calibration

- 10: Compute model incident data, Y_{mod}^{inc} , from Λ
 - 11: Determine calibration coefficients $C = Y_{mod}^{inc}/Y^{inc}$
 - 12: Apply calibration coefficients $Y^{cal} = CY^{scat}$
 - 13: **return** Y^{cal}
-

Algorithm 6.6 Scattered Field Calibration

Input: Incident field data \tilde{s}^{inc} , Total field data \tilde{s}^{tot} , Calibration object data \tilde{s}_{co}^{tot}

Output: Calibrated scattered field Y^{cal}

Transducer localization

- 1: Clean incident data and store in s^{inc} (Algorithm 6.2)
- 2: Determine \tilde{T} from s^{inc} (Algorithm 6.1)
- 3: Obtain T from \tilde{T} (Algorithm 6.3)
- 4: Determine Λ from T (Algorithm 6.4)

Convert to frequency domain

- 5: Obtain scattered data $\tilde{s}^{scat} = \tilde{s}^{tot} - \tilde{s}^{inc}$
- 6: Obtain calibration object scattered data $\tilde{s}_{co}^{scat} = \tilde{s}_{co}^{tot} - \tilde{s}^{inc}$
- 7: Window scattered data $\hat{s}^{scat} \leftarrow \tilde{s}^{scat}$
- 8: Window calibration object scattered data $\hat{s}_{co}^{scat} \leftarrow \tilde{s}_{co}^{scat}$
- 9: Compute frequency-domain scattered data $Y^{scat} = \text{FFT}(\hat{s}^{scat})$
- 10: Compute frequency-domain calibration-object data $\mathbb{Y}^{scat} = \text{FFT}(\hat{s}_{co}^{scat})$

Apply calibration

- 11: Determine model calibration object data, \mathbb{Y}_{mod}^{scat}
 - 12: Compute calibration coefficients $C = \mathbb{Y}_{mod}^{scat} / \mathbb{Y}^{scat}$
 - 13: Apply calibration coefficients $Y^{cal} = CY^{scat}$
 - 14: **return** Y^{cal}
-

7

Results

The outcome of applying the principles and methods given in Chapter 6 are presented here. A discussion on the effectiveness of the described transducer localization method is first presented. It is then followed by an analysis of inversion results obtained after applying the incident and scattered field calibration techniques to collected data.

7.1 Transducer Localization

The effectiveness of the transducer localization technique presented in section 6.6.2 is demonstrated by applying it to model TOF data. A simulation approach is employed because the true locations of the UST chamber transducers are not known, making it difficult to directly show that the localization method works. The intention here is to construct models that adequately represent possible transducer configurations found in the UST chamber and to apply the localization algorithm on TOF information derived from them. The effectiveness of the technique is measured by evaluating the Euclidean distance between the computed transducer locations and the ones expected by the model. The distance between computed and expected locations will be referred to as the transducer positioning error. Based on experience with

MWT systems, transducer positioning error should be kept below one half of the signal wavelength observed in the background medium. In the case of the UST system, the shortest wavelength encountered is approximately 1mm. Therefore, positioning error must be kept below 0.5 mm.

Transducer-ring models are created through the use of randomized parameters in order to evaluate the localization procedure on many possible configurations. Randomness is kept within realistic bounds to best represent the possible transducer arrangements found in the UST chamber. A particular model is constructed using the following three-step process:

1. A set of 32 evenly-spaced nodes are placed on a circle centered at the origin of a 2D Cartesian coordinate system. The chosen circle radius is 65 mm, which approximately models the transducer-ring radius found in the UST chamber.
2. The nodes are then shifted by up to 1.5mm in any direction, away from their ideal locations on the circle. The amount of shift for each individual node is determined by a MATLAB pseudo-random number generating function with uniform probability distribution. This is done to represent the assumption that the transducers of the UST chamber do not lie on a perfect circle.
3. The system transducers have non-negligible dimension due to their size with respect to wavelength. In order to account for this in the model, transducer halos are introduced. Halos are circles centered at nodes and have a diameter ranging from 1.7 mm to 2.7 mm. They represent the space occupied by transducers in 2D. The diameter of each individual halo is determined by a MATLAB pseudo-random number generating function with uniform probability distribution.

The construction described above implies that models will differ in transducer sizes

and locations. An example of a constructed model is depicted in Figure 7.1.

The transducer localization technique is then applied to TOF information extracted from the model. In order to simulate TOF measurements that would be taken by the UST system, the model is treated as follows:

1. The TOF matrix is created by first computing a distance matrix of the model transducers. The distance between a transducer pair is taken as the shortest straight-line (ray) between their halos (see Figure 7.2). The distances are determined in this manner to simulate the arrival of signals at different transducer surface regions as a consequence of source location. The TOF matrix is then determined by dividing each element of the distance matrix by the assumed signal speed of 1500m/s.
2. A sample matrix is obtained from the TOF matrix by multiplying each of its elements by an assumed sampling rate of 50 MHz. All values of the new sample matrix are rounded to the nearest integer. This conversion is performed to simulate the discretized nature of the measured signals.
3. In order to simulate inconsistency in measured signal-arrival samples, each element of the sample matrix is adjusted by an integer value taken from a MATLAB pseudo-random number generating function with a normal probability distribution. The distribution parameters are set to a mean of 0 and a standard deviation of 5. The distribution parameters commonly seen with experimental data have a mean of 0 and a standard deviation of approximately 3.5.
4. The TOF between nearby transducers is not known in the experimental case. To incorporate this lack of information into the simulation, the appropriate elements are set to zero in the sample matrix.

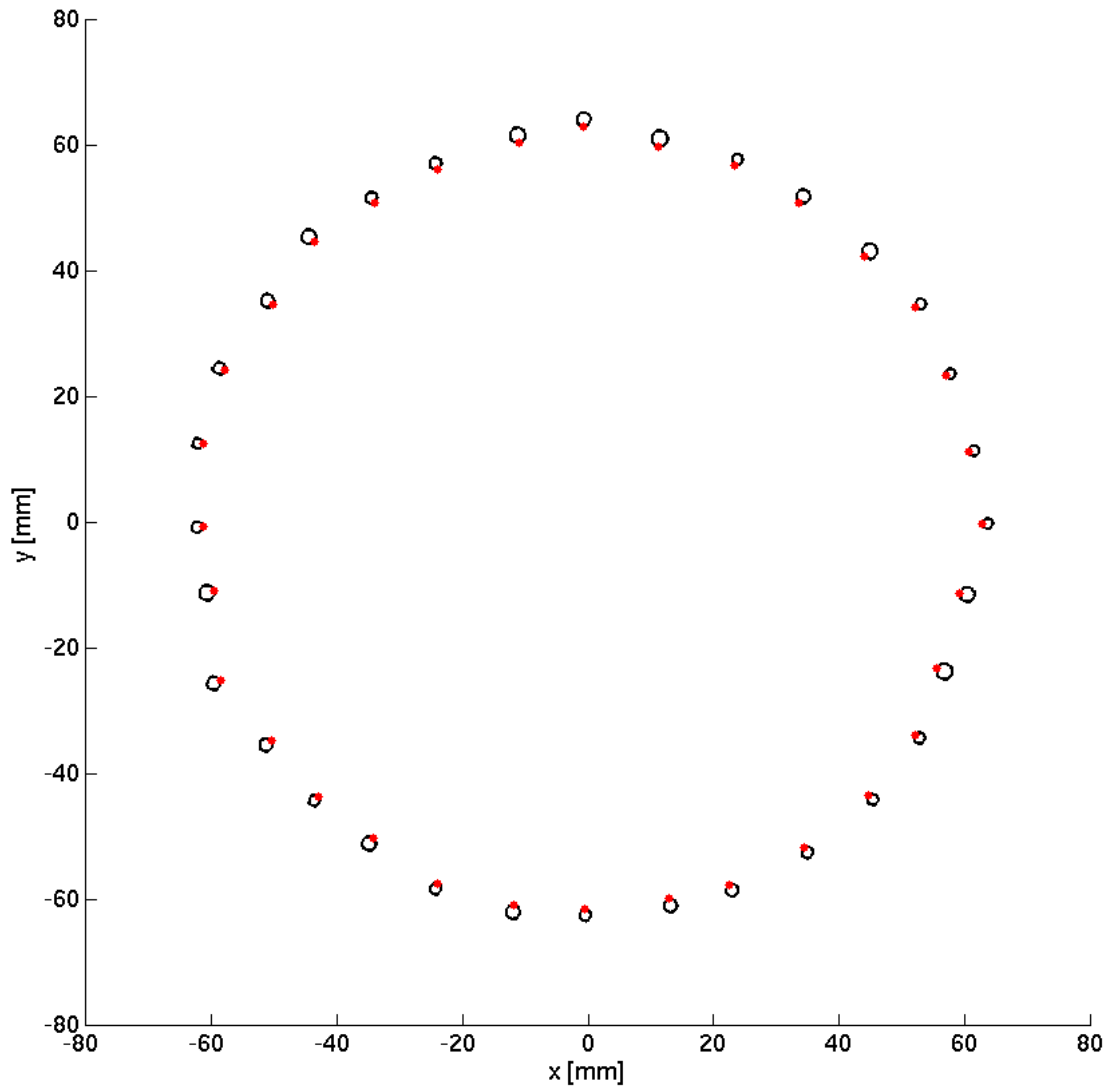


Figure 7.1: Example of a constructed transducer-ring model. The black circles represent locations and sizes of the model transducers. The points on these circles which are closest to the geometric center of the ring are coloured in red. The coordinates of these points are expected to be computed by the MDS localization algorithm.

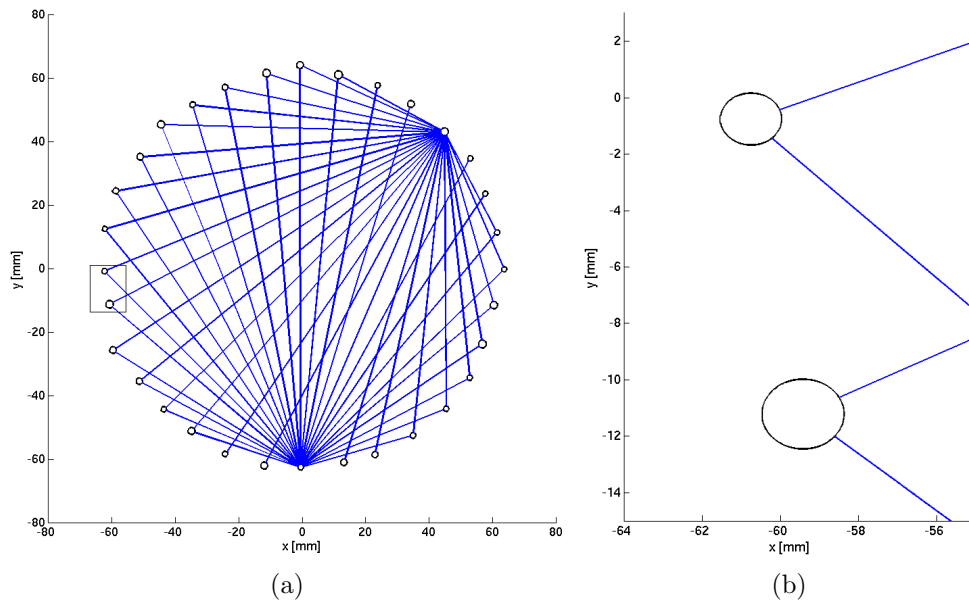


Figure 7.2: Illustration of rays used to determine pairwise transducer distance. (a) Rays used to determine pairwise transducer distances for two different transmitters. (b) Boxed area in (a), detailing how the rays touch at different points on the receiver surface depending on the transmitter location.

The resultant sample matrix is passed to the TOF-matrix-correction procedure, outlined in Algorithm 6.3. This algorithm is expected to remove any inconsistency in signal-arrival time and interpolate missing information. An example of a simulated sample matrix, before and after correction, is shown in Figure 7.3(a) and Figure 7.3(b), respectively.

The corrected sample matrix is converted to a distance matrix and MDS localization is performed. Each computed transducer position is expected to be located at the point on its halo which is closest to the geometric center of the model nodes (see Figure 7.1). However, due to the error introduced into the model data, the computed positions will slightly differ from these expected locations. The transducer positioning error was computed for twenty different random models and the results are summarized in Table 7.1. The overall maximum positioning error was computed

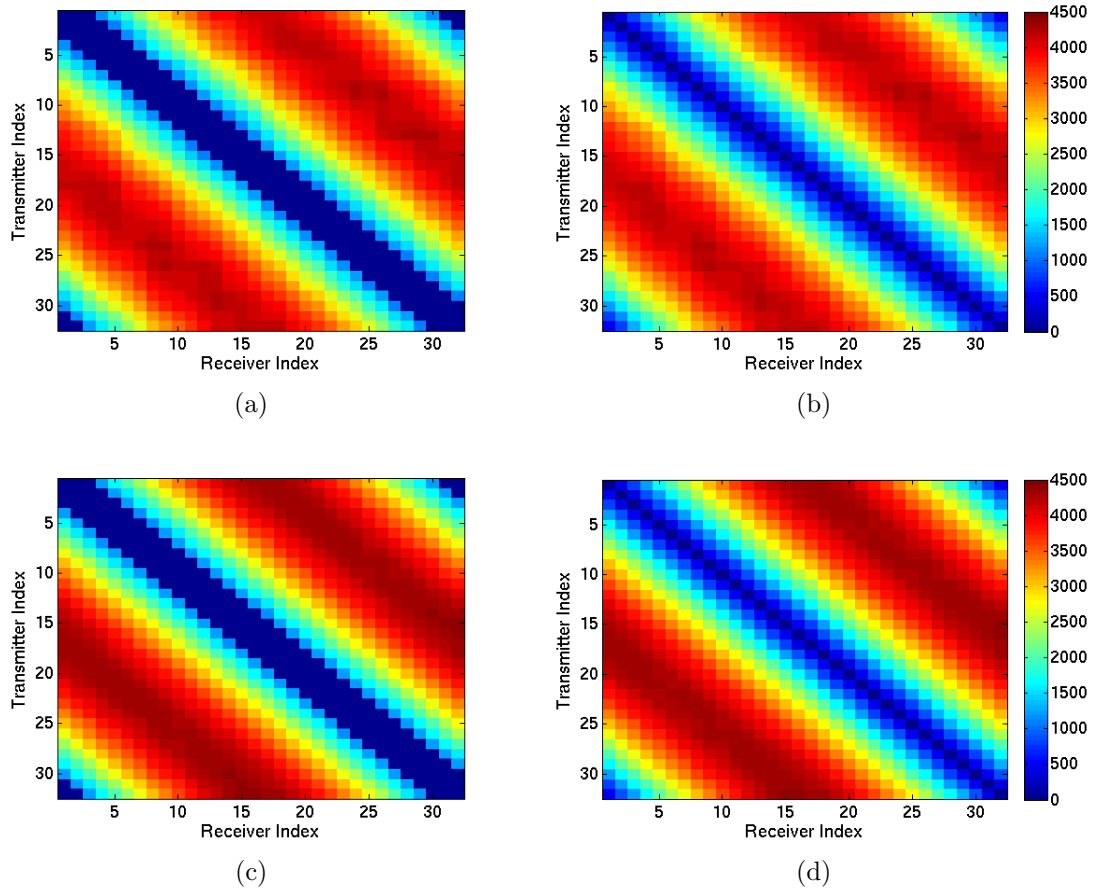


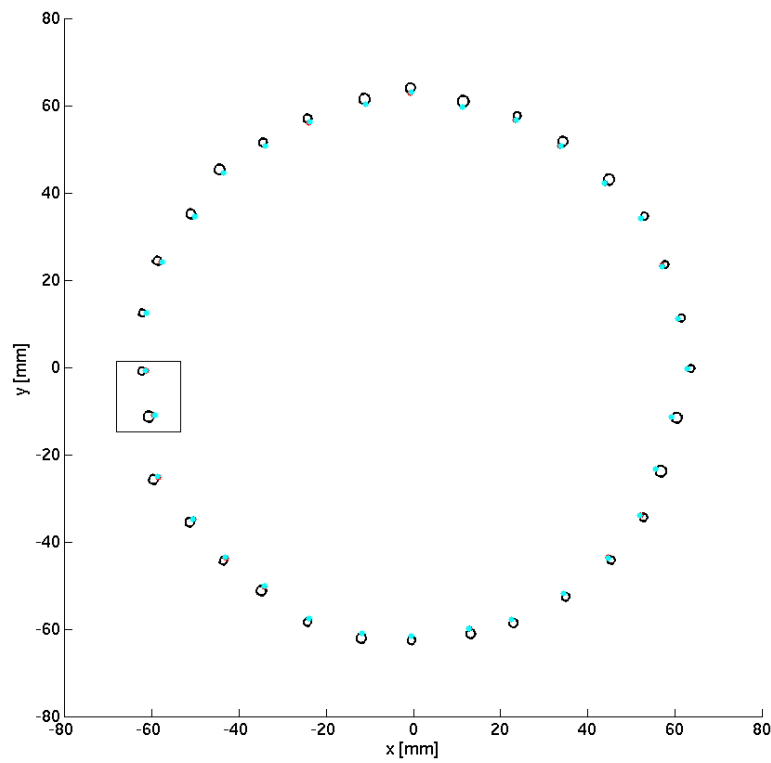
Figure 7.3: Illustration of sample matrices before and after correction. All values are in units of “samples.” (a) Sample matrix for an example model before correction. (b) Sample matrix for an example model after correction. (c) Sample matrix of measurement data before correction. (d) Sample matrix of measurement data after correction.

Model	Maximum Error (mm)	Mean Error (mm)	Standard Deviation (mm)
1	0.14541	0.06575	0.034831
2	0.22645	0.085642	0.052376
3	0.18759	0.069076	0.038752
4	0.17947	0.066323	0.044388
5	0.1606	0.082079	0.039069
6	0.15632	0.065341	0.03508
7	0.14466	0.07742	0.031324
8	0.19465	0.075235	0.039979
9	0.13101	0.065767	0.035813
10	0.27851	0.15367	0.066674
11	0.12834	0.055618	0.02757
12	0.14353	0.052712	0.035383
13	0.13749	0.05989	0.034791
14	0.16809	0.066165	0.035249
15	0.24116	0.087957	0.054682
16	0.1142	0.063862	0.024914
17	0.15587	0.064424	0.038214
18	0.13208	0.061085	0.034628
19	0.13356	0.068746	0.036112
20	0.18369	0.06693	0.042105
Overall	0.27851	0.072685	0.044645

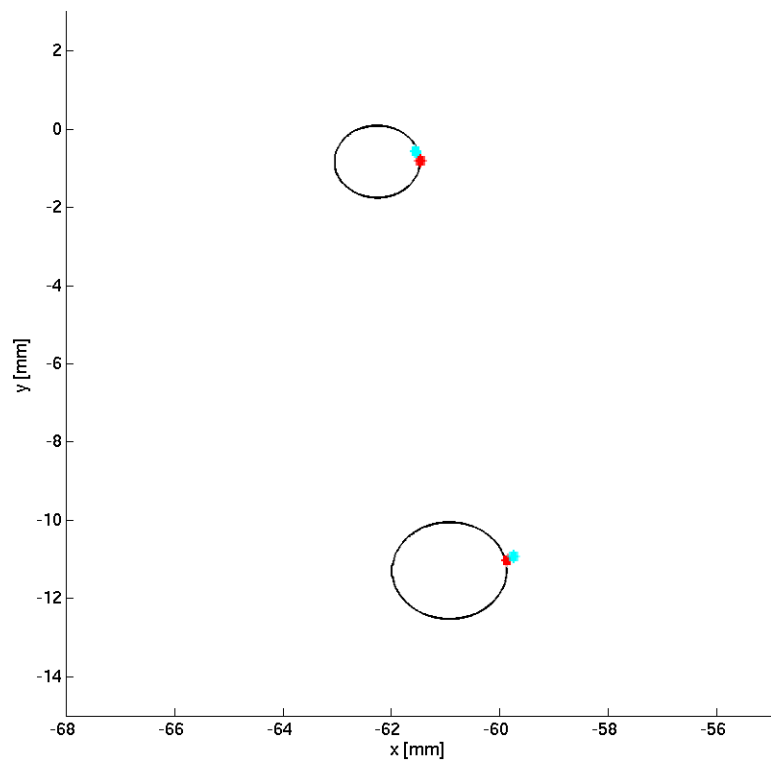
Table 7.1: Summary of transducer positioning error for 20 different random model configurations. The transducer localization method presented in section 6.6.2 was applied to 20 different random models. An outline of the resulting transducer positioning errors are shown. Note that the overall maximum positioning error is less than the tolerable error of 0.5mm

to be less than the maximum error tolerance of 0.5 mm. A comparison of computed versus expected transducer positions for an example model is shown in Figure 7.4. It can be concluded that the localization algorithm correctly determines transducer positions from TOF data within tolerable error.

In order to show that the transducer-ring simulation methods used in this section adequately represent measurement data, a simulated sample matrix is compared to a measured sample matrix in Figure 7.3. It is clear from the comparison that missing



(a)



(b)

Figure 7.4: Comparison of expected and computed transducer positions for an example model. (a) The black circles represent actual locations and sizes of the model transducers. The red points indicate the expected computed locations and the blue points indicate the actual computed locations. (b) Boxed area in (a).

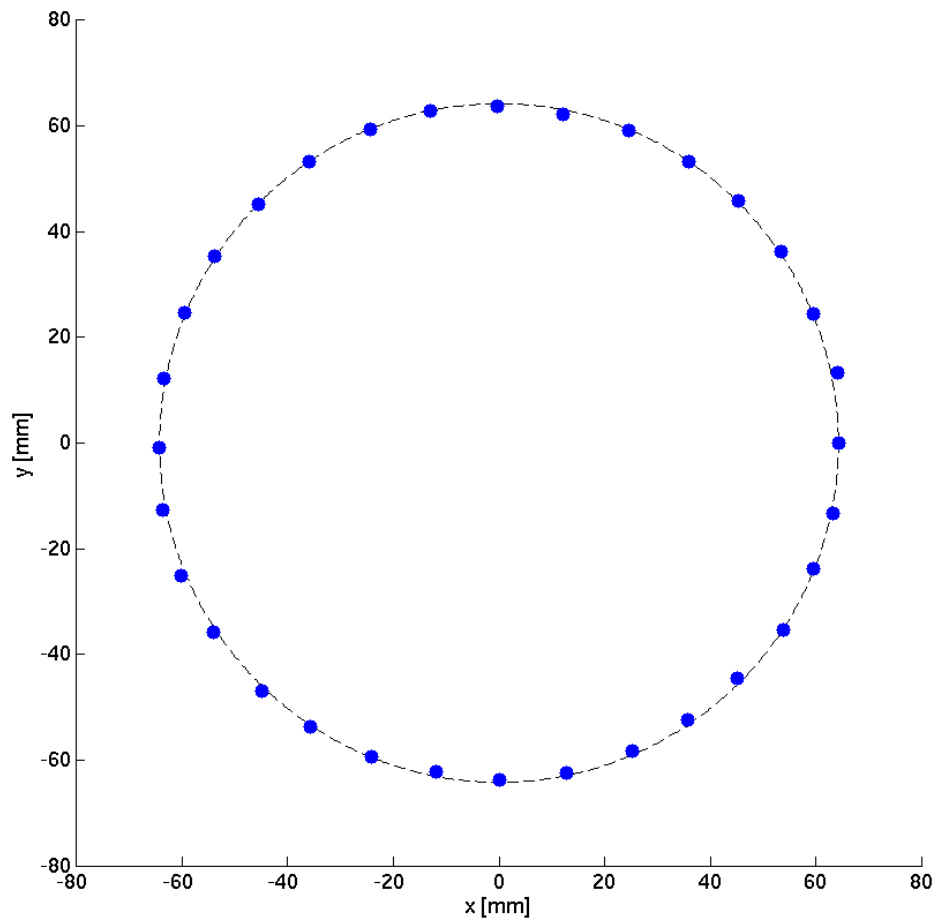


Figure 7.5: Transducer locations computed from measurement data. The dashed line is the best fit circle through the computed transducer positions.

data is interpolated to similar values in both instances. Thus, the results of this section indicate that the localization algorithm correctly handles measurement data and that transducer positions can be determined with sufficient accuracy. The result of transducer localization performed on example measurement data is shown in Figure 7.5.

7.2 Calibration Results

This section examines the effects of calibration on image reconstruction by observing inversions of data prepared by the incident and scattered field calibration techniques. The images presented in this section provide a 2D spatial distribution of the contrast determined by FEM-CSI. The depicted axes provide the spatial information and the colour scale specifies the reconstructed contrast. Note that the colour scale actually denotes normalized contrast values defined as

$$\chi'(\vec{r}) = \chi(\vec{r}) + 1 = \left(\frac{c_b(\vec{r})}{c(\vec{r})} \right)^2. \quad (7.1)$$

7.2.1 The Imaging Phantom

The object imaged in the following subsections is a homogeneous phantom mimicking acoustical properties of human tissue (reconstructions of other objects are provided in Appendix A). The phantom is a mixture of unflavoured gelatin powder (20 g), psyllium fibre (10 g) and boiling water (250 mL) which is refrigerated until congealed [60]. In order to acquire phantom data, a 15 cm column of the gelatinous material is hung into the UST chamber for measurement. The images produced are of its cross-section, which is approximately a 4 mm square with an expected normalized contrast of 0.93.

The phantom contrast is determined from two signal TOF measurements taken between two transducers located diametrically across the UST chamber from each other. The first TOF, t_b , is measured between the transducers in the background medium. If the distance between the transducers is denoted as d_b then the first TOF

can be written as

$$t_b = \frac{d_b}{c_b} \quad (7.2)$$

where c_b is determined from a water temperature measurement and formula (6.30).

The second TOF, t_p , is measured with a slab of phantom material placed between the transducers. If the slab thickness is denoted as d_p then the second TOF can be written as

$$t_p = \frac{d_b - d_p}{c_b} + \frac{d_p}{c_p} \quad (7.3)$$

where c_p is the unknown speed of sound through the phantom. Combining (7.2) and (7.3) we obtain a formula for c_p , independent of transducer distance:

$$c_p = \left(\frac{t_p - t_b}{d_p} + \frac{1}{c_b} \right)^{-1}. \quad (7.4)$$

The computed value of c_p is then be used in (7.1) to obtain the normalized contrast of the phantom.

One final point to note about the phantom is that it has acceptable density discrepancy for imaging with FEM-CSI. This is verified by measuring the weight and volume of a sample taken from the material. Such a phantom can therefore be used to obtain quantitative reconstructions with meaningful contrast values.

7.2.2 Incident Field Calibration

The incident field calibration technique, outlined in Algorithm 6.5, is first tested with synthetic data generated by a 2D-FDTD simulation of phantom measurements. For this simulation, the UST chamber is modelled as a circular domain with absorbing boundaries. The sources are located within the domain and are evenly spaced on a

6.5 cm radius circle around the object of interest. Every source location is also an observation point. The background medium parameters model water and are set to commonly-used average values: $\rho_b = 1000 \text{ kg/m}^3$ and $c_b = 1500 \text{ m/s}$. The phantom is modelled as a square penetrable object with density equal to that of the background medium and a sound speed of 1555 m/s, resulting in a normalized contrast of 0.93. The data generated by the simulation are then subject to an incident field calibration at a frequency of interest of 1.3 MHz.

Reconstructions of the FDTD simulation data are presented in Figure 7.6. For each source, data from only 23 observation points (of the available 32) are used in the inversions to better represent information available in an experimental scenario. Note that for each source, it is always data from the observation points furthest from the source location which are used. Images of FDTD data calibrated with the 2D and 3D incident field models are shown in Figure 7.6(b) and Figure 7.6(c), respectively. A reconstruction of FDTD data without calibration is also provided for comparison in Figure 7.6(a). Finally, an image reconstructed from FEM-simulated data is provided in Figure 7.6(d) to illustrate what is expected when inverting idealized data. It is clear from these images that there is an improvement in reconstructed image quality after applying the incident field calibration to the data.

The incident field calibration is also applied to data collected by the UST system. The necessary time-domain signals are obtained by first performing a total field measurement of the phantom suspended in the UST chamber. The phantom is then removed and an incident field measurement is taken soon after. The incident field calibration algorithm is then applied to the acquired signal data at the frequency of interest of 1.3 MHz. The resulting reconstructions are presented in Figure 7.7. Calibration with the 2D and 3D incident field models is tested and both produce similar

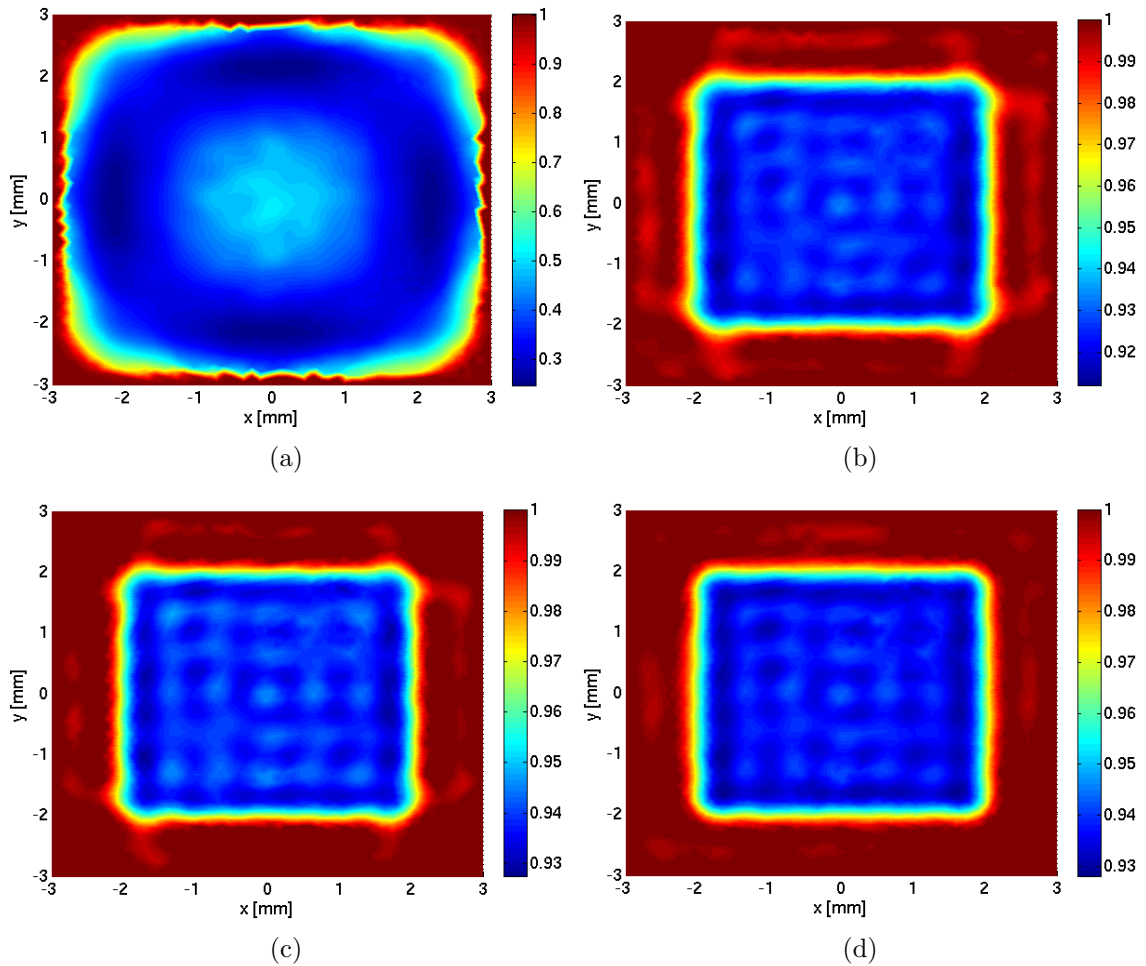


Figure 7.6: Reconstructions of FDTD data after the application of the incident field calibration. Each calibration is performed with information from 23 observation points for each of the 32 source locations. The expected image is a 4 mm square with $\chi' = 0.93$ (a) Reconstruction of FDTD data before calibration. (b) Reconstruction of FDTD data after calibration with the 2D point-source incident field model. (c) Reconstruction of FDTD data after calibration with the 3D point-source incident field model. (d) Reconstruction of idealized FEM data, provided as a model reference.

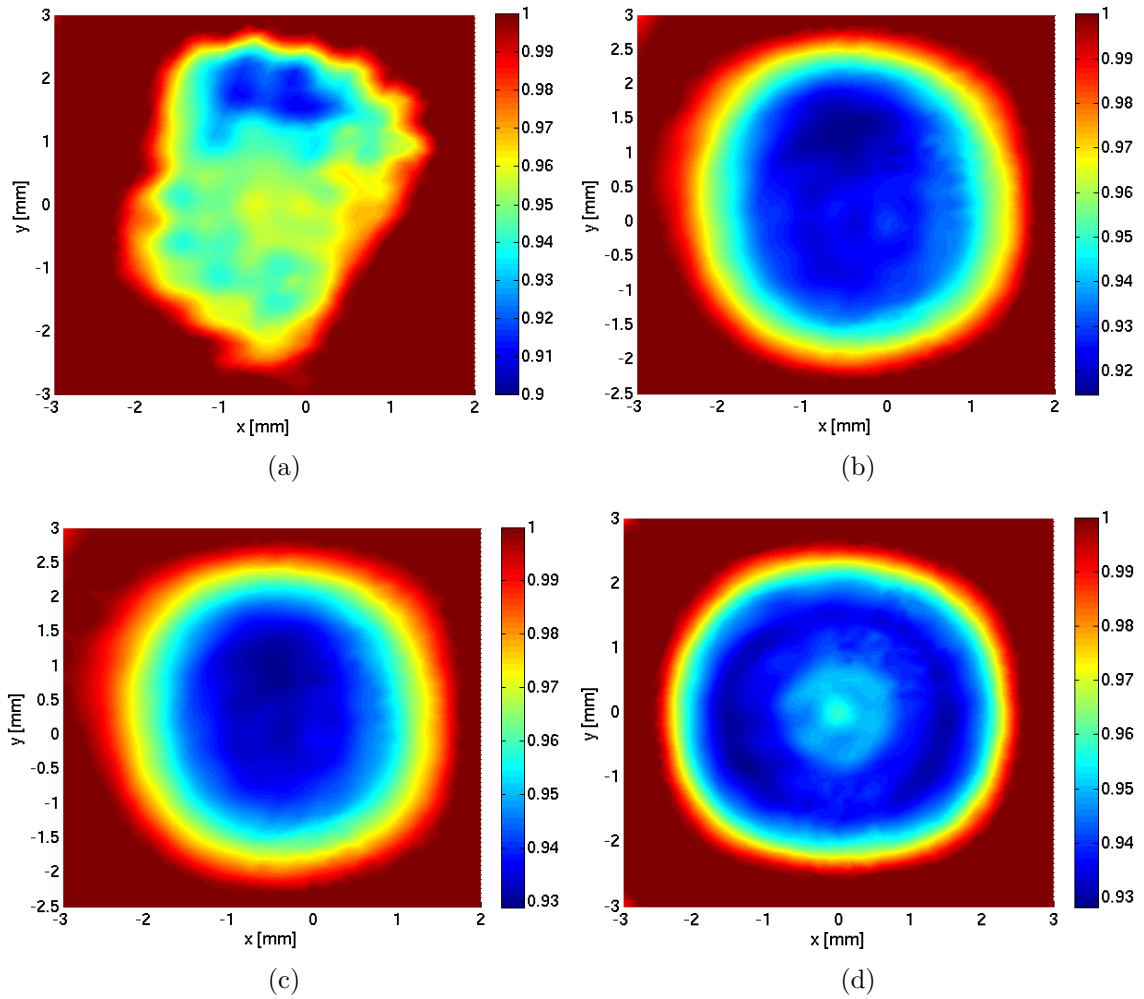


Figure 7.7: Images of human-tissue phantom data measured at 1.3 MHz where 3 receivers per transmitter are used. The expected image is a 4 mm square with $\chi' = 0.93$. (a) Image reconstruction before calibration. (b) Image after incident field calibration using the 2D point-source incident field model. (c) Image after incident field calibration using the 3D point-source incident field model. (d) Image reconstructed from synthetic FEM data.

shape reconstructions as can be seen in Figure 7.7(b) and Figure 7.7(c), respectively. The inversion result without calibration and a reconstruction of idealized synthetic data are provided for comparison in Figure 7.7(a) and Figure 7.7(d), respectively. It can be observed that inversion results are improved after calibration with either incident field model but the determined contrast values are in better agreement with the idealized case when the 3D point-source is used.

Data from only 3 receivers (of the available 31) per transmitter were used for the inversions depicted in Figure 7.7. The effect of using more receivers with the incident field calibration is illustrated in Figure 7.8; the chosen receivers are always those furthest from the active transmitter. As can be seen, reconstruction quality degrades with an increasing number of receivers. This is contrary to what is expected in a model scenario. Using data from more receivers should imply that more information is available to the inversion algorithm and should therefore produce a more accurate reconstruction. This is shown in Figure 7.9 with inversions of the FDTD data for the 4 mm square object. We see that the use of data from more observation points certainly does not worsen the inversion results.

The unfavourable results shown in Figure 7.8 could be the result of significant inconsistency distortion (described in section 6.6.3) and random noise present in the data acquired by the additional receivers. It has been observed that the measured scattered field is weak at these transducers and is therefore highly affected by these types of perturbations. The effects of noise on image reconstruction is further examined in the context of the scattered field calibration in section 7.2.3. The poor reconstructions could also be due to the difference in incident and scattered signal arrival angles. A theoretical argument was presented in section 6.7 to show that this effect can have a significant impact on the effectiveness of the incident field calibra-

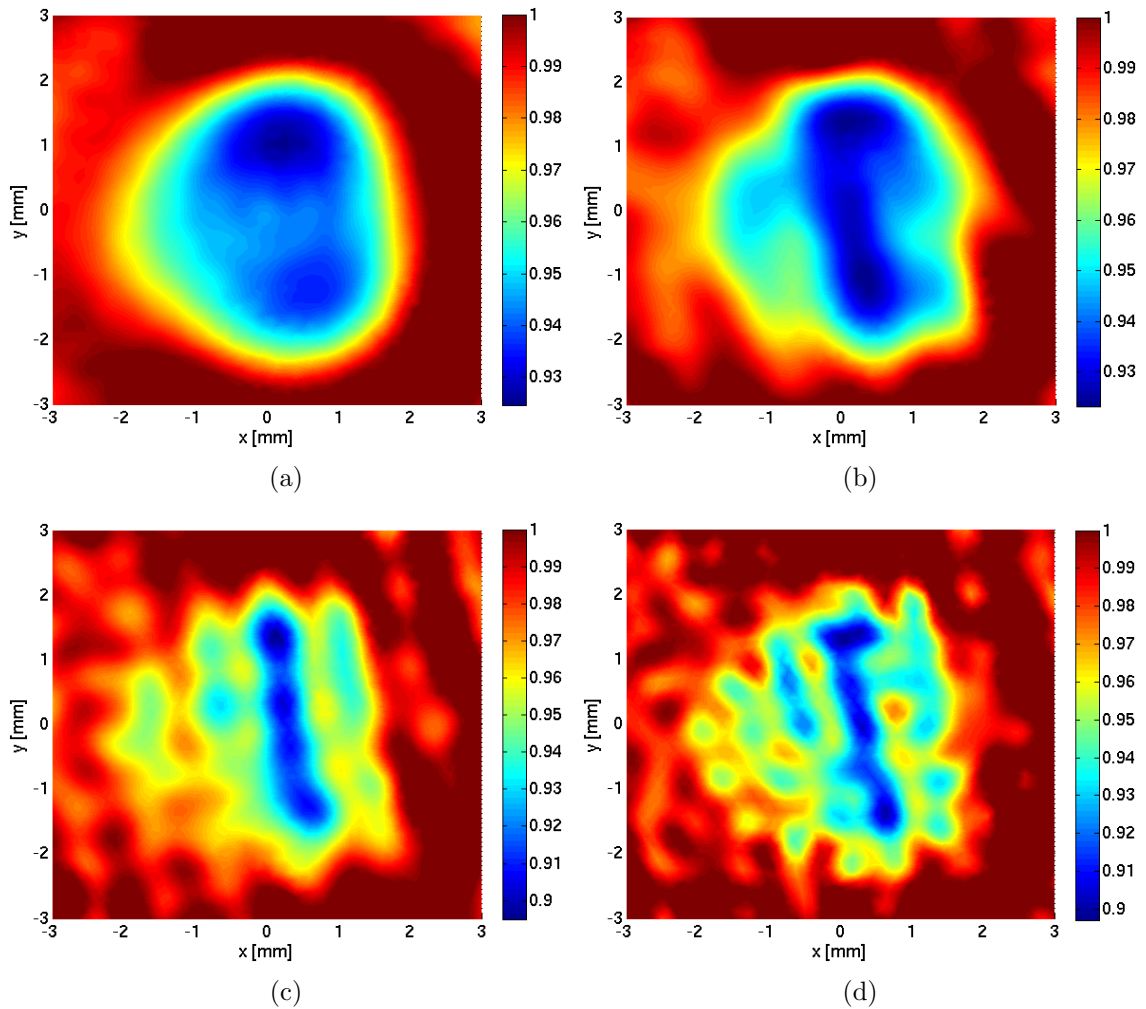


Figure 7.8: Reconstructions of phantom data calibrated with the incident field calibration when different numbers of receivers are used in the inversion. The series of images shows how reconstruction quality degrades as more receivers are used in the inversion of measurement data. The chosen receivers are always those furthest from the active transmitter. (a) Reconstruction with 5 receivers. (b) Reconstruction with 11 receivers. (c) Reconstruction with 17 receivers. (d) Reconstruction with 23 receivers.

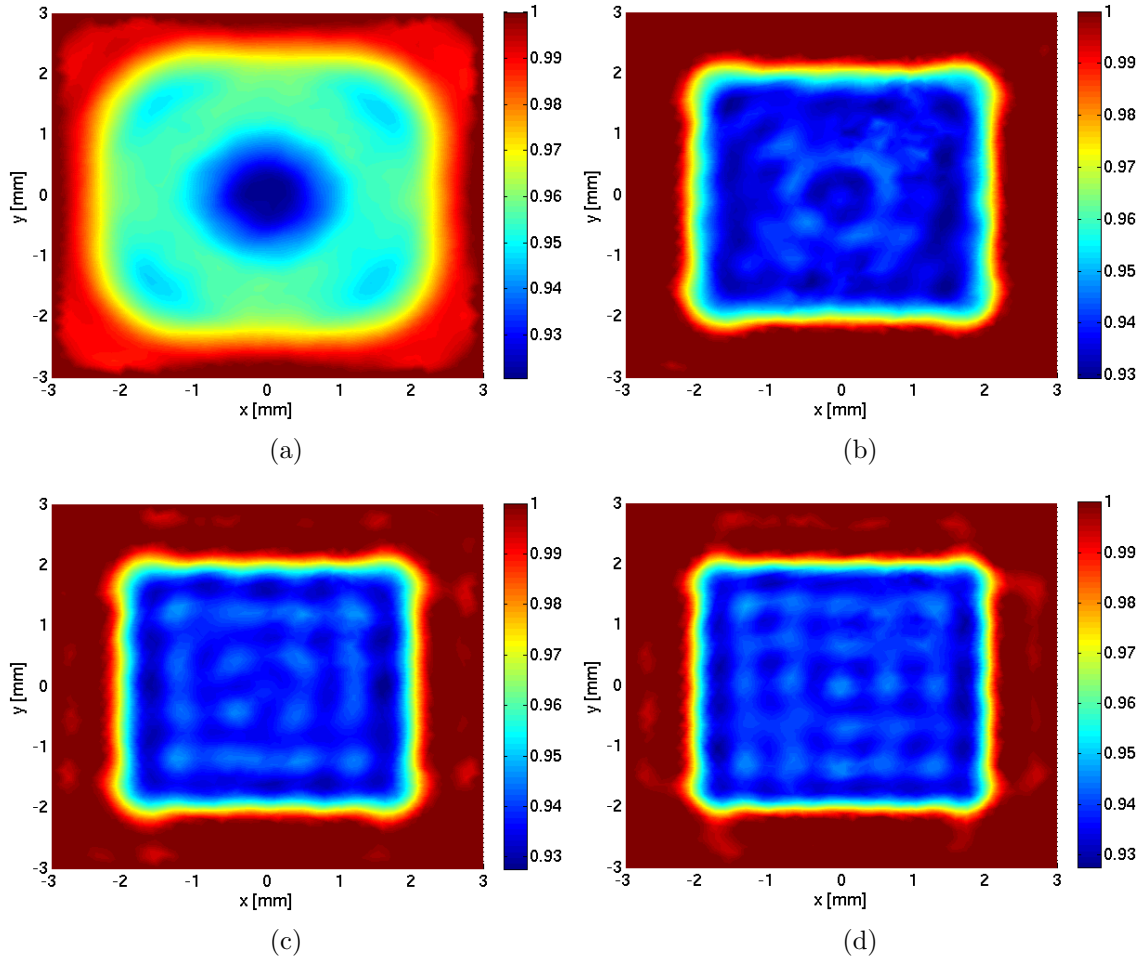


Figure 7.9: Reconstructions of calibrated FDTD data when different numbers of observation points are used in the inversion. The images shown indicate that reconstruction quality should not degrade when more observation point data per source are included in the inversion. (a) Inversion with 5 observation points. (b) Inversion with 11 observation points. (c) Inversion with 17 observation points. (d) Inversion with 23 observation points.

tion when applied to data from transmitter-receiver pairs for which relative positions are not diametrically across the UST chamber. If this is the case in practice then the data from additional receivers would not be properly calibrated and would reduce the ability of the inversion algorithm to converge to a correct result.

7.2.3 Scattered Field Calibration

The scattered field calibration technique, outlined in Algorithm 6.6, is first tested with synthetic data generated by a 2D-FDTD simulation. The simulation domain and phantom are modelled as described in the incident field calibration section above. The calibration object is modelled as a soft, 3 mm radius circle and is centered in the FDTD simulation domain. The data are then subject to a scattered field calibration at a frequency of interest of 1.3 MHz.

Reconstructions of the FDTD simulation data are presented in Figure 7.10. For each source, data from only 23 observation points (of the available 32) are used in the inversions. As always, it is data from the observation points furthest from the source location which are used. The necessary calibration coefficients are determined with the help of a FEM model of the calibration object, as described in section 6.5.2. The 2D and 3D point-source models are both tested as the incident field in the FEM simulation. The inversion result of implicitly calibrating with the 2D point-source is shown in Figure 7.10(b) and with the 3D point-source in Figure 7.10(c). The reconstructions are very similar for both calibration object models and both agree very well with the image computed from the idealized data shown in Figure 7.10(d). The inversion result obtained before calibration is reproduced in Figure 7.10(a) for comparison. It is clear from these images that there is an improvement in reconstructed image quality after applying the scattered field calibration to the data.

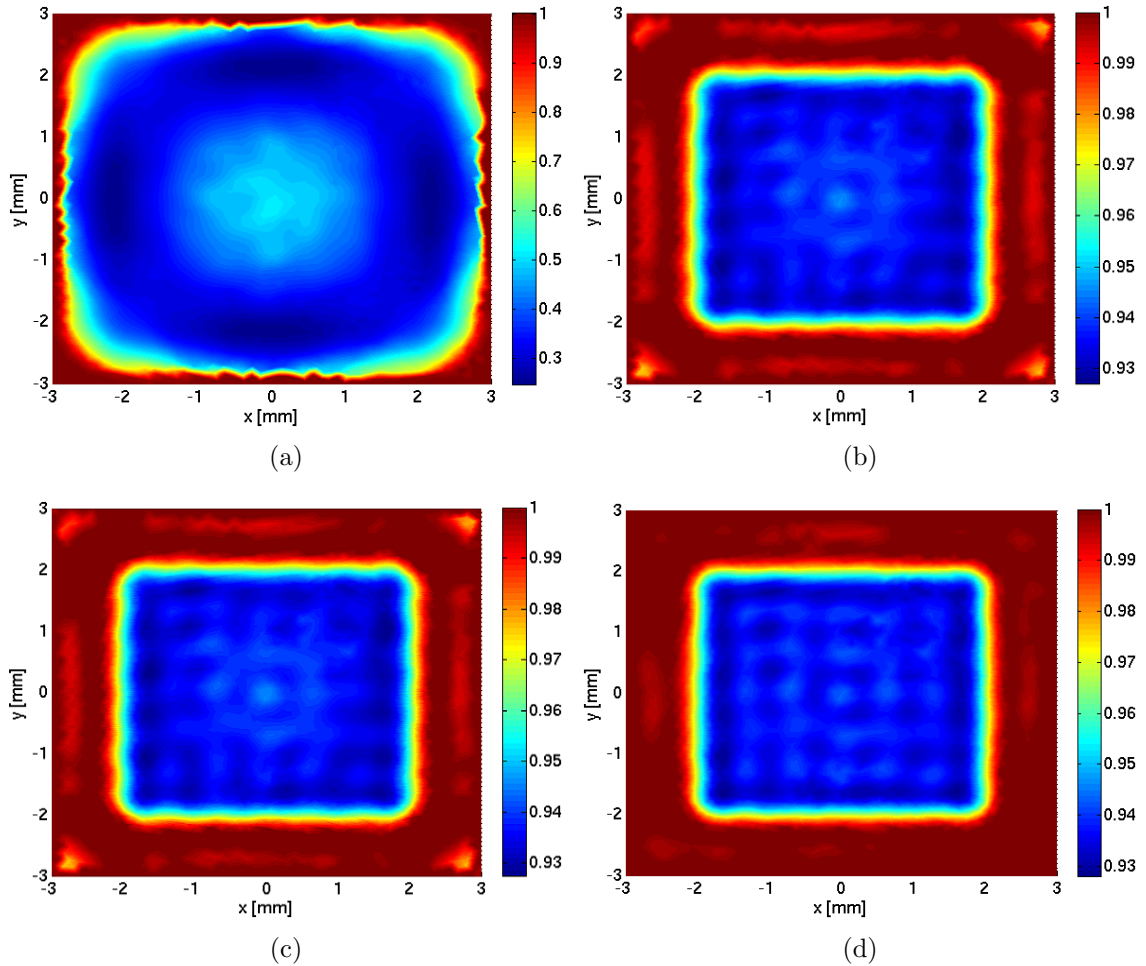


Figure 7.10: Reconstructions of FDTD data after the application of the scattered field calibration. Each calibration is performed with information from 23 observation points for each of the 32 source locations. The expected image is a 4 mm square with $\chi' = 0.93$ (a) Reconstruction of FDTD data before calibration. (b) Reconstruction of FDTD data after calibration with a 2D point-source calibration object model. (c) Reconstruction of FDTD data after calibration with a 3D point-source calibration object model. (d) Reconstruction of idealized FEM data, provided as a model reference.

The scattered field calibration is also applied to the measured data of the gelatin-based phantom described in the previous section. As mentioned before, the necessary time-domain signals are obtained by first performing a total field measurement of the phantom and an incident field measurement soon after. The time-domain signals of the calibration object are collected following the incident field acquisition. The calibration object is a 6 mm diameter air-filled straw and is suspended vertically in the UST chamber during measurement. It is simulated via the FEM as a soft scatterer for the determination of calibration coefficients. Note that knowledge of the calibration object location relative to the receiver positions is required for the FEM model. This information is determined by visual inspection of a reconstructed image of the object. It is produced by inverting measurement data of the calibration object after applying the incident field calibration. See Appendix A for sample reconstructions of the calibration object.

The calibrated phantom data is reconstructed with FEM-CSI to obtain 2D images of its cross-section. The results are shown in Figure 7.11 for a frequency of interest of 1.3 MHz. Calibration with implicit 2D and 3D point-source models is tested and both produce very similar reconstructions as can be seen in Figure 7.11(b) and Figure 7.11(c), respectively. It can also be observed that the edges of the reconstructed object are not well defined and that the contrast values differ significantly from the inversion result of idealized data in Figure 7.11(d). The reconstruction obtained when no calibration is applied is reproduced in Figure 7.11(a) for comparison. Whether image quality is improved after calibration is questionable.

Some of the problems seen in the reconstructions of experimental data could be attributed to inadequate modelling of the calibration object. Two potential concerns surrounding this aspect of the calibration process are identified here. One issue is

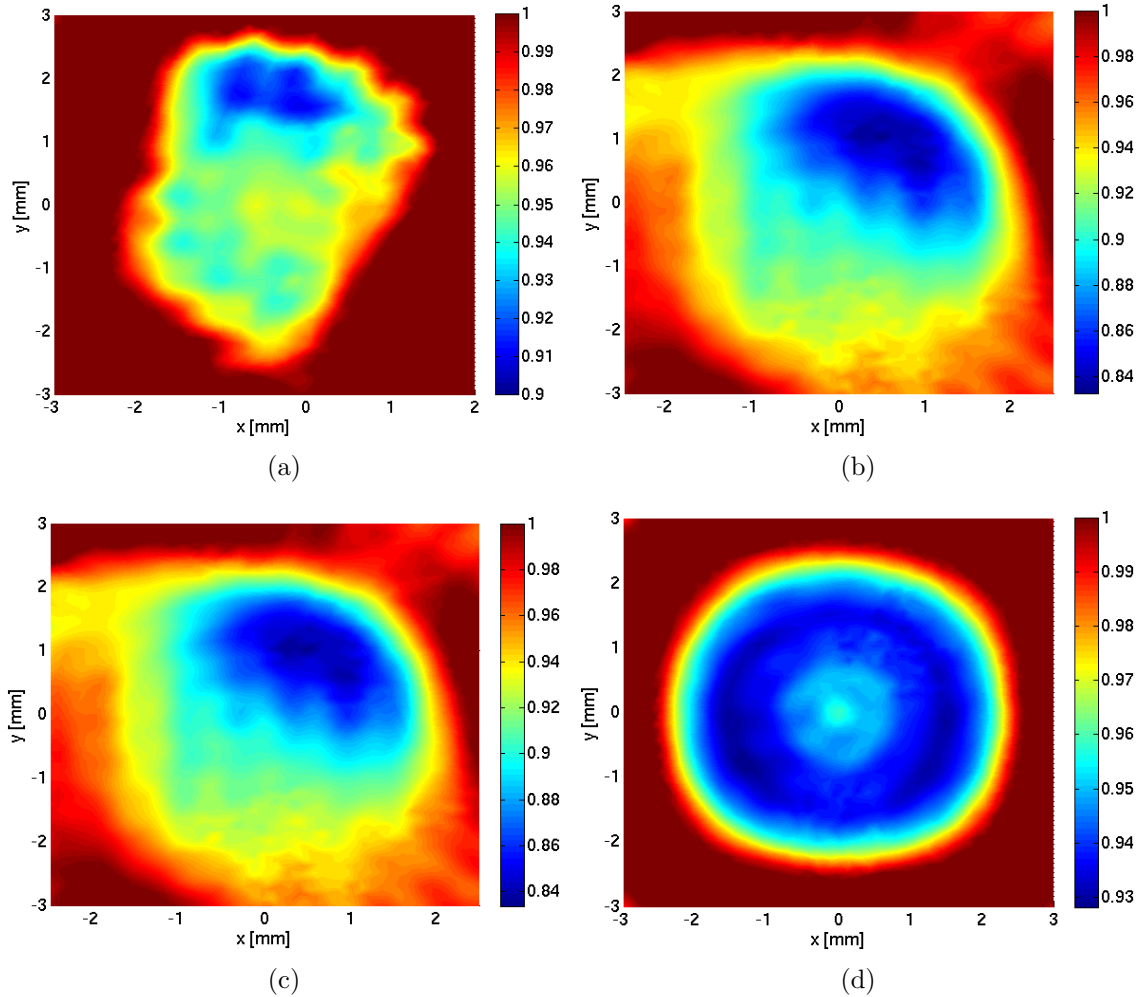


Figure 7.11: Reconstructions of phantom data after the application of the scattered field calibration. Each calibration is performed with information from 3 receivers for each of the 32 transmitters. The expected image is a 4 mm square with $\chi' = 0.93$ (a) Reconstruction of phantom data before calibration. (b) Reconstruction of phantom data after calibration with a 2D point-source calibration object model. (c) Reconstruction of phantom data after calibration with a 3D point-source calibration object model. (d) Reconstruction of idealized FEM data, provided as a model reference.

that the air-filled straw is modelled as a soft scatterer, ergo the straw wall is not taken into account in the FEM simulation. Modelling the calibration object in this manner relies on the assumption that the wall has low contrast and is thin enough to negligibly disturb the signals scattered by the air within. However, this assumption is difficult to verify because the acoustical properties of the straw wall are unknown and a “negligible disturbance” is hard to quantify. Another known issue is the difficulty in accurately determining the location of the calibration object with respect to the receiver positions. An estimate of its location can be obtained from images produced with data prepared via the incident field calibration but effectiveness of this approach is not entirely reliable.

Data from only 3 receivers (of the available 31) per transmitter were used for the inversions depicted in Figure 7.11. The effect of using more receivers with the scattered field calibration is illustrated in Figure 7.12. It can be observed that reconstruction quality is reduced as the number of receivers is increased. This result is, again, contrary to what is expected. Investigation into the matter reveals that, in the case of the phantom data, only the few receivers diametrically across from the transmitter record a significant scattered field. The scattered signals measured by the other receivers are those deflected by the phantom and are substantially corrupted by noise due to their very small amplitude. When data from these receivers are used, it has the effect of incorporating noisy and conflicting information into the inversion. In other words, the signal-to-noise ratio (SNR) of the scattered field for these receivers is too low and should not be used.

The justification given above can be verified by conducting a simple simulation. A 4 mm square object with $\chi' = 0.93$ is simulated using 2D-FDTD to first represent noise-free scattered field measurements of the phantom. The simulation results show

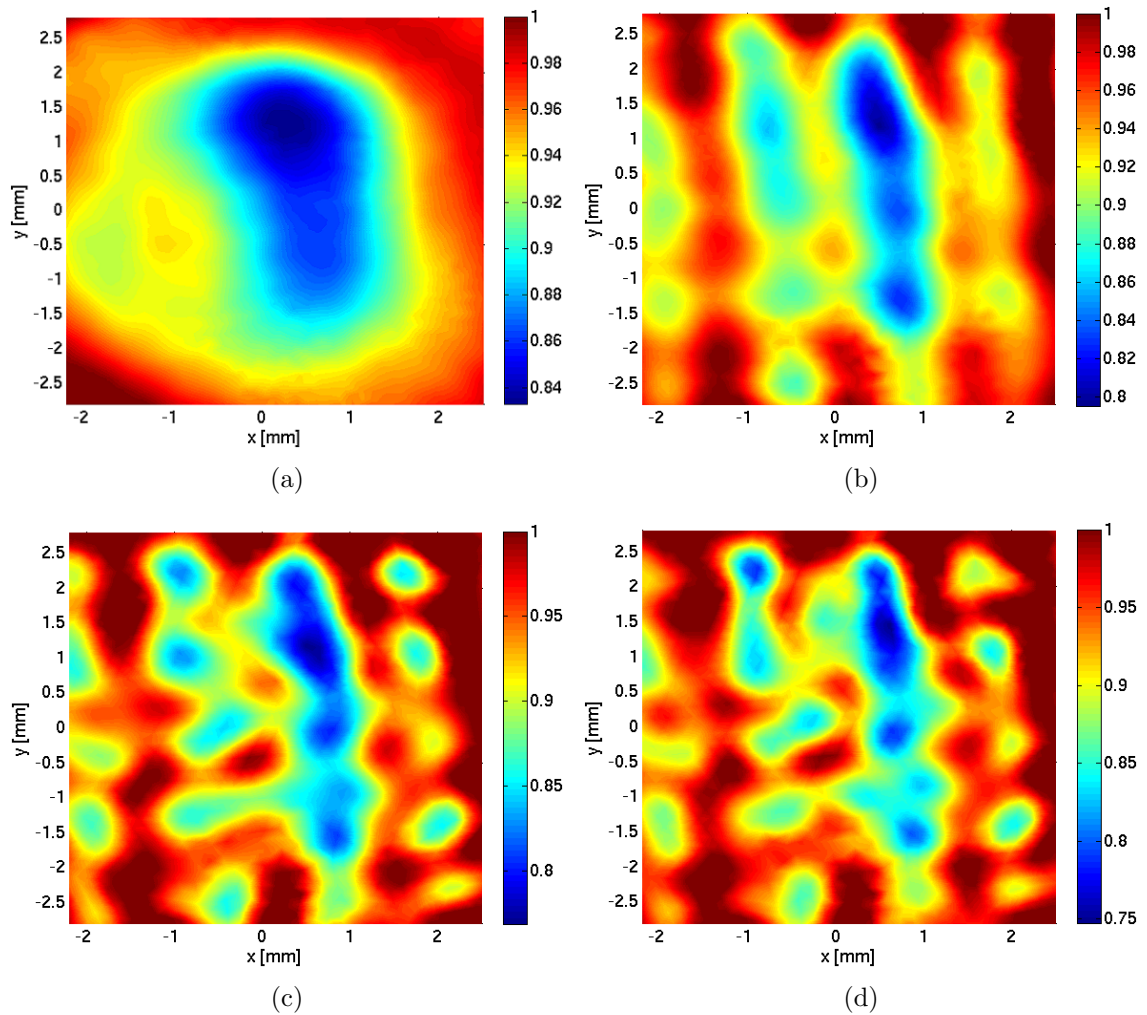


Figure 7.12: Reconstructions of phantom data calibrated with the scattered field calibration when different numbers of receivers are used in the inversion. The frequency of interest is 1.3 MHz and the expected image is a 4 mm square with $\chi' = 0.93$. (a) Reconstruction for 5 receivers per transmitter. (b) Reconstruction for 11 receivers per transmitter. (c) Reconstruction for 17 receivers per transmitter. (d) Reconstruction for 23 receivers per transmitter.

that, in most cases, the deflected signal amplitude is less than 1% of the scattered field determined at the observation point positioned diametrically from the source. This indicates that a significant scattered field cannot be expected at most receivers when taking measurements of the phantom. In order to simulate the effects of low SNR, artificial inconsistency distortion and random noise are superimposed onto the time-domain scattered field data of the simulated phantom. For each transducer pair, inconsistency distortion is modelled as a 1.3 MHz sinusoid with a random phase shift and a peak amplitude of 6% of the maximum simulated scattered field amplitude. The random noise has a maximum magnitude of 2% of the maximum simulated scattered field amplitude and is generated from a uniform probability distribution. The noise levels are chosen to reflect what is observed experimentally. The scattered field calibration is then applied to the noisy FDTD data and the inversion results are shown in Figure 7.13. It can be observed that reconstruction quality is reduced as the number of receivers is increased in a manner similar to the experimental results.

The simulation described above allows us to specifically examine the effects of time-domain noise on calibration and image reconstruction. Other sources of error are eliminated because the true transducer locations are known and there is no notion of dissimilar signal arrival angles in the FDTD model. Furthermore, it can be inferred from the inversion results of noise-free FDTD data in Figure 7.10 that little error is introduced by the calibration procedure alone. The results of this noise study therefore indicate that the SNR at receivers capturing a deflected signal is of concern.

The reconstructions of Figure 7.8 and Figure 7.12 show that including data from more receivers has the effect of reducing image quality for both calibration schemes. This result has been found to be partly due to a poor SNR at the additional receivers. For this reason, the effectiveness of the presented calibration schemes cannot be fully

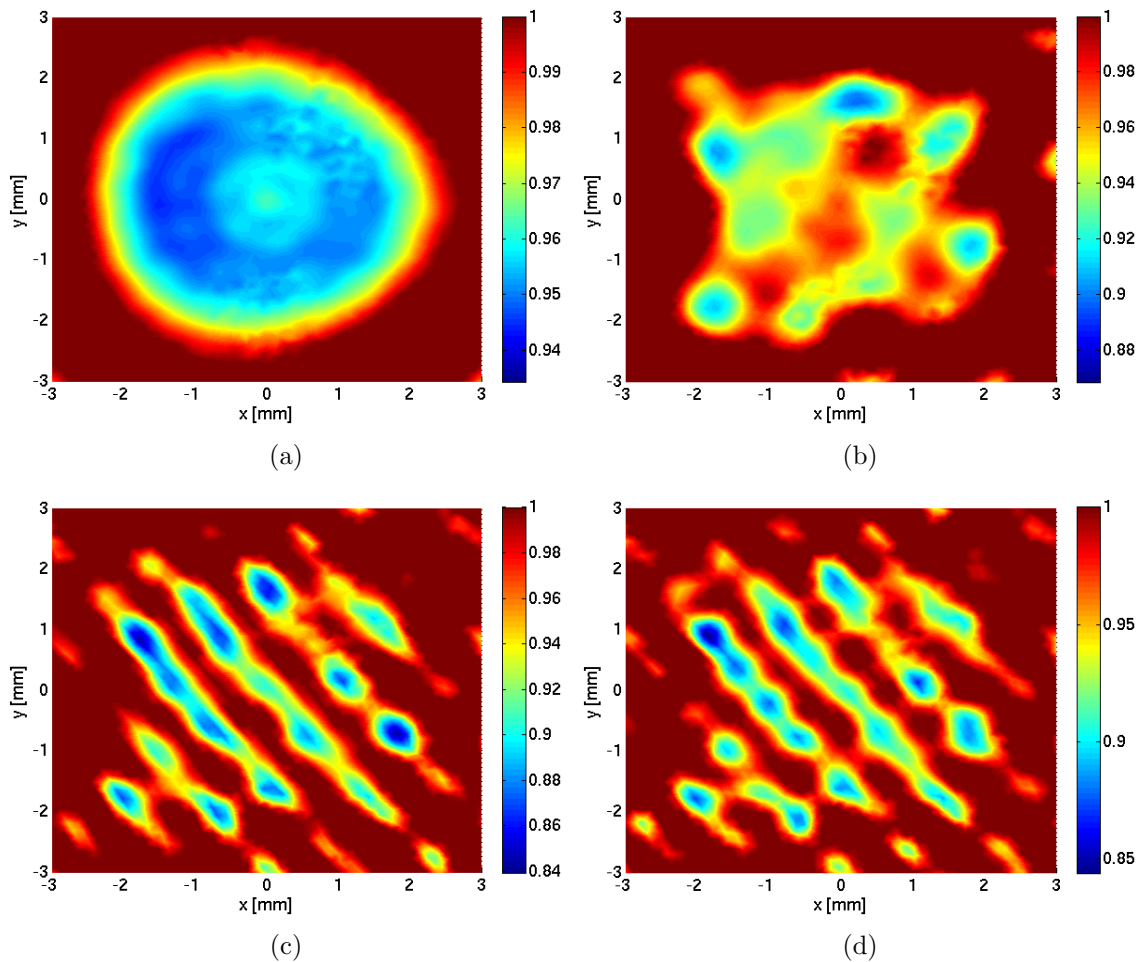


Figure 7.13: Images of a noisy FDTD-simulated phantom with the scattered field calibration. The frequency of interest is 1.3 MHz and the expected image is a 4 mm square with $\chi' = 0.93$. (a) Reconstruction for 3 observation points per source location. (b) Reconstruction for 11 observation points per source location. (c) Reconstruction for 17 observation points per source location. (d) Reconstruction for 23 observation points per source location.

verified with data from more receivers until the SNR is adequately improved. Moreover, it is only by meeting this condition that the influence of dissimilar signal arrival angles can be evaluated in the context of the incident field calibration.

7.2.4 Time-Domain Windowing

The reconstructions of measurement data presented in this chapter are derived from time-domain signals that are subjected to the windowing process described in section 6.6.3. Windowing has the effect of mitigating the detrimental effects of noise on calibration and inversion. In order to demonstrate its impact on image reconstruction, inversions of the phantom data are carried out for different windowing domain radii. The calibration and inversion parameters used here are otherwise the same as the ones that produced the image of Figure 7.7(c). The results are shown in Figure 7.14. As can be observed, image quality is improved as the windowing domain size is reduced to better match the dimensions of the target. This result is expected because a windowing domain which closely encircles the object of interest allows the window function to remove the most noise from the time-domain signal without disrupting meaningful data.

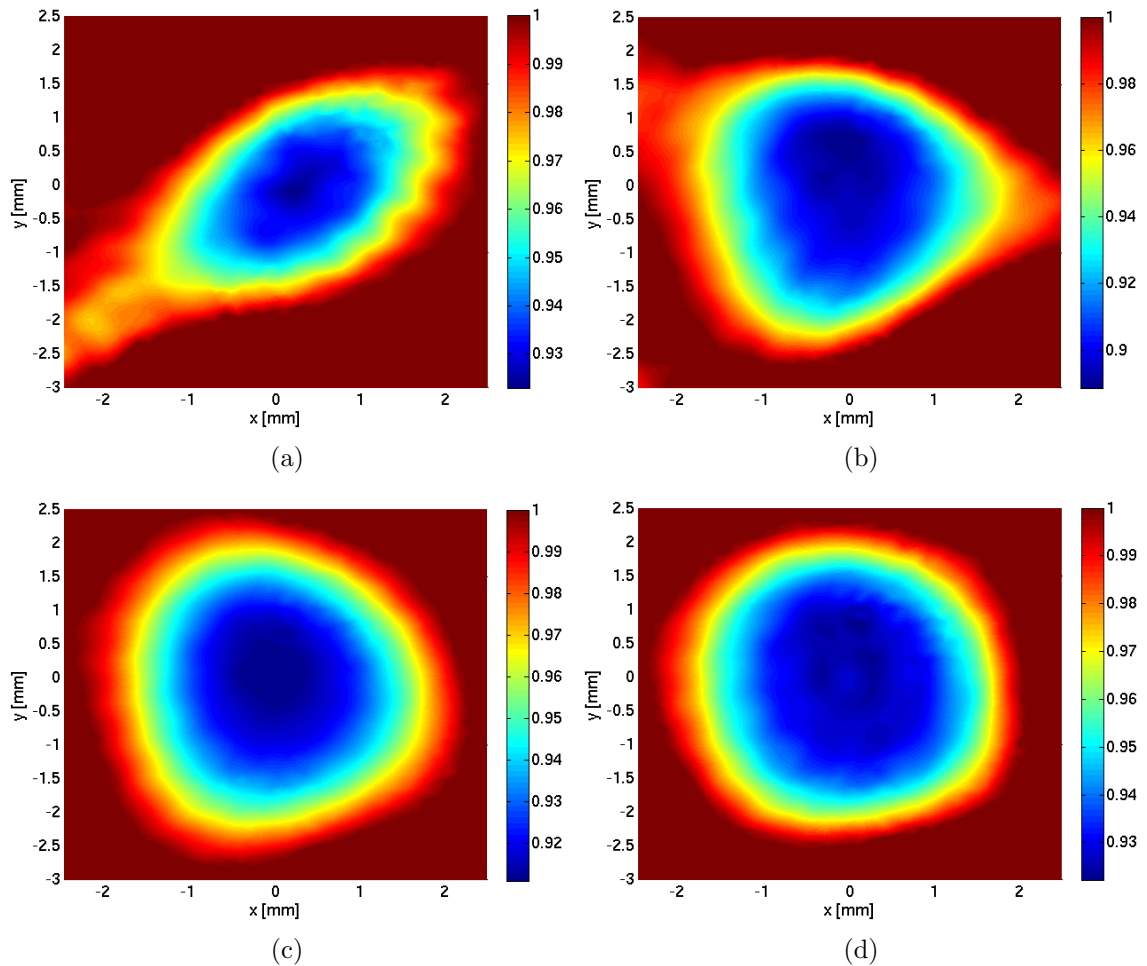


Figure 7.14: Reconstructions of calibrated phantom data for different windowing domain sizes. The expected image is a 4 mm square with $\chi' = 0.93$. It can be observed that image quality improves as the window size is reduced to better match the dimensions of the target. (a) Reconstruction when windowing is not applied. (b) Reconstruction for a 40 mm window radius. (c) Reconstruction for a 15 mm window radius. (d) Reconstruction for a 4 mm window radius.

8

Conclusions and Future Work

This dissertation outlined two calibration techniques and related signal processing methods that may be used to prepare data measured by the UMEIL's UST system for imaging with FEM-CSI. This work also detailed the development of some simulation techniques and mathematical models of acoustic wave behaviour. The following is a summary of observations and conclusions that can be drawn from the presented work.

- Models of electromagnetic and acoustic wave behaviour share many parallel concepts. This insight helped in the development of acoustical FDTD simulation software based on existing algorithms written for Maxwell's equations. It also allowed FEM-CSI, an imaging algorithm originally designed for microwave tomography, to be used in the context of ultrasound.
- The incident and scattered field calibration techniques were applied to FDTD-simulation data for imaging with FEM-CSI. Both schemes demonstrated a significant improvement in image reconstruction quality after calibration. The inversion results closely matched those obtained by inverting idealized synthetic data.
- The incident field calibration technique was applied to measurement data for imaging with FEM-CSI. This calibration method requires a model of ultrasound

wave propagation in an unbounded medium. Two such models were verified and, in both cases, better inversion results were obtained after calibration. Calibration with the 3D point-source model produced image reconstructions which more closely matched the inversion of synthetic data.

- The scattered field calibration technique was used to prepare measurement data for imaging with FEM-CSI. This calibration method requires a model of ultrasound scattering from a well characterized calibration object. Inversion results obtained after applying this calibration scheme indicated that certain challenges concerning the calibration object must still be addressed. Namely, a more accurate determination of its location with respect to transducer positions is needed and a more appropriate model of its acoustical response is required.
- Certain concerns regarding measurements made with the UST system have been identified. There is the issue of inconsistency distortion which is caused by slight fluctuations in recorded signals. This problem causes a poor SNR for the measured scattered field at most receivers which greatly reduces the amount of data suitable for inversion. The cause of this inconsistency is currently unknown. The potential issue of variable transducer system-functions is also of concern. If the system functions of the mounted transducers vary with respect to signal angle of departure and arrival then the incident field calibration may not be valid for most transmitter-receiver pairs. This effect has only been described theoretically and cannot be verified experimentally before inconsistency distortion is sufficiently reduced.
- The implementation of signal processing techniques such as time-domain windowing and TOF correction contributed to better overall image reconstruction.

It was shown through experiment that windowing improves the reconstruction of a target's shape and contrast information. It was also demonstrated via simulation that the employed transducer localization technique is capable of determining effective transducer locations within acceptable error bounds.

8.1 Future Work

Several improvements can be made to the UST system and the overall imaging procedure. The following is a list of possible modifications which could be implemented to improve image reconstruction in the future.

- A greater assortment of targets could be imaged if FEM-CSI were modified to support larger objects and more significant density variations in the imaging domain. Support for the latter is of particular concern in the context of medical imaging because differences in human soft-tissue densities readily exceed the 3% density-discrepancy tolerance [61]. If these capabilities are beyond FEM-CSI then a different imaging algorithm based on the Born iterative method or one involving simultaneous reconstruction of bulk modulus and density may be viable alternatives [62, 63].
- A solution to the inconsistency distortion problem will have to be found because it is a significant source of noise in the measurement system. A possible solution may be discovered by examining different source waveforms and their effect on transducer ringing. It may also be possible to achieve more consistent signal measurements through the use of advanced signal averaging techniques [64, 65].
- Whether transducer system-functions change significantly with respect to signal angle can be verified after inconsistency distortion is reduced. If this is in fact a

problem then research into more suitable transducers will have to be made in order to properly apply the incident field calibration to more transducer pairs. It may be beneficial to consider the use of smaller transducers or the implementation of a ring transducer-array similar to the ones employed by Waag and at the Karmanos Cancer Institute [14, 15]. It may also be worthwhile to investigate the use of capacitive micro-machined ultrasonic transducers (CMUT) due to advantages this new technology may possess over piezoelectric crystals [66, 67].

- If the scattered field calibration is to be properly applied in the context of ultrasound, it will be necessary to overcome some of the difficulties associated with the technique. It will be important to obtain an accurate model of a well characterized calibration object and to develop a method for precisely determining its location with respect to the transducer positions.
- The transducers of the UST system are configured to function in either transmit mode or receive mode during a data acquisition, never both. It may be valuable to add the capability to receive data on a transmitting transducer because it would allow for the implementation of different types of calibration schemes. The pulse-echo information that could be measured may also lead to an effective technique for locating a calibration object with respect to the transducer positions.
- Finally, the 2D principles developed in this work may be extended to 3D imaging. Appropriate modifications would have to be made to the imaging algorithm and calibration procedures. In particular, the TOF and MDS algorithms would have to be adapted for transducer localization in the third dimension.

A

Additional Inversion Results

This appendix presents inversion results of several objects that were tested with the UST system. The first set of images, shown in Figure A.1, depicts reconstructions of the calibration object (air-filled straw). These images are a sample of what is used to determine its position with respect to transducer locations. Inversions of the human-tissue phantom at different frequencies are provided in Figure A.2 and Figure A.3. Reconstructions of two different wire arrangements are given in Figure A.4 and Figure A.5 in order to demonstrate the capabilities of FEM-CSI in the context of UST when applied to small, high-contrast targets. Finally, reconstructions of a high-density polyethylene rod are shown in Figure A.6. This relatively large phantom has a density discrepancy of nearly 6% and is used to experimentally verify the limitations of FEM-CSI.

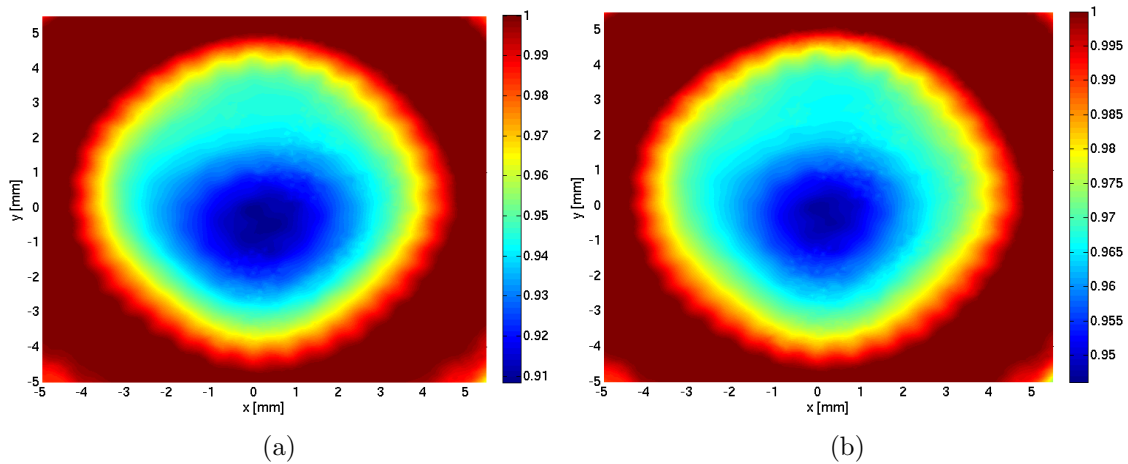


Figure A.1: Reconstructions of the calibration object after applying the incident field calibration. The calibration object is a 6 mm diameter air-filled straw. The inversions are performed with information from 3 receivers for each of the 32 transmitters. The location of the calibration object may be determined by inspection of these images. This information is used in the FEM model required for the scattered field calibration. Note that the reconstructed contrast values have little meaning because the density of the calibration object (air) is very different from that of the background medium (water). (a) Reconstruction of the calibration object after calibration with a 2D point-source incident field model. (b) Reconstruction of the calibration object after calibration with a 3D point-source incident field model.

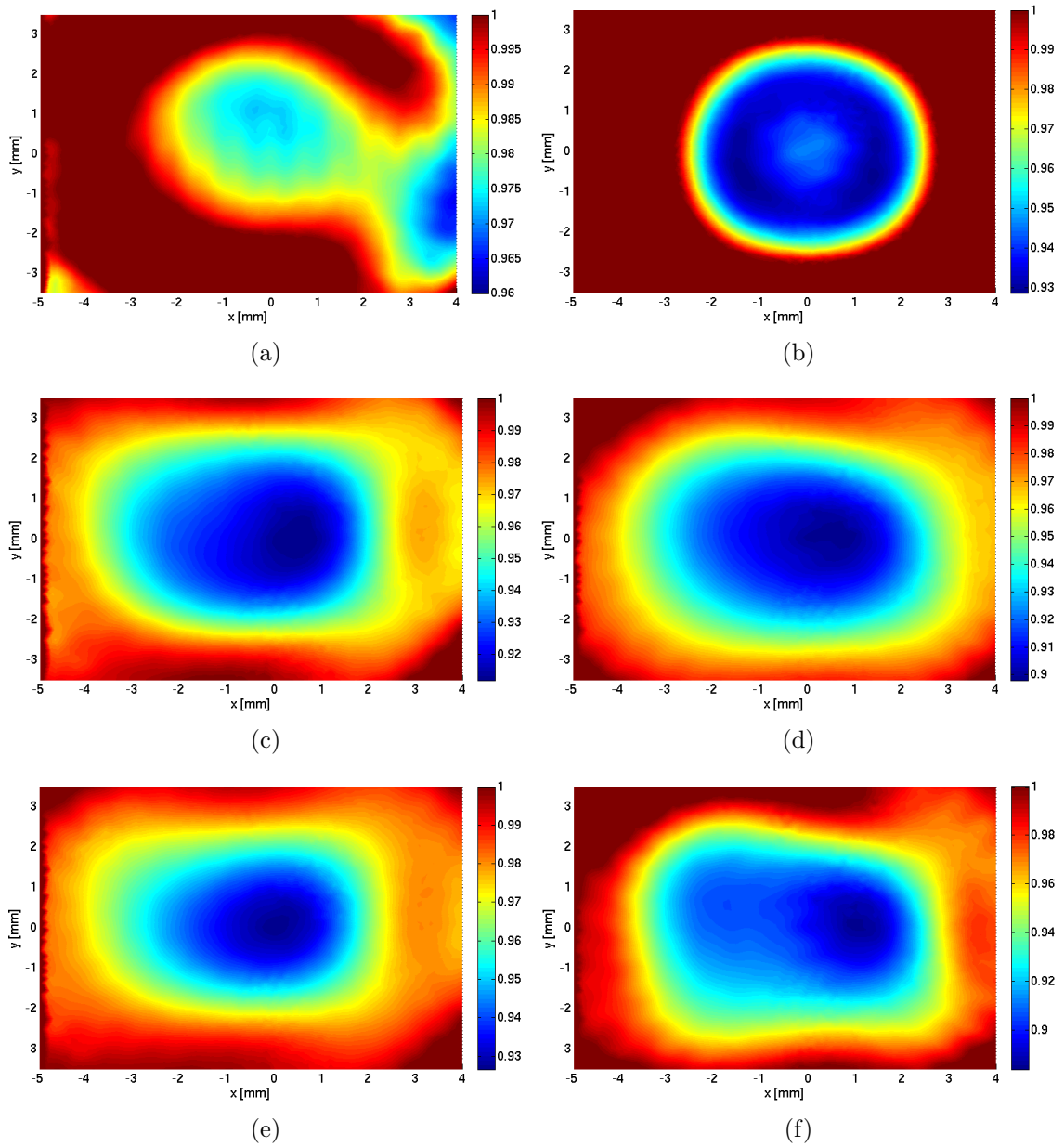


Figure A.2: Reconstructions of human-tissue phantom data at 1.1 MHz. The inversions are performed with information from 3 receivers for each of the 32 transmitters. The expected image is a 4 mm square with $\chi' = 0.93$. (a) Image from measurement data before calibration. (b) Image reconstructed from synthetic FEM data. (c) Image from measurement data after incident field calibration using the 2D point-source incident field model. (d) Image from measurement data after scattered field calibration using the 2D point-source calibration object model. (e) Image from measurement data after incident field calibration using the 3D point-source incident field model. (f) Image from measurement data after scattered field calibration using the 3D point-source calibration object model.

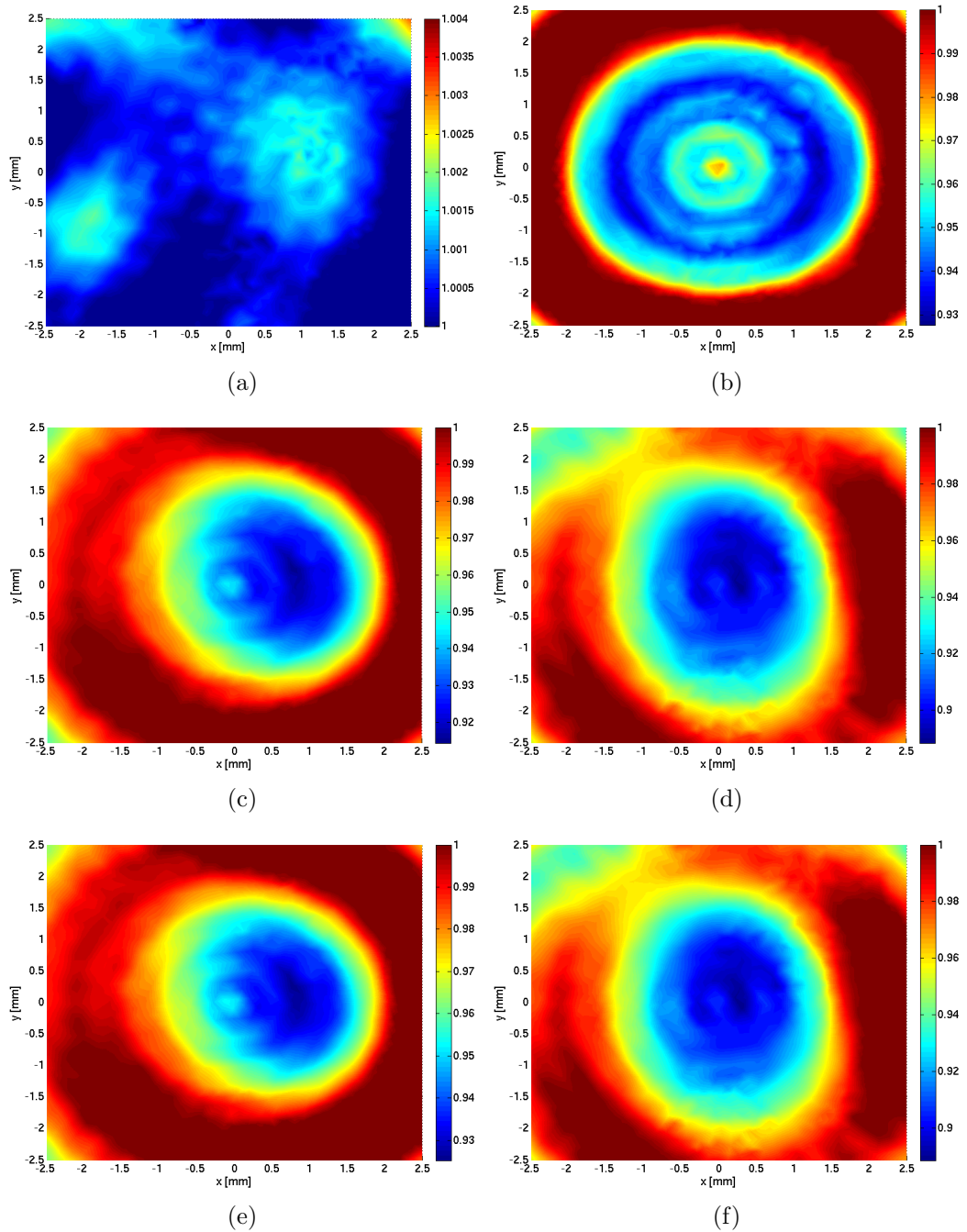


Figure A.3: Reconstructions of human-tissue phantom data at 1.5 MHz. The inversions are performed with information from 3 receivers for each of the 32 transmitters. The expected image is a 4 mm square with $\chi' = 0.93$. (a) Image from measurement data before calibration. (b) Image reconstructed from synthetic FEM data. (c) Image from measurement data after incident field calibration using the 2D point-source incident field model. (d) Image from measurement data after scattered field calibration using the 2D point-source calibration object model. (e) Image from measurement data after incident field calibration using the 3D point-source incident field model. (f) Image from measurement data after scattered field calibration using the 3D point-source calibration object model.

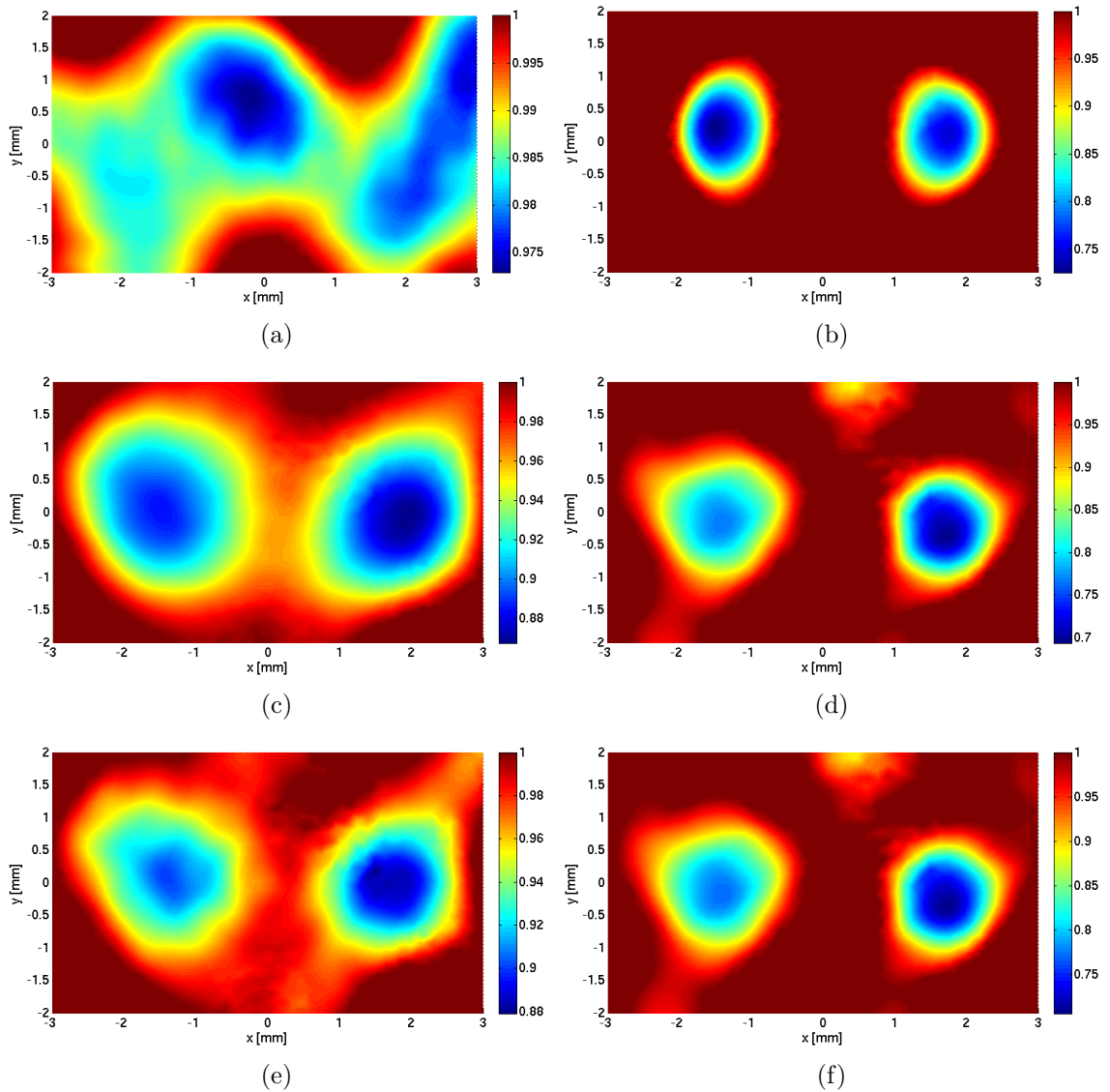


Figure A.4: Inversion results of data for two aluminium wires at 1.2 MHz. The inversions are performed with information from 5 receivers for each of the 32 transmitters. The expected image is that of the cross-section of two wires placed side-by-side, approximately 1.5 mm apart; both wires have a diameter of 1.4 mm. Note that the reconstructed contrast values have little meaning because the density of aluminium is very different from that of the background medium (water). (a) Image from measurement data before calibration. (b) Image reconstructed from FDTD data. (c) Image from measurement data after incident field calibration using the 2D point-source incident field model. (d) Image from measurement data after scattered field calibration using the 2D point-source calibration object model. (e) Image from measurement data after incident field calibration using the 3D point-source incident field model. (f) Image from measurement data after scattered field calibration using the 3D point-source calibration object model.

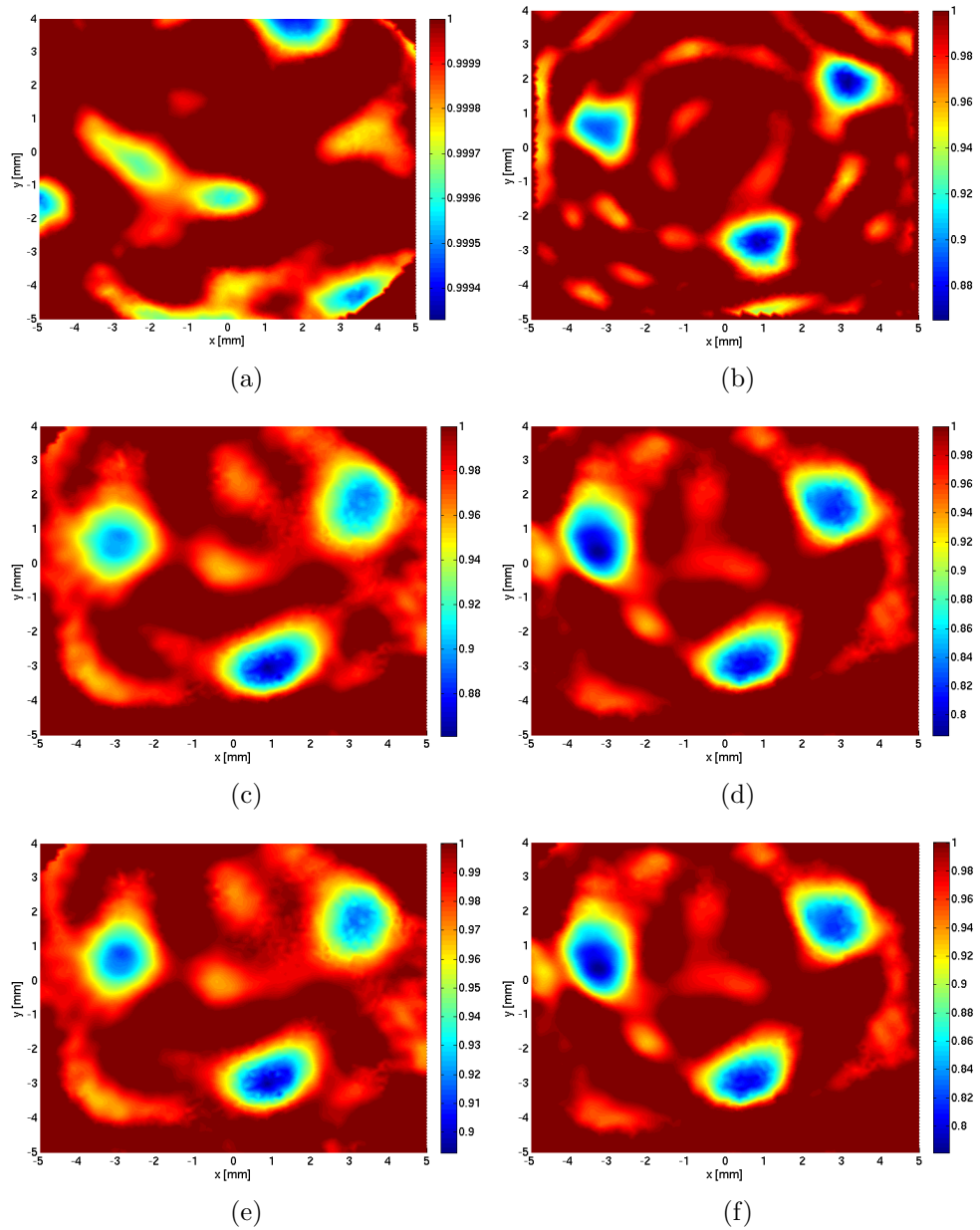


Figure A.5: Inversion results of data for three aluminium wires at 1.4 MHz. The inversions are performed with information from 5 receivers for each of the 32 transmitters. The expected image is that of the cross-section of three wires placed in a triangular formation where wire pairs are approximately 4 mm apart; all wires have a diameter of 1.4 mm. Note that the reconstructed contrast values have little meaning because the density of aluminium is very different from that of the background medium (water). (a) Image from measurement data before calibration. (b) Image reconstructed from FDTD data. (c) Image from measurement data after incident field calibration using the 2D point-source incident field model. (d) Image from measurement data after scattered field calibration using the 2D point-source calibration object model. (e) Image from measurement data after incident field calibration using the 3D point-source incident field model. (f) Image from measurement data after scattered field calibration using the 3D point-source calibration object model.

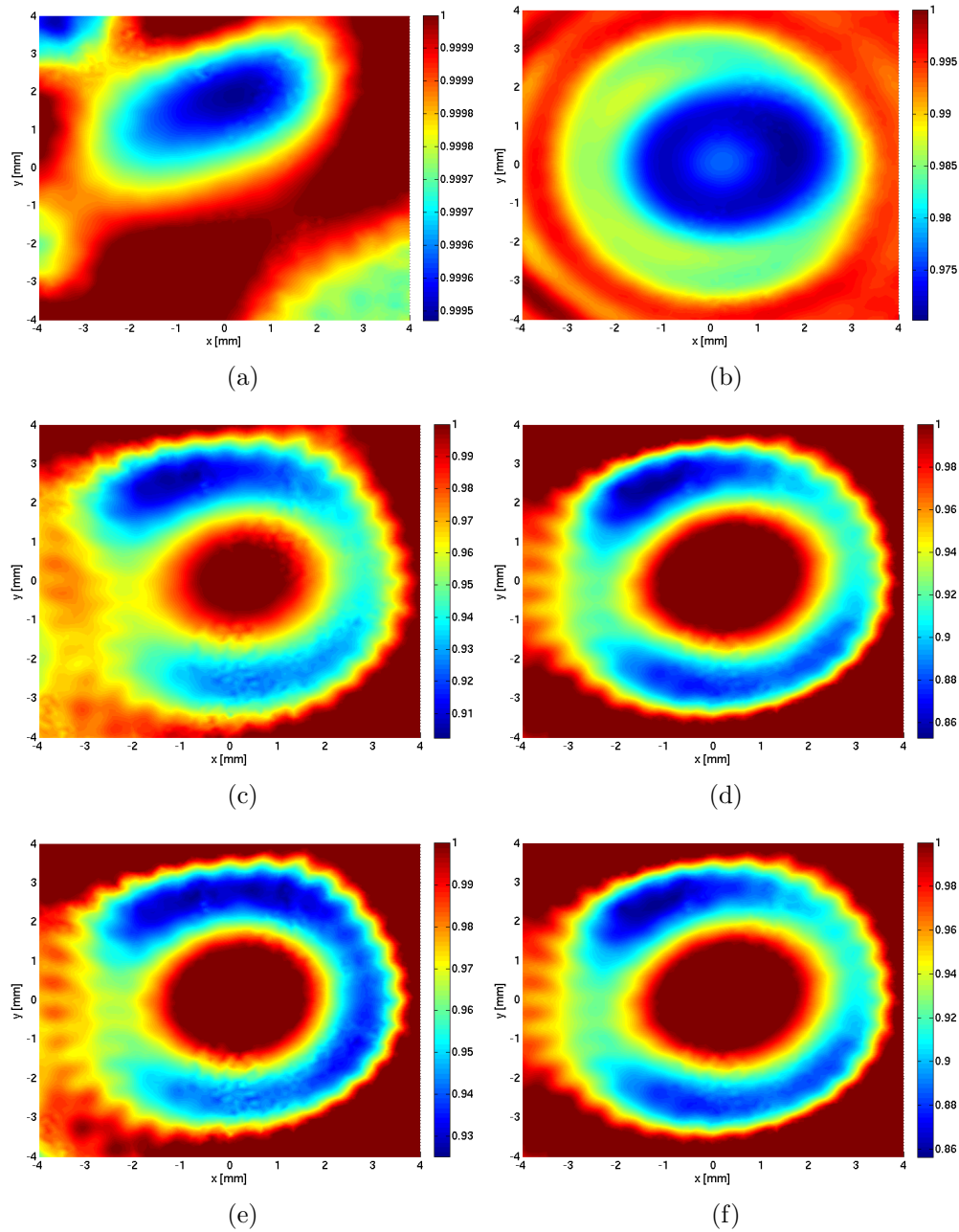


Figure A.6: Inversion results of data for a high-density polyethylene rod at 1.2 MHz. The inversions are performed with information from 3 receivers for each of the 32 transmitters. The expected image is a 7.5 mm diameter solid circle with $\chi' = 0.64$. Note that the density discrepancy of the polyethylene rod is nearly 6% and its largest dimension is approximately 6 wavelengths. These properties are near the limits supported by FEM-CSI. (a) Image from measurement data before calibration. (b) Image reconstructed from FDTD data. (c) Image from measurement data after incident field calibration using the 2D point-source incident field model. (d) Image from measurement data after scattered field calibration using the 2D point-source calibration object model. (e) Image from measurement data after incident field calibration using the 3D point-source incident field model. (f) Image from measurement data after scattered field calibration using the 3D point-source calibration object model.

B

Frequency-Domain Representation of Signal Data

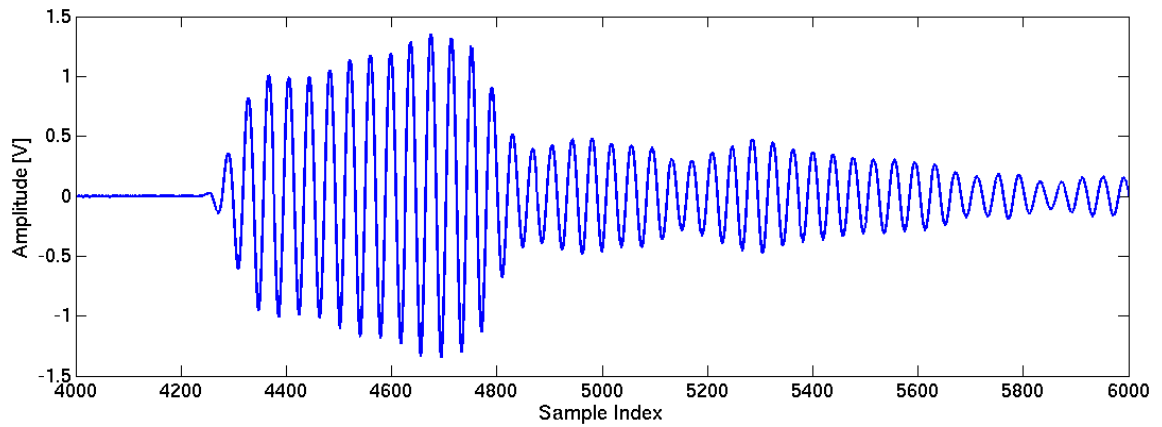
This appendix covers some of the details regarding the representation of measured signal data in the frequency-domain. Also included are example plots of measured time-domain data and their frequency-domain counterparts.

Data measured by the UST system are transformed to the frequency-domain with the fast Fourier transform (FFT) function provided in the MATLAB [24] development environment (`fft()`). The frequency resolution obtained with this function is the ratio of the sampling frequency and the number of samples in the signal. Measurement parameters commonly utilized in this work provide a frequency resolution of approximately 7 kHz due to a sampling rate of 50 MHz and a signal length of 7000 samples.

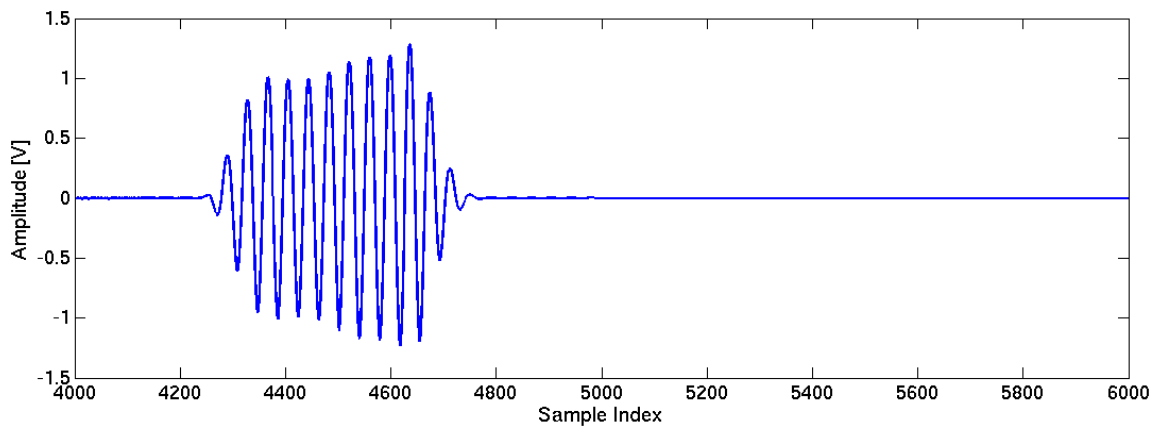
In the event that the user-defined frequency of interest falls between two frequency components computed by FFT, it is the frequency component nearest the frequency of interest which is used and no interpolation is performed. This same frequency component is used for each signal in a calibration process in order to maintain consistency. The availability of this frequency component is guaranteed for all signals measured in an experiment by using the same sampling rate and number of samples throughout. The actual frequency used in the inversion algorithm is the same as the one used for calibration.

The values returned by the FFT function can be represented in phasor form. When represented in such a way, the measured data are compatible with the phasor-based calibration principles introduced in Chapter 6. This representation also allows each signal component to be expressed as a quantity describing its amplitude and phase, which can be useful for data plotting and analysis.

Plots of time-domain data and their frequency-domain representations are given in this appendix. Transformations of windowed and unmodified time-domain data are shown in order to demonstrate the effects of windowing on their frequency-domain form. All plotted signals were recorded for a transmitted 1.3 MHz sinusoidal waveform with a pattern length of 10 microseconds. The sampling frequency was set to 50 MHz.

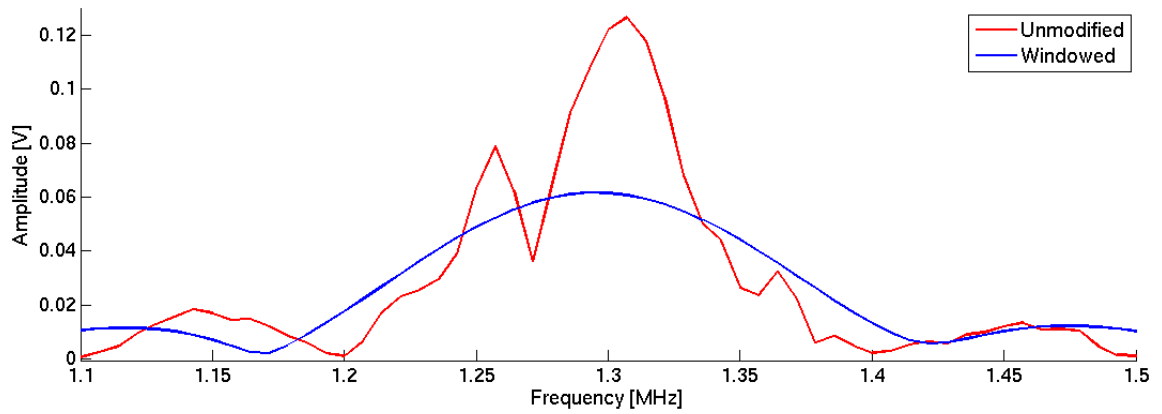


(a)

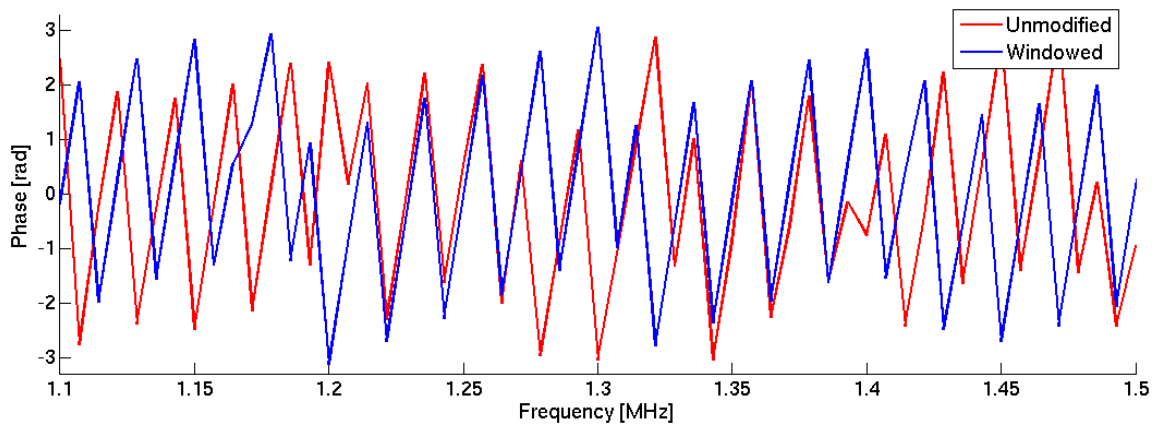


(b)

Figure B.1: Measured time-domain incident field signal before applying the FFT. Its frequency-domain representation is given in Figure B.2. (a) Incident field before windowing is applied. (b) Incident field after windowing.



(a)



(b)

Figure B.2: Frequency-domain representation of a measured incident field signal. The time-domain signal is given in Figure B.1. (a) Signal amplitude as a function of frequency. (b) Signal phase as a function of frequency, restricted to $\pm\pi$.

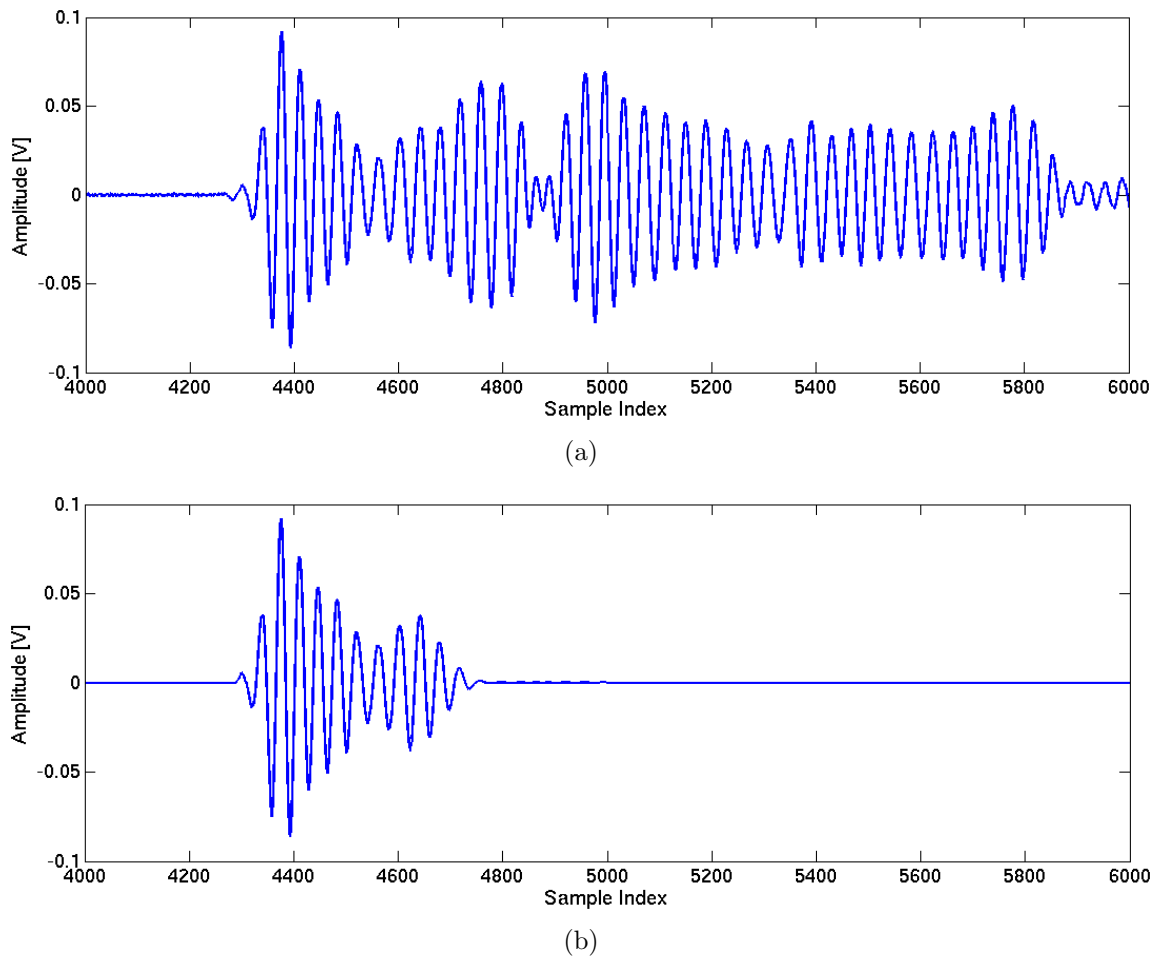


Figure B.3: Measured time-domain scattered field signal before applying the FFT. The scatterer used to produce this signal is the human tissue phantom described in section 7.2.1. The frequency-domain representation for this signal is given in Figure B.4. (a) Scattered field before windowing is applied. (b) Scattered field after windowing.

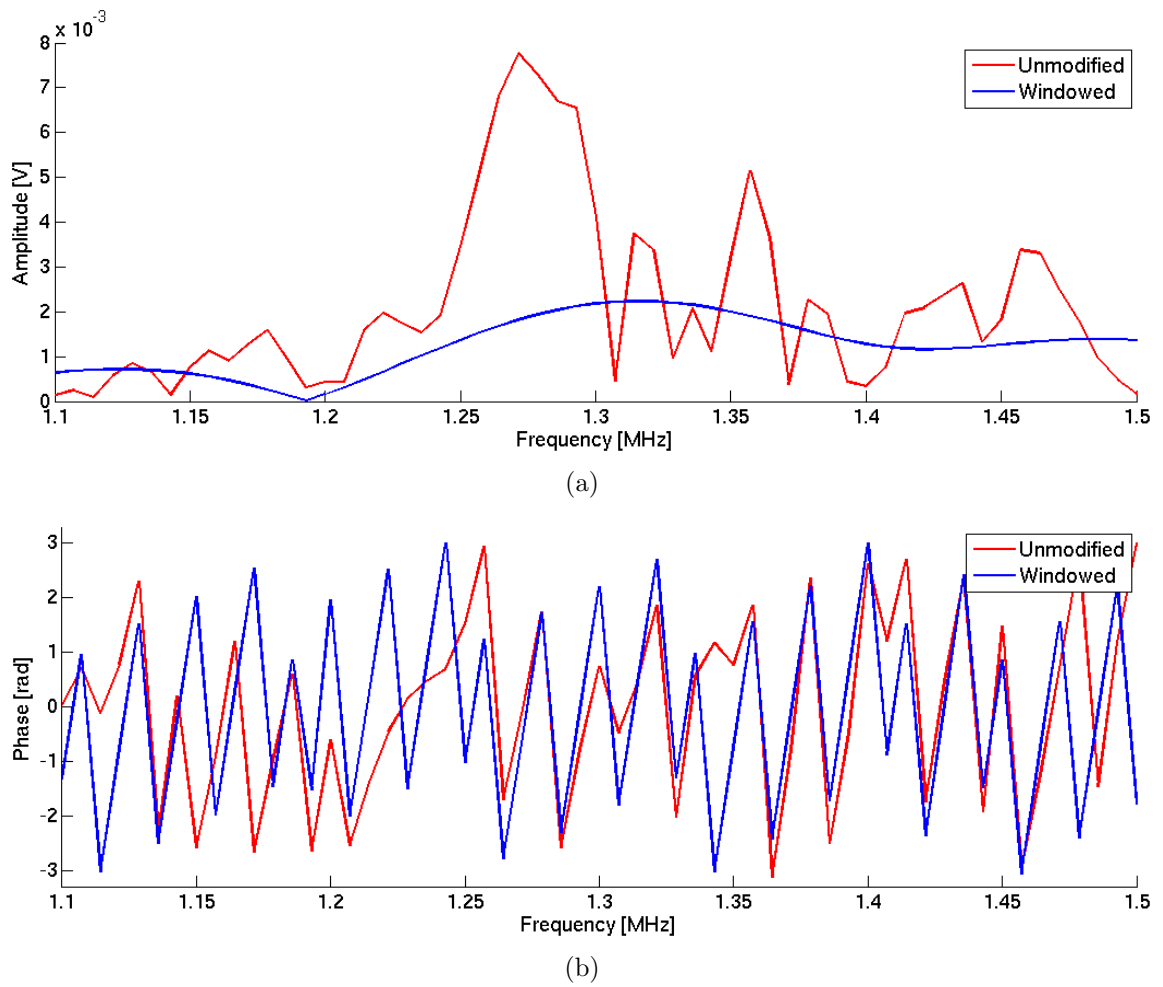


Figure B.4: Frequency-domain representation of a measured scattered field signal. The time-domain signal is given in Figure B.3. (a) Signal amplitude as a function of frequency. (b) Signal phase as a function of frequency, restricted to $\pm\pi$.

References

- [1] A. Dhawan, *Medical Image Analysis*. New Jersey: Wiley Inter-Science, 2003.
- [2] R. Sanders and T. Winter, *Clinical Sonography: A Practical Guide*, 4th ed. Lippincott Williams & Wilkins, 2006.
- [3] J. Ferlay, H. Shin, F. Bray, D. Forman, C. Mathers, and D. Parkin. (2008) Globocan 2008 v1.2, cancer incidence and mortality worldwide: Iarc cancerbase no. 10. International Agency for Research on Cancer. Lyon, France. Accessed on 01/05/12. [Online]. Available: <http://globocan.iarc.fr>
- [4] R. Swart. (2011, August) Breast cancer screening. Medscape. Accessed on 01/05/12. [Online]. Available: <http://emedicine.medscape.com/article/1945498-overview#aw2aab6b5>
- [5] C. Gilmore, P. Mojabi, A. Zakaria, M. Ostadrahimi, C. Kaye, S. Noghianian, L. Shafai, S. Pistorius, and J. LoVetri, "A wideband microwave tomography system with a novel frequency selection procedure," *Biomedical Engineering, IEEE Transactions on*, vol. 57, no. 4, pp. 894–904, 2010.
- [6] C. Gilmore, A. Zakaria, P. Mojabi, M. Ostadrahimi, S. Pistorius, and J. LoVetri, "The university of manitoba microwave imaging repository: A two-dimensional microwave scattering database for testing inversion and calibration algorithms," *IEEE Antennas and Propagation*, vol. 53, no. 5, October 2011.
- [7] M. Ostadrahimi, P. Mojabi, S. Noghianian, J. LoVetri, and L. Shafai, "A multiprobe-per-collector modulated scatterer technique for microwave tomography," *Antennas and Wireless Propagation Letters, IEEE*, vol. 10, pp. 1445–1448, 2011.
- [8] M. Ostadrahimi, P. Mojabi, S. Noghianian, L. Shafai, S. Pistorius, and J. LoVetri, "A novel microwave tomography system based on the scattering probe technique," *Instrumentation and Measurement, IEEE Transactions on*, no. 99, pp. 1–12, 2011.
- [9] A. Zakaria, "The finite-element contrast source inversion method for microwave imaging applications," Ph.D. dissertation, University of Manitoba, 2012.

-
- [10] P. Mojabi, “Investigation and development of algorithms and techniques for microwave tomography,” Ph.D. dissertation, University of Manitoba, May 2010.
- [11] C. Kumaragamage and P. Oramasionwu, “Design of an ultrasound tomography system for breast cancer imaging,” University of Manitoba, Tech. Rep., 2010.
- [12] T. Szabo, *Diagnostic Ultrasound Imaging*. Elsevier Academic Press, 2004.
- [13] N. Duric, “Development of ultrasound tomography for breast imaging: Technical assessment,” *Medical Physics*, vol. 32, no. 5, 2005.
- [14] N. Duric and P. Littrup, “Detection of breast cancer with ultrasound tomography: First results with the computed ultrasound risk evaluation (cure) prototype,” *Medical Physics*, vol. 34, no. 2, 2007.
- [15] R. Waag and R. Fedewa, “A ring transducer system for medical ultrasound research,” *IEEE Transactions on Ultrasonics, Ferroelectrics and Frequency Control*, vol. 53, no. 10, October 2006.
- [16] M. Andre, H. Janeé, P. Martin, G. Otto, B. Spivey, and D. Palmer, “High-speed data acquisition in a diffraction tomography system employing large-scale toroidal arrays,” *International Journal of Imaging Systems and Technology*, vol. 8, no. 1, pp. 137–147, 1997.
- [17] L. Mercier, T. Langø, F. Lindseth, and L. Collins, “A review of calibration techniques for freehand 3-d ultrasound systems,” *Ultrasound in medicine & biology*, vol. 31, no. 2, pp. 143–165, 2005.
- [18] M. Ostadrahimi, P. Mojabi, C. Gilmore, A. Zakaria, S. Noghianian, S. Pistorius, and J. LoVetri, “Analysis of incident field modeling and incident/scattered field calibration techniques in microwave tomography,” *Antennas and Wireless Propagation Letters, IEEE*, no. 99, 2011.
- [19] J. Kruskal, “Multidimensional scaling by optimizing goodness of fit to a non-metric hypothesis,” *Psychometrika*, vol. 29, no. 1, pp. 1–27, 1964.
- [20] O. Roy, I. Jovanovic, N. Duric, L. Poulo, and M. Vetterli, “Robust array calibration using time delays with application to ultrasound tomography,” in *SPIE Medical Imaging*, vol. 7968, 2011.
- [21] P. Drineas, A. Javed, M. Magdon-Ismail, G. Pandurangant, R. Virrankoski, and A. Savvides, “Distance matrix reconstruction from incomplete distance information for sensor network localization,” in *Sensor and Ad Hoc Communications and Networks, 2006. SECON’06. 2006 3rd Annual IEEE Communications Society on*, vol. 2. IEEE, 2006, pp. 536–544.

-
- [22] A. Karbasi, S. Oh, R. Parhizkar, and M. Vetterli, “Ultrasound tomography calibration using structured matrix completion,” in *International Congress on Acoustics (ICA2010)*, 2010.
- [23] K. Foo and P. Atkins, “A relative-localization algorithm using incomplete pairwise distance measurements for underwater applications,” *EURASIP Journal on Advances in Signal Processing*, vol. 2010, pp. 10–10, 2010.
- [24] The MathWorks, Inc. (2007, January) Matlab.
- [25] A. Arnau Vives, *Piezoelectric Transducers and Applications*, 2nd ed. Verlag Berlin Heidelberg: Springer, 2008.
- [26] D. Staelin, A. Morgenthaler, and J. Kong, *Electromagnetic Waves*. New Jersey: Prentice Hall, 1994.
- [27] D. S. Jones, *Acoustic and Electromagnetic Waves*. New York: Oxford University Press, 1989.
- [28] I. Karatzas and S. Shreve, *Brownian motion and stochastic calculus*. Springer Verlag, 1991, vol. 113.
- [29] R. Harrington, *Time-Harmonic Electromagnetic Fields*, ser. IEEE Press Series on Electromagnetic Wave Theory. IEEE Press, 2001.
- [30] J. C. Maxwell, “A dynamical theory of the electromagnetic field,” *Philosophical Transactions of the Royal Society of London*, vol. 155, pp. 459–512, 1865. [Online]. Available: <http://rstl.royalsocietypublishing.org/content/155/459.short>
- [31] P. M. Morse and K. U. Ingard, *Theoretical Acoustics*. New Jersey: Princeton University Press, 1986.
- [32] D. D. Joseph, *Fluid Dynamics of Viscoelastic Liquids*. New York: Springer-Verlag, 1990.
- [33] H. Tabuteau, D. Sikorski, and J. R. de Bruyn, “Shear waves and shocks in soft solids,” *Physical Review E*, vol. 75, no. 1, p. 012201, 2007.
- [34] F. Zhen and W. Shuozhong, “Improved algorithm for the implementation of unified ftdt in underwater sound scattering,” *Journal of Shanghai University*, vol. 3, no. 2, June 1999.
- [35] O. Reynolds, *Papers on Mechanical and Physical Subjects*, ser. The Sub-Mechanics of the Universe. Cambridge: Cambridge University Press, 1903, vol. 3.

-
- [36] K. Muralidhar and G. Biswas, *Advanced Engineering Fluid Mechanics*. Alpha Science International, 2005.
- [37] I. Newton, *The mathematical principles of natural philosophy*, ser. The Mathematical Principles of Natural Philosophy. printed for Benjamin Motte, 1729, no. v. 2. [Online]. Available: <http://books.google.ca/books?id=6EqxPav3vIsC>
- [38] T. Rossing, *Springer Handbook of Acoustics*. New York: Springer Science, 2007.
- [39] P. Bergmann, “The wave equation in a medium with a variable index of refraction,” *The Journal of the Acoustical Society of America*, vol. 17, no. 4, pp. 329–333, 1946.
- [40] R. Cobbold, *Foundations of biomedical ultrasound*. Oxford University Press, USA, 2006.
- [41] J. Stratton, *Electromagnetic Theory*, D. Dudley, Ed. Wiley-Interscience, 2007.
- [42] A. Taflove and S. Hagness, *Computational Electrodynamics: The Finite-Difference Time-Domain Method*, ser. Artech House Antennas and Propagation Library. Artech House, 2005.
- [43] K. Kunz and R. Luebbers, *The Finite Difference Time Domain Method for Electromagnetics*. CRC Press, 1993.
- [44] J. LoVetri, D. Mardare, and G. Soulodre, “Modeling of the seat dip effect using the finite-difference time-domain method,” *The Journal of the Acoustical Society of America*, vol. 100, p. 2204, 1996.
- [45] K. Yee, “Numerical solution of initial boundary value problems involving maxwell’s equations in isotropic media,” *Antennas and Propagation, IEEE Transactions on*, vol. 14, no. 3, pp. 302–307, 1966.
- [46] P. Morse and H. Feshbach, *Methods of Theoretical Physics*, G. Harnwell, Ed. McGraw-Hill, 1953, vol. 1.
- [47] G. Mur, “Absorbing boundary conditions for the finite-difference approximation of the time-domain electromagnetic-field equations,” *IEEE Transactions on Electromagnetic Compatibility*, vol. EMC-23, no. 4, pp. 377–382, November 1981.
- [48] A. Zakaria, C. Gilmore, and J. LoVetri, “Finite-element contrast source inversion method for microwave imaging,” *Inverse Problems*, vol. 26, no. 11, November 2010.

-
- [49] P. Van Den Berg and R. Kleinman, "A contrast source inversion method," *Inverse Problems*, vol. 13, no. 6, 1997.
- [50] J. LoVetri and A. Zakaria, Personal communication.
- [51] S. Beer, "An ultrasound tomography system for biomedical imaging," Master's thesis, Hochschule Ravensburg-Weingarten, April 2011.
- [52] E. Brigham and R. Morrow, "The fast fourier transform," *Spectrum, IEEE*, vol. 4, no. 12, pp. 63–70, 1967.
- [53] A. Oppenheim, A. Willsky, and S. Nawab, *Signals & Systems*. New Jersey: Prentice Hall, 1983.
- [54] J. Irwin and R. Nelms, *Basic Engineering Circuit Analysis*, 8th, Ed. New Jersey: Wiley, 2005.
- [55] C. Eckart and G. Young, "The approximation of one matrix by another of lower rank," *Psychometrika*, vol. 1, no. 3, pp. 211–218, 1936.
- [56] K. Cheung and H. So, "A multidimensional scaling framework for mobile location using time-of-arrival measurements," *Signal Processing, IEEE Transactions on*, vol. 53, no. 2, pp. 460–470, 2005.
- [57] J. Lubbers and R. Graaff, "A simple and accurate formula for the sound velocity in water," *Ultrasound in medicine & biology*, vol. 24, no. 7, pp. 1065–1068, 1998.
- [58] J. Hunt, M. Arditi, and F. Foster, "Ultrasound transducers for pulse-echo medical imaging," *Biomedical Engineering, IEEE Transactions on*, no. 8, pp. 453–481, 1983.
- [59] F. Harris, "On the use of windows for harmonic analysis with the discrete fourier transform," *Proceedings of the IEEE*, vol. 66, no. 1, pp. 51–83, 1978.
- [60] R. Bude and R. Adler, "An easily made, low-cost, tissue-like ultrasound phantom material," *Journal of clinical ultrasound*, vol. 23, no. 4, pp. 271–273, 1995.
- [61] T. Mast, "Empirical relationships between acoustic parameters in human soft tissues," *Acoustics Research Letters Online*, vol. 1, p. 37, 2000.
- [62] M. Haynes and M. Moghaddam, "Large-domain, low-contrast acoustic inverse scattering for ultrasound breast imaging," *Biomedical Engineering, IEEE Transactions on*, vol. 57, no. 11, pp. 2712–2722, 2010.
- [63] M. Moghaddam and W. C. Chew, "Simultaneous inversion of compressibility and density in the acoustic inverse problem," *Inverse problems*, vol. 9, no. 6, p. 715, 1999.

-
- [64] C. Wang, P. Hale, and K. Coakley, “Least-squares estimation of time-base distortion of sampling oscilloscopes,” *Instrumentation and Measurement, IEEE Transactions on*, vol. 48, no. 6, pp. 1324–1332, 1999.
- [65] K. Coakley and P. Hale, “Alignment of noisy signals,” *Instrumentation and Measurement, IEEE Transactions on*, vol. 50, no. 1, pp. 141–149, 2001.
- [66] D. Yeh, O. Oralkan, I. Wygant, M. O’Donnell, and B. Khuri-Yakub, “3-d ultrasound imaging using a forward-looking cmut ring array for intravascular/intracardiac applications,” *Ultrasonics, Ferroelectrics and Frequency Control, IEEE Transactions on*, vol. 53, no. 6, pp. 1202–1211, 2006.
- [67] D. Mills, “Medical imaging with capacitive micromachined ultrasound transducer (cmut) arrays,” in *Ultrasonics Symposium, 2004 IEEE*, vol. 1. IEEE, 2004, pp. 384–390.